A BODY AREA NETWORK FOR WEARABLE HEALTH MONITORING: CONDUCTIVE FABRIC GARMENT UTILIZING DC-POWER-LINE CARRIER COMMUNICATION

by

Eric R. Wade

S. B. Mechanical Engineering
Massachusetts Institute of Technology, 2000

S. M. Mechanical Engineering
Massachusetts Institute of Technology, 2004

S. M. Electrical Engineering
Massachusetts Institute of Technology, 2004

Submitted to the Department of Mechanical Engineering
in Partial Fulfillment of the Requirements for the Degree of
Doctor of Philosophy in Mechanical Engineering

at the
Massachusetts Institute of Technology

February 2007

Signature of Author .....
Department of Mechanical Engineering
January 12, 2007

Certified by .....
H. Harry Asada
Ford Professor of Mechanical Engineering
Thesis Supervisor

Accepted by .....
Lallit Anand
Chairman, Department Committee on Graduate Students

A Body Area Network for Wearable Health Monitoring: Conductive Fabric Garment utilizing DC-Power-line Carrier Communication

by

Eric R. Wade

Submitted to the Department of Mechanical Engineering
On January 12, 2007 in Partial Fulfillment of the
Requirements of the Degree of Doctor of Philosophy in
Mechanical Engineering

ABSTRACT

Wearable computing applications are becoming increasingly present in our lives. Of the many wearable computing applications, wearable health monitoring may have the most potential to make a lasting positive impact. The ability to remotely monitor physiological signals such as respiration, motion, and temperature has benefits for populations such as elderly citizens, fitness professionals, and soldiers in the battlefield. To fully integrate wearable networks into a user's daily life, these systems must be minimally invasive and minimally intrusive. At the same time, such wearable networks require multiple sensors and electronic components to be mounted on the body. Unfortunately, typical off-the-shelf components of this nature are heavy, bulky, and don't integrate well with the human form. Thus, it is critical to figure out how best to minimize the physical and mental burden that these systems place on the user.

To address these problems, we propose a new method of designing wearable health monitoring networks by combining electrically conductive fabrics and power-line communication technology. Electrically conductive fabrics are useful in that they feel and behave like normally worn clothing but also have the ability to transmit data and power. To fully exploit the conductive fabric as a transmission medium, we also use power-line communication technology. Power-line communication allows for simultaneous power and data transmission over a shared medium. The use of these two technologies will allow us to significantly reduce the amount of metal cabling on the body and to reduce overall system bulk and weight.

With this project, we design the DC-PLC system that will act as the physical layer of the architecture. Next, we construct a prototype body area network, and derive analytical models for predicting garment electrostatic and electro-dynamic properties using Maxwell's equations, and verify using empirical data and finite-element analysis. Finally, we will determine relevant rules and guidelines for the design and construction of such garments.

Thesis Supervisor: H. Harry Asada
Title: Ford Professor of Mechanical Engineering

I would like to thank God for using me as his instrument. This work is a manifestation of His will and power. I dedicate this work to all of those who have played a part in getting me to this point in my life, most especially; my parents, Jerome and Leslie; my brothers, Jerome, Neil and Craig; and Mikii, without whom none of this would have been possible.

TABLE OF CONTENTS

TABLE OF FIGURES

1. Introduction

1.1. Wearable Health Monitoring

In recent years, we have seen many advances in the field of wearable computing. Wearable computing is fast becoming a ubiquitous concept. Of the many wearable computing applications, wearable health monitoring will have an immense and immediate benefit to our quality of life by allowing for constant monitoring of physiological signals such as limb motion, respiration, and skin temperature. Such systems can expedite recovery and rehabilitation, immediately address a sudden decline in health, and assist those in need until they have access to a health professional. In order for this wearable network to be widely accepted, it must also be minimally invasive and minimally intrusive. Specifically, the users of such a system should be able to carry out their normal activities without actual or perceived impediment from the wearable network. The ideal users of such systems are fitness professionals [1],[2], soldiers in the battlefield [3],[4], and particularly the elderly population [5],[6]. The elderly population, often at increased risk for health problems, has been steadily increasing. Finding the facilities and resources for dealing with these problems is critical. Oftentimes, elderly people are forced to stay in a hospital or nursing home while physiological signals are monitored. With this work, such patients will be able to return to their homes for improved quality of life.

Fig. 1 Conductive fabric garment

Many health monitoring applications require the placement of electrical components on the user. Placing these components on the body requires careful consideration for the physical connections of the components, the bulk and weight of the components, and the routing of wires along the body [7],[8]. For instance, locations of minimum movement and maximum load carrying capacity are optimal for locating heavy components, and should be considered for the design of these systems [9]. In fact, numerous metrics for wearability have been discussed, but are not often implemented.

The authors have devised a unique approach to addressing these issues by applying direct-current power-line carrier communication (DC-PLC) technology to a wearable monitoring system. DC-PLC is a technology in which a single shared DC bus is used to provide power to each node and facilitate communication between multiple nodes in an electrical network [10]. In our system, sensor nodes are embedded in the garment at various locations. The sensor nodes transmit data to a master node which transmits all sensor information wirelessly to a local capture and storage medium, such as a personal computer.

To truly make the system wearable and to allow for connectivity of sensors at any point on the body, we must ensure that the DC bus is flexible and lightweight, which precludes the use of traditional metal wiring. Instead, we propose to use conductive fabric sheets sewn into clothing garments as the electrical transmission medium, as demonstrated in [11] and [12]. These fabrics do not restrict the wearer's body movement and behave like normal fabrics. Initial work on the use of conductive fabric sheets for electrical transmission has been conducted by the authors as well as others [12],[13],[14].

1.2. Communication over DC Power-lines

Simultaneous transmission of power and information over a single medium is commonly known as power-line carrier communication, or simply power-line communication (PLC). This technology has been used primarily for in-home networks to transmit data over pre-laid power lines. However, we propose to use PLC over a conductive fabric garment for a localized, body-area network. Thus, our network architecture is different from these pre-existing systems.

The direct current (DC) PLC system, pictured in Fig. 2, was first introduced and applied to a wearable system in [11]. In [10], the authors described an implementation for

such a system that relies on transmission-line transformer (TLT) theory and knowledge of the medium's resistive properties to minimize insertion losses associated with PLC transformers. The DC-PLC system consists of three components; the transmission medium, a master command node, and the sensor nodes. The system we have developed requires only two conductors; a supply line, that we call the consolidated power-signal (CPS) line, and a ground line for electrical return. The CPS is used to transmit both DC power and data between the master node and the sensor nodes within the system. The master node acts as the command node by sending commands to and reading data from the sensors located throughout the network. It also contains a single battery which serves as the power source for the system. As a result, the sensors do not need local batteries; this reduces the overall bulk and weight of the network. As the number of sensor nodes increases, these savings become more significant.

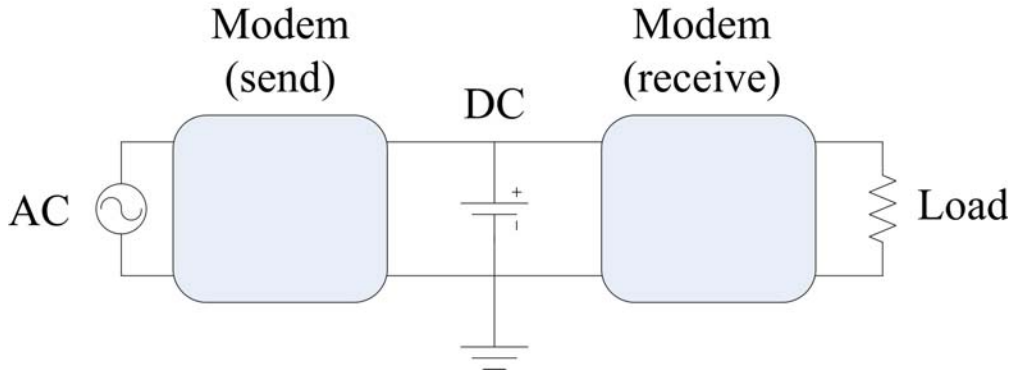

Fig. 2 DC-PLC System Diagram

We must allow for connectivity of multiple types of sensors to gather a variety of physiological signals. Therefore, we need a means of converting the DC battery voltage of the master node to each sensor's required power level. Similarly, we need to convert the sensor outputs to a digital signal. A modem is needed to perform these functions. The sensor nodes utilize a modem developed by the authors specifically for a high-fanout DC-PLC system [10]. The modem, which contains a DC-to-DC converter, an analog-to-digital converter, a TLT, and a phased-lock loop, can be interfaced with a multitude of sensor types. It can read both analog and digital data, then digitize (if necessary), encode, and modulate the signal for transmission over the CPS to the master node. Frequency-shift keying (FSK) is used to modulate the signals, and frequency separation is used to minimize the number of collisions between sensor node transmissions. Each sensor is

assigned a specific carrier frequency; when the master node wants to view data from a given sensor, it demodulates the aggregate signal seen on the power line using the appropriate carrier.

Our prototype is pictured in Fig. 1. We construct the garment with a 'sandwich' of conductors and insulators, as shown in Fig. 3. There are two layers of conductive fabric, one each used for transmission and grounding. In addition, there are three layers of insulation to prevent electrical contact between the ground and supply lines, between ground and the environment, and between supply and the user.

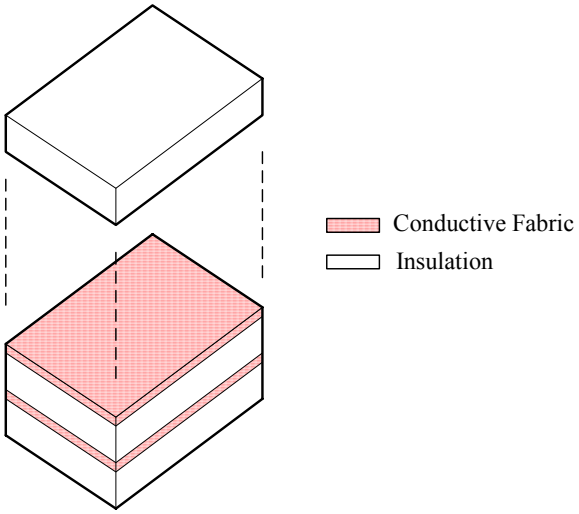

Fig. 3 Sandwich Section Construction of Conductive Fabric Garment

1.3. Conductive Fabric Signal Transmission

The CPS and ground line are constructed using electrically conductive fabric sheets sewn into a fabric garment. A transmission medium covering the whole body will allow us to connect sensor nodes anywhere. It also spatially distributes the medium, which reduces the user's burden. Thus, conductive fabrics are well-suited for wearable systems. However, one major drawback of conductive fabrics is their significantly large resistivity, on the order of 100Ω/cm for a single strand. To overcome this poor resistivity problem, the conductive fabrics are used as a two-dimensional media as opposed to a one-dimensional medium such as traditional metal cables. We argue the validity of this approach with an intuitive example. As shown in Fig. 4, two points, P_+ and P_-, are located on a line separated by a distance h. If the points are connected by a single strand of a constant cross-section, homogenous conductive material, the electrical resistance

between the points varies linearly with *h* (Fig. 4a). However, in a flat, constant cross-section homogeneous sheet of conductive material, we find that the two points separated by h have a multitude of transmission paths between them (Fig. 4b). As a result, the electrical resistance between the points in the sheet is much lower than that of the points along a wire. The low transmission resistance allows us to transmit power as well as signals.

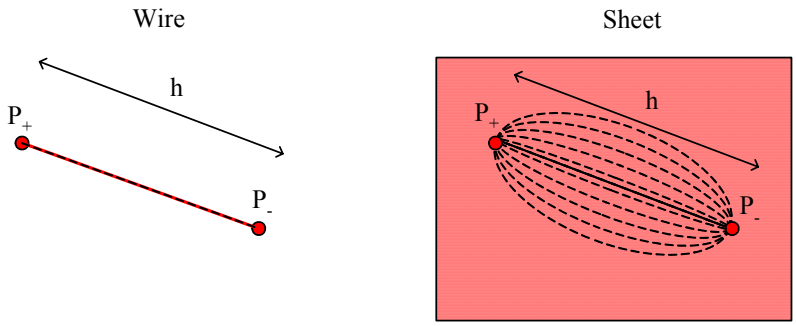

Fig. 4 Single strand compared to a sheet

1.4. System Integration

In this thesis, we will present a novel method for the analysis and design of these conductive fabric garment sensor networks. We introduce three functional requirements for our wearable DC-PLC system, motivated by the needs and lifestyles of the targeted populations. In constructing this wearable network, we require; (1) the ability to place sensor nodes anywhere on the body, (2) the ability to maintain sufficiently low line resistance to facilitate electrical transmission between the multiple nodes, and (3) minimization of the burden on the wearer.

First, we will discuss the DC-PLC technique. This involves the design of the electronic components, including (but not limited to) designing the wireless communication device, designing the modems at each sensor node, and tuning the modem impedances to ensure that loads are matched.

Next, we will discuss the relevant properties and behavior of conductive fabrics. Because of their non-ideal properties, we must introduce a method of accurately estimating relevant electrical properties such as impedance and resistance, and determine how these properties affect the overall system design and performance. To do so, we will

need to introduce a method for predicting the DC resistance behavior of the entire garment, and its implications for creating the DC-PLC system. This method must take into account the unique geometry of the human body by reducing garments into simpler geometric sections. We will start by formulating a model for the conductive fabric behavior, and verifying the model using experimental resistance measurements. This model, along with empirical results, will be used to find a closed-form solution for the DC resistance. The observations will allow us to present design guidelines and suitable applications for this technology. To successfully design the system, we must formulate analytical models of the relevant garment properties. Specifically, analytical DC resistance and AC impedance models must be formulated and compared to experimentally measured characteristics. These models must be derived using fundamental physical equations and must take into account the very unique 3D geometry of the garment.

In addition to determining the behavior and characteristics of the CF garment, we will also find the influence of disturbance sources. For instance, we must be able to characterize and predict noise due to the motion artifact of the user. This must be accounted for, especially when measuring body motion. Moisture can also affect the behavior of the CF and possibly alter the impedance characteristic. Considering user perspiration, as well as environmental moisture sources is necessary when considering this garment for general use. Naturally, ambient heat, light, and noise from sources such as fluorescent light bulbs can also detract from signal integrity. All of this information will be considered in analyzing the garment design. The design guidelines that we determine must be easily generalized. We will introduce design guidelines such that garments can be easily created for users of various sizes and body types.

2. Wearable Health Monitoring

2.1. The need for wearable health monitoring

Wearable health monitoring applications have been in development for some time. There are obvious reasons for why we would want to be able to measure physiological signals with a wearable device. The chief reason is for health and safety concerns. There are a number of populations that would benefit greatly from such technologies, most especially the elderly. Of course there are other groups such as soldiers and health professionals, but the elderly are a special and critical group.

Improved healthcare, medicine, and technology have improved our chances for living longer lives. There are a number of telling statistics. In the second half of the twentieth century, the average life span increased by twenty years, and is expected to increase another ten by the year 2050 [15]. Here in the United States in the year 2000, 12.4% of the population was 65 or older. However, it is projected that, by 2030, this group will make up 19.6% of the population [16]. Global trends will see the 65 and older population growing from 6.9% to 12.0% during this same time period [16]. The elderly population is increasing, and will continue to increase as our health technology improves.

The downside to this increased life expectancy is the quality of life above age 65. This group is increasingly susceptible to chronic illness, injuries, and various other disabilities [17]. In the U.S., the health care cost per capita of those 65 and older is three to five times that of those under 65 [17]. Thus, if current trends continue, there will be an incredible strain on the health care system. The current paradigm of health care will be increasingly difficult to sustain with the ever increasing number of elderly citizens.

Many studies maintain that the care and health of the elderly is improved when they are in environments that they deem comfortable, such as their homes, or in the company of family members. However, in the U.S., two million of the nine million 65 and above are living alone with no one to turn to in times of emergency [17]. In addition, this group often has lower incomes, and limited access to affordable healthcare, goods, services, and living facilities. Thus, we have a significant and growing population of individuals who are not being provided for adequately and are at risk for emergencies.

2.2. Traditional health monitoring techniques

We clearly need new, inexpensive mechanisms for providing care remotely in the home of the elderly. While the demand is now becoming critical, numerous groups have worked on solutions for remote monitoring for a number of years. In the U.S. alone, numerous patents have been issued, with a large number issued in the 80s and 90s pertaining to monitoring of cardiovascular signals. However, many of these early designs have limitations that make this difficult to use with the elderly.

For example, in U.S. Patents 5906004 [18] and 6080690 [19], a garment composed of a cris-crossed structure of conductive fibers and optical fibers for electronic transmission is discussed. These systems presented substantial limitations to how users could move, behave, and properly affix such wearable networks. In U.S. Patent 6102856 [20], a system for monitoring certain vital signs is introduced. This system requires units to be worn on the body in engagement with the skin, which is inconvenient. A user would not be able to use this garment on their own, without extensive special training about how to properly locate and fix the sensors. An elderly user might find the complicated fixturing prohibitive for everyday use. In U.S. Patent 6315719 [21], the system requires the fixturing of sensors to the skin using adhesives. In U.S. Patent 6860897 [22], the system requires implantable devices, which are invasive and uncomfortable.

Some inventors choose to avoid the problem altogether by using sensor nodes with dedicated batteries [23]. Thus, each sensor node is essentially self-sufficient, with its own power source and its own wireless communication components.

Finally, certain inventors have chosen to bypass the problems of routing and fixturing by limiting the user bases for their patents. In U.S. Patent 6315719, the apparatus is specified for use with astronauts whose wearable networks were physically attached to the users. In U.S. Patent 6687523 to [24], the invention is specified for use with infants. Due to the small size of infants, and their limited movements, the routing of cables through Jayaramen's garment doesn't pose a problem. However, expanding this apparatus to the scale of a grown user still requires the use of bulky, metallic cables. Thus, these inventors drastically limit the scope of their inventions to small samples of the population.

In general, prior work in this area suffers form a number of shortcomings that stand to limit their effectiveness in practice, including:

(a) Sensor locations restricted due to the complexity of the routing of the transmission medium. This means the system may be incapable of gathering some relevant data, such as the acceleration at a remote body part.

(b) Adhesively or elastically mounted sensors that are uncomfortable.

(c) Sensors that require trained professionals in order to be fixed to the user's body, and thus force the user to depend on another individual for their quality of life.

(d) Bulky, heavy sensing devices and components that act as impediments to normal daily life and impede normal motion and behavior.

(e) Bulky heavy metallic or optical cables that do not behave like a normal garment and make normal daily life difficult.

(f) Battery driven nodes are bulky and must have batteries periodically replaced.

(g) Limited scope in terms of the types of sensors that can be utilized. This means when newer, perhaps more capable sensors are produced, the systems risk becoming obsolete.

(h) Limited scope in terms of the lack of support provided for actuators. This limits the types of applications for such networks, such as rehabilitation.

(i) Limited scope in terms of system components useful only for monitoring. This limits the types of applications for such networks, such as information displays and entertainment.

(j) Limited scope in terms of the directionality of the wireless transmission. None of the former systems had bi-directional communication capabilities. This limits the utility of such a system since the remote capture and storage mechanism is not permitted to send information to the wearable network in order to give feedback based on the network node outputs.

(k) Limited scope in terms of the user base. This means the majority of the population cannot use the described apparatus.

For these reasons, the known devices and systems are not suitable, or can only be used with serious limitations, for long-term continuous monitoring of a user. Furthermore, such known systems are not well suited to being reactively adapted to flexible and varied demands of the system.

2.3. Challenges of health monitoring

As much of this work indicates, we are still a long way from a truly wearable, non-invasive, non-intrusive wearable health monitoring system. In the design of our garment, our tactic is not simply to apply off the shelf electronic components to the human form. Rather, our goal is to evaluate what is wearable and comfortable, and figure out how to build electronic components that fit with such requirements.

Much information can be gained from qualitatively looking at the idea of 'wearability.' Gemperle et. al. discuss wearability by referring to human-factors based metrics [9]. While some metrics are obvious, others are less obvious but equally important. The metrics with which we are concerned, and their application to the elderly, are the following; component *placement* is very important. With the elderly, there are certain physiological signals, such as heart rate, which are extremely relevant. We must place sensors and electronic components at locations where the relevant physiological signals are most effortlessly obtained.

Form shape is also extremely important. The human body is round and soft, with few straight lines or sharp corners. Components made to be placed on the body should also fit this form factor so as not to cause harm or discomfort to the user.

Human motion must also be considered. Sensors or components should not be placed in the range of motion. For instance, a bulky component should not be placed on the hip where a swinging arm might hit it.

Proxemics is a less obvious concern, but extremely important for the elderly. Proxemics refers to our perception of where we are physically located. That is, we avoid bumping into walls not because we are watching the wall to ensure that we are far enough away, but rather because we have a mental perception of where we are relative to objects in our environment. This mental perception can be altered and reduced if heavy or bulky objects are attached to the body, leading to collisions with objects in the environment. For the elderly, who are often more rigid and brittle, such collisions can be critical.

Sizing must also be considered. In our case, we would like to minimize the size of all components. Additional metrics include weight, accessibility, and aesthetics. All of these metrics are taken into account for the design of our system. By using conductive fabrics along with DC PLC, we have chosen technologies that allow for the reduction of the

number of components, the reduction of overall weight and bulk, and the minimization of resources necessary to transmit data and power. The distributed nature of the system results in our ability to distribute the weight and bulk of the components over the body.

2.4. Our Solution: DC-PLC using Conductive Fabrics

2.4.1. Addressing existing problems

Our solution to the problem is to combine DC power-line communication and conductive fabrics. We create a wearable health monitoring device that addresses the problems mentioned in Section 2 while taking into account the metrics mentioned in Section 3. The conductive fabric sheets of the garment can cover the entire body. Thus, sensors can be fixed anywhere and will have an electrical connection to power and data. Thus, we have great freedom of sensor locations for our system. Because the garment covers the body, it has a pervasive physical presence. Thus, sensors are held in their proper locations by the conductive fabric. This greatly simplifies fixturing; the user need only put on the garment and the sensor nodes will accurately self-locate. The physical construction of our garment is similar to the approaches of [25] and [12].

The DC PLC system allows us to distribute the system weight and bulk according to the body's load-carrying capabilities. Because we place a single battery at the lower back, each sensor node need not have its own local battery. Further, using the conductive fabric allows us to eliminate most metallic and optical cables, in favor of the lighter more breathable silver-coated nylon. This reduces the physical burden on the user.

One may at this point ask why 'wired' nodes are used instead of wireless nodes. That is, why not allow for each node to have its own dedicated wireless connections, as is done in [23]. We choose wired rather than wireless to minimize user burden.

When considering power delivery, with our system, we simply have to recharge a single battery pack. Thus, for recharging, the user simply removes the garment and plugs it in. If batteries are used at each node, they must be replaced whenever they die. For large numbers of sensors, battery maintenance can become significant. Further, while battery sizes are shrinking, there is still significant bulk associated with them, and as the number of nodes increases, so does the number of batteries.

For transmission, the primary reason we choose wired communication is to avoid interference. We have only a single wireless channel, versus the numerous that would be required for a system of wireless nodes. Further, we can easily coordinate the signals using wired transmission. Coordinating and synchronization are much more difficult with wireless nodes. Note also for increased range, the wireless transmitter must be of a certain size. A single larger transmitter at the lower back does not impose a significant burden, where such a transmitter at each node would be restrictive in size.

Our modem design allows for bidirectional communication, increasing versatility and utility. Higher priority sensors can be asked to send their information packets more often, while lower priority sensors can be polled less often, but interrupt transmission in times of emergency. Thus, not only do the sensors have the ability to send their outputs to the centralized components, but we can implement complex sharing and energy saving techniques by polling sensors only when necessary. We can also implement techniques that have been proven in other shared-medium networks, such as that of wireless cell phones. We can also utilize feedback to more accurately care for and evaluate the patients' condition.

All of these factors combine to make a device that can be applied to a broad population. Though we target the elderly, all of the features of our device make it applicable for and useful to a wide range of populations, such as fitness trainers and emergency response professionals. Such versatility is due to our careful consideration of the wearability metrics.

2.4.2. Accommodating wearability metrics

Specifically, we have designed the shell for the sensor nodes and centralized components to fit with the form factor of the human body. The sensor shell has rounded edges and an egg-like shape, to ensure the electrical and mechanical sensor node components are not significantly cumbersome for the user. The same is true for the centralized components which are conformed to the shape of the lower back.

We also ensure that normal motion, specifically walking and moving around, are not impeded by sensors. Certain areas of the body have relative motion to one-another. Consider the hip and wrist, which have relative motion to one another when the arm swings during the normal gait cycle. We place no sensor in these obvious motion paths to

avoid forcing the user to augment their natural behavior and prevent them from striking themselves.

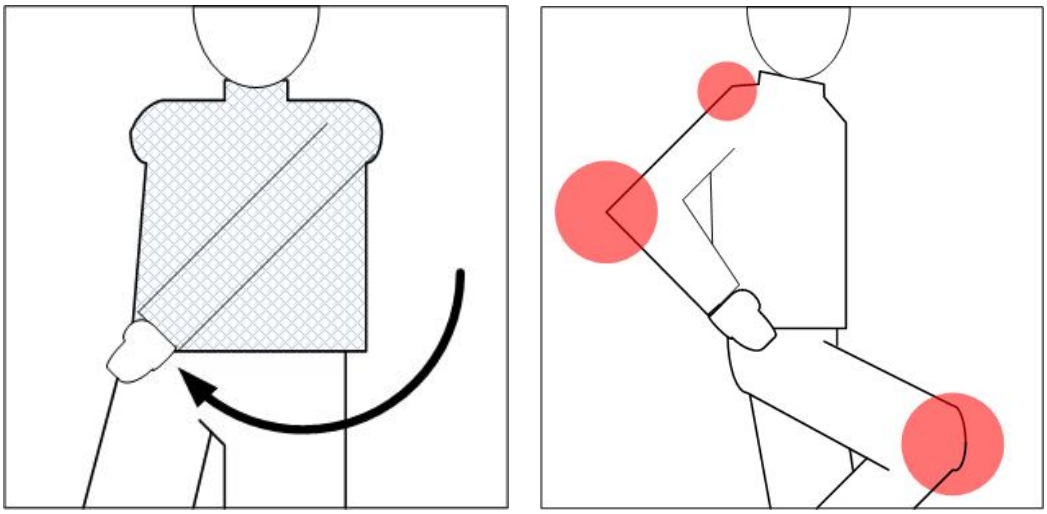

Fig. 5 Illustration of relative motion of arm to the hip and the extreme points of the body during the walking gait

This not only helps in allowing for motion, but helps to ensure that our proxemic sense is not violated. We minimize the size of all body-mounted components, and also avoid placing sensors at 'endpoints.' That is, a shoulder, elbow, or knee is the extreme point of the body during different phases of the normal gait. To ensure we don't drastically alter the user's physical perception of them self, we avoid these locations for sensor placement.

Finally, the obvious issue of sizing is has been taken into consideration throughout the construction of our device. We have always striven to minimize the size of all components in order to satisfy the wearability metrics and also to minimize user burden. This is done by using circuit design techniques which minimize the size and number of required electrical components. In the interest of minimizing bulk, we also use printed circuit boards (PCBs) along with surface mount (SMT) component packages.

3.DC Power-line Carrier Communication

When determining the best way to minimize user burden in such systems, there are certain techniques that might be used. One such technique is minimizing the size of all components, which can be done as previously described by using PCBs and MEMS-based sensors. However, in considering existing technologies, one of the biggest problems is actually the cabling and wiring. The metallic cabling can be heavy, bulky and restrictive. Thus, reducing the amount of this cabling greatly reduces the total burden on the user. To this end, we take inspiration from in-home AC power-line communication techniques. Such in-home techniques have gained popularity in Asia and Europe as methods for creating home automation. The idea is based on the expense associated with installing local high-speed data lines. Instead of doing so, it is more convenient and cost-effective to use the pre-existing cables and wires used for power transmission. Power line communication (PLC) consolidates the need for separate power and data lines by sending data over already existing power lines. Thus, PLC is an effective and proven method for reducing cabling, and in our wearable systems, for reducing user burden.

The bulk of PLC research to this point has been done in regards to in-home networks. In-home AC PLC has been shown to be a useful and economically viable technology in recent years [26][21]. However, there are a number of limitations to this PLC method. The large power transformers that are used to step down power from outdoor power lines to individual houses attenuate high frequency signals required for broadband communication [21]. Also, residential loads such as dimmers, switching power supplies, and other communication media often contribute noise in ranges anywhere between 100Hz and 1MHz [28]. Depending on what loads are connected to the line, the line characteristics of impedance, noise, and signal attenuation vary over a wide range and are highly complex and non-linear.

Another problem for AC PLC is bandwidth limitations due to regulation. In most countries, transmissions on the commercial power line are allocated to the range between 3Hz and about 500kHz. For instance, the Federal Communications Commission (FCC) in the United States allows power line transmissions in the 10 – 450kHz range, while European authority CENELEC currently allows for transmissions in the 3 – 148.5kHz range [29][30]. Communication above these ranges is shared by many other operations, including AM radio and amateur broadcasters

[31]. The current bit transmission rate for PLC is severely limited due to these restrictions and regulations. Thus, traditional PLC has numerous difficulties that have limited its success so far.

We wish to take advantage of the positive features of AC PLC; namely, the savings in time for installation and maintenance, the simplicity, and the reduction of the required amount of cabling. DC PLC requires only a ground and supply line for transmitting data and power. However, we must face the fact that the design of our DC PLC system will differ drastically from that of the AC systems used in homes. The details of this design follow.

3.1. DC Power-line Communication Network

3.1.1. Architecture

Our PLC architecture is intended to apply to a confined, local system where DC power is supplied to all of the nodes. Such closed environments with shared DC power can be found in robotic systems, vehicles, and wearable systems, which contain a number of actuators and sensors. As shown in Fig. 2, a single power bus line originating in a DC power supply extends to a number of nodes, e.g. actuator and sensor units. Data to be transmitted, such as encoder readings, sensor signals, and control commands, are coded, modulated, and sent over the DC power bus by superimposing high frequency signals on top of the DC power supply voltage. Each node is equipped with a modem for superimposing and tapping the signal as well as coding and modulating the signal. A single DC voltage line, that we term the Consolidated Power/Signal (CPS) line, and a ground line are sufficient for connecting all the nodes. This system is represented schematically in Fig. 6.

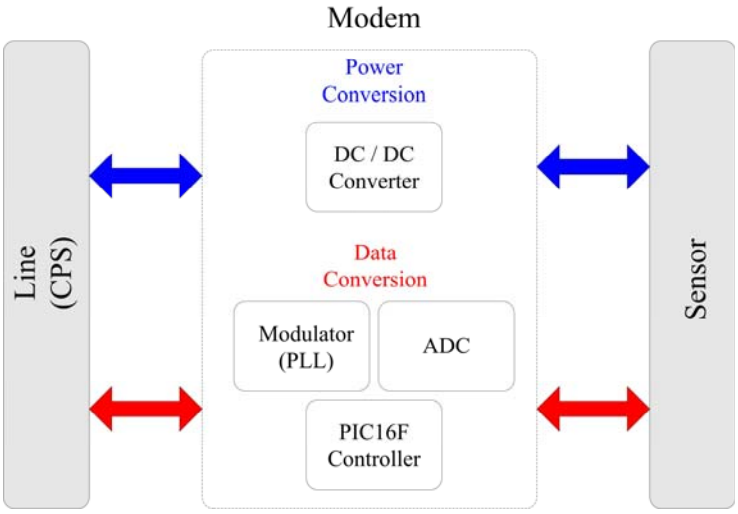

Fig. 6 Architecture of DC power bus communication system

Note that, unlike traditional layouts, where drive amplifiers are placed inside a control console and long cables are used for connecting the actuators to the drives, this DC power bus network entails distributed modulation and control components placed near the sensors or actuators. The load conditions are known, or at least predictable. Modems for transmitting signals can be designed based on the previously quantified characteristics of loads and noise sources. This allows for the reliable broadband communication needed for multiple nodes.

3.1.2. Technical Issues

The above architecture may have numerous variations and diverse levels of sophistication. Here, we focus on the basic physical layer and hardware modem design suitable for DC PLC. The obvious driving question is whether or not the DC bus can be used as a broadband communication medium. Interferences with the DC power supply might make the power-line communication infeasible or difficult. There are two possible failure scenarios that must be considered. The first is severe attenuation of the data signal. There is a possibility that the low impedance of the DC power source will draw too much signal current and substantially attenuate the data signal. Additionally, most DC power supplies have active regulators, which act to minimize ripple in output voltage or current. These regulators might also attenuate the data signal.

We must ensure that these adverse effects of using the DC bus can be substantially neglected over the frequency ranges in which we hope to operate.

3.2. Modem Design and Analysis

3.2.1. Hardware Requirements and Problems

Given that the DC power-line is feasible to use as a communication medium, we now determine a method for fully exploiting the features of the DC PLC technique. Specifically we are interested in networking a large number of actuators and sensors, as described previously. There are two significant technical challenges; Signals must not attenuate significantly although many nodes are connected to the CPS line. Furthermore, the line impedance must remain high enough to keep the driving current low even when large numbers of nodes are connected to the CPS line. To meet these goals, an efficient modem design will be presented in this section.

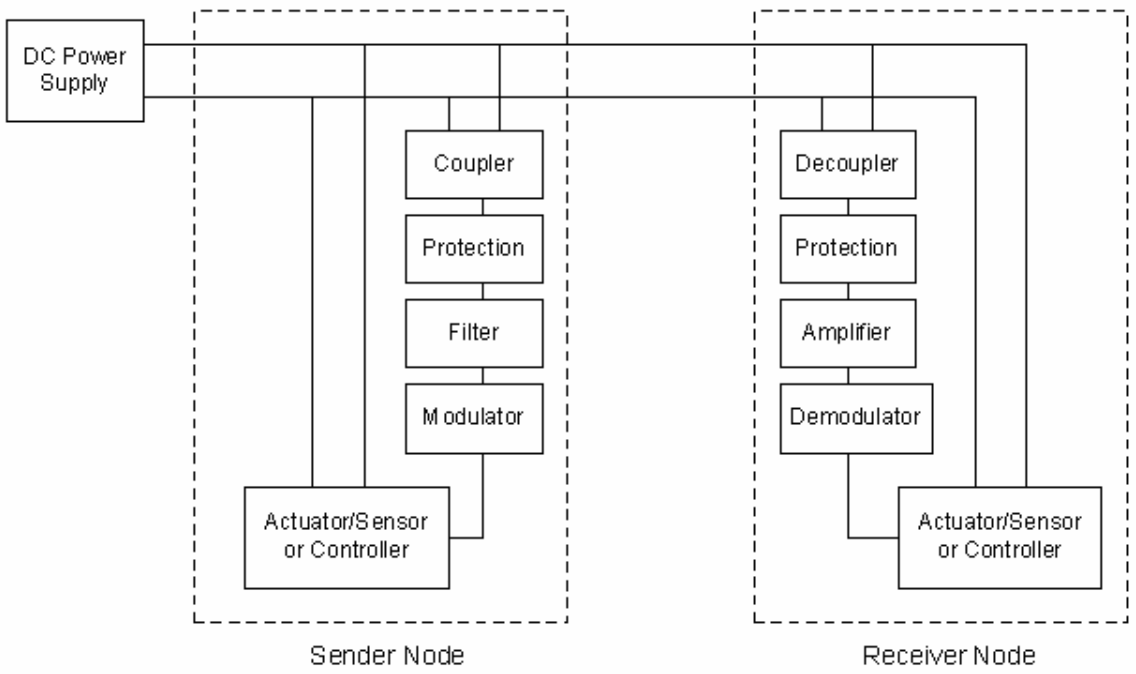

Fig. 7 Block diagram of DC Bus transmission components

Fig. 7 illustrates the major components involved in sender and receiver nodes. The modulator, demodulator, amplifiers, and filters are all standard modem components. However, because this modem is for use in a PLC system, additional protection, coupling, and decoupling components are required. The primary functional requirement for these components is the ability to superimpose the data signal onto the DC power-line. Additionally, we must be able to block DC voltage and current to prevent saturation of and damage to the modem. The protection must not, however, impede the combination (and separation) of the data and power by the coupler (and decoupler). The components must also maximize signal power deliver to the receivers and have a minimum insertion loss. Finally, we wish to be able to communicate with a large number of nodes, despite the fact that they are paralleled on the bus line.

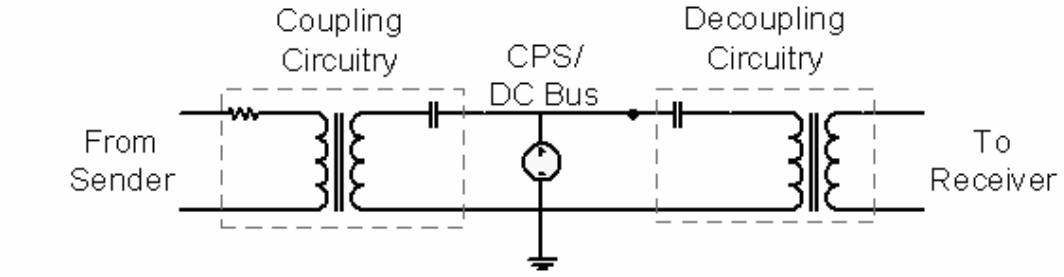

Fig. 8 Standard coupling/decoupling circuitry

Fig. 8 depicts a standard coupling and decoupling circuit used for ac power-line communication [32]. The transformer electrically isolates the data and power sources. The capacitor is used to block DC power from the modem transmit– and receive–components. The transformer and capacitor provide a path for the ac data signal to be superimposed on the DC power-line. This standard circuit, however, does not meet our requirements due to the parasitic effects of the transformer at high frequencies. Parasitics such as winding resistance and magnetizing inductance, typically ignored in the ideal transformer model, cannot be neglected for our high frequency application. At high frequencies, these parasitics cause insertion losses, or resonances that detract from ideal behavior and draw non-negligible amounts of current. This current flows from the supply line directly to ground, and never passes to the load, causing substantial attenuation of the data signal. As the number of nodes increases, this attenuation can critically reduce the data signal level on the CPS until it is too low to drive the receiver nodes.

3.2.2. Use of Transmission Line Transformer

To minimize the insertion losses associated with the coupling and decoupling circuits, we propose to apply the theory of transmission line transformers, which have substantially lower insertion losses than traditional transformers for various applications [33], [34]. The basic building block of the transmission line transformer (TLT), shown in Fig. 9a, transmits energy to the load by use of transverse transmission line mode. The functionality of the circuit depends on the grounding and the connection of the terminals 1 through 4. Placing a load across terminals 2 and 4, and varying the grounded point can produce a phase inverter or delay line, for example.

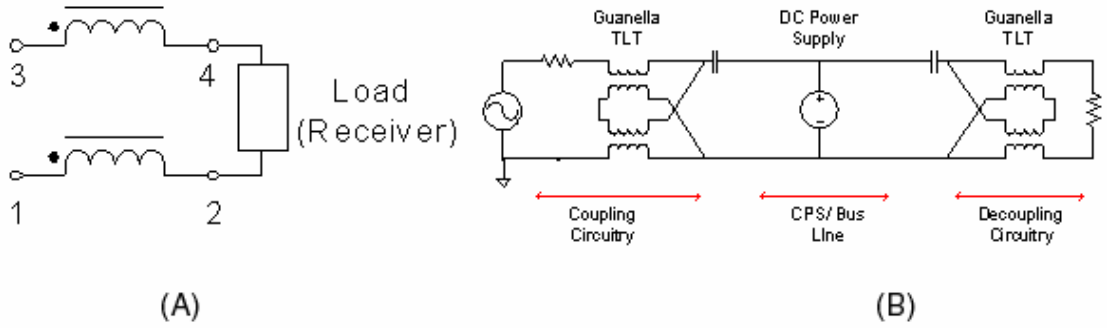

Fig. 9 Basic building block for transverse transmission mode circuits and coupling and decoupling circuits with transmission line transformer

A major advantage of TLTs is that the parasitics associated with the transformer, many of which show up in parallel with the windings, are now in series with the load. Thus, even when these parasitics draw non-negligible current at high frequencies, the current is ultimately delivered to the load. As stated, a standard transformer allows this current to flow directly to ground, bypassing the load. Thus, the TLT is less susceptible to losses due to parasitics.

TLTs have not yet been used in power-line communication systems. Here, we present the design a high-fanout modem by exploiting the features of the TLT. A class of TLT configurations known as Guanella TLTs transforms apparent impedance, as seen from the CPS line. Thus, we can make the power supply input impedance, Z_{ps}, appear much higher than that of the receivers, Z_r. The system schematic, including the Guanella TLT, is shown in Fig. 9b. This Guanella TLT performs a 1:4 impedance transformation. As will be shown later, a 1:4 transformation is adequate for our application. TLTs with a variety of parameters are available from multiple vendors. For the engineer without the time or resources to build a custom TLT, we will later outline a procedure by which the ideal TLT parameters can be found. Subsequently, the user can select an off-the-shelf TLT that best meets the requirements. However, for the purposes of modeling the system, we will first assume that we have the ability to tune our own TLT according to the methods described in [33]. Our design requirements for the tuning of these parameters will result from a careful analysis of the TLT functionality

3.2.3. TLT Modeling

We start by analyzing the frequency characteristics of a single TLT and build a lumped parameter model competent to depict parasitic dynamics in a relevant frequency range. The TLT model we used is based on that presented by Kuo [34]. Traditional TLT models are accurate only over limited frequency ranges. Often multiple models are required to predict the operation of a TLT over a wide frequency range (up to MHz). However, Kuo's model can predict both the low and high frequency responses of the TLT. This model incorporates the magnetizing inductance and winding resistance of the transformer in addition to the TLT windings. The difference in our formulation is due to the fact that a basic 1:1 isolating transformer is modeled in [34], whereas a 1:4 Guanella style transformer is needed. Nonetheless, the applicability of Kuo's model to our Guanella TLT is verified by close agreement between experimental and model results. Based on this model, the ideal TLT circuit of Fig. 9b is redrawn in Fig. 10 to explicitly include the winding inductance, L_w, and winding resistance R_w.

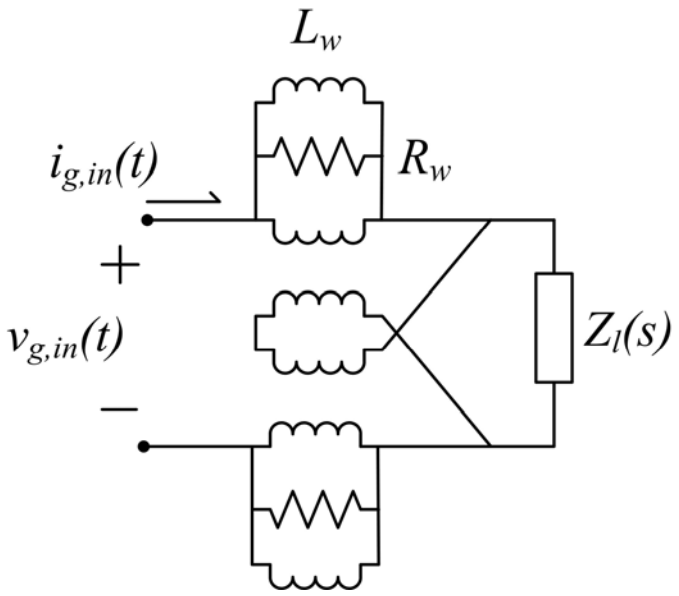

Fig. 10 Guanella transmission line transformer model accounting for magnetizing inductance and winding resistance

Let $i_{g,in}(t)$ and $v_{g,in}(t)$ be the Guanella input current and voltage, respectively, and Z_l the equivalent load resistance placed across the output terminals. Replacing the winding inductance, L_w, with the magnetizing inductance, $L_m = 2L_w$, and applying impedance-based modeling techniques, the TLT impedance $Z_t(s)$ seen at the input terminals can be written as

$$Z_t(s) = \frac{V_{g,in}(s)}{I_{g,in}(s)} = \left(\frac{8R_wZ_l}{Z_l + 2R_w}\right)\frac{s}{s + \left[\frac{2}{L_m}\left(\frac{R_wZ_l}{Z_l + 2R_w}\right)\right]} \quad (1)$$

(see Appendix 10.2 for derivation)

We experimentally determine the values for L_m and R_w. Impedance data was collected with an HP4194A impedance analyzer with bandwidth of 100MHz. The TLT was terminated with various resistors, and the impedance of the TLT-and-resistor combination was measured. The experimental values for the parasitic components were plugged into the $Z_t(s)$ function to obtain a numerical solution. The magnetizing inductance, 5μH, and the winding resistance, 450Ω, were used along with various resistive terminations to produce Fig. 11. Note that, in Fig. 11 there is close correlation between the experimental and model performance for the TLT for load resistances of 50Ω, 100Ω, and 200Ω.

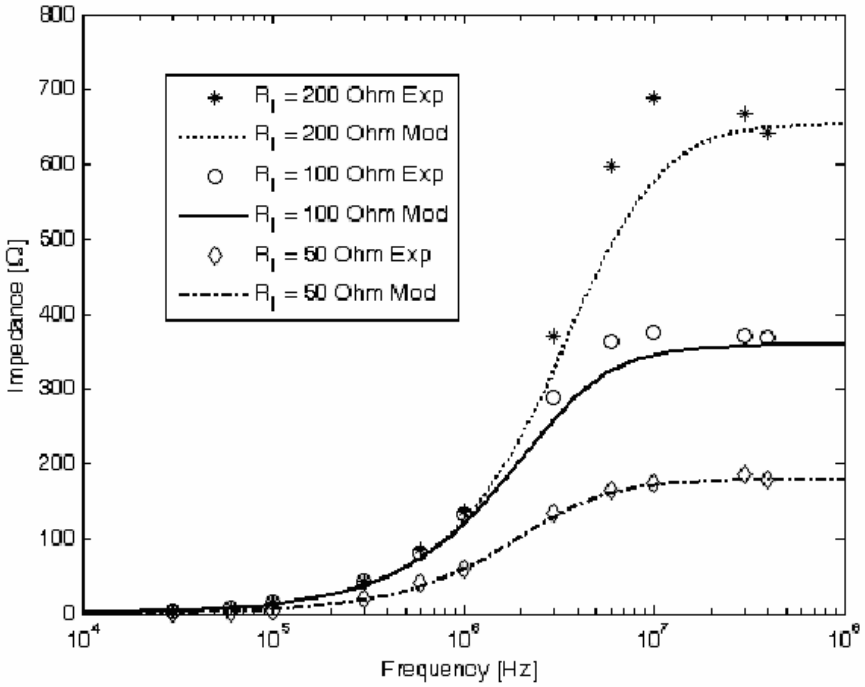

Fig. 11 Impedance of transmission line transformer with terminating resistor

3.2.4. System Performance

Having verified the TLT model, the next step is to evaluate the entire system performance when a number of nodes are connected to the CPS line through the Guanella TLT (See Fig. 12). Note that the Guanella TLT is arranged in symmetric form for the sender and the receivers. Specifically, we are interested in broadcasting data to many receiver nodes. Gain and impedance must be evaluated as the number of nodes *n* becomes large. The impedance seen from the sender-side terminals is given by:

$$Z_n(s) = \frac{V_a(s)}{I_a(s)} \tag{2}$$

The frequency transfer function from the input voltage of the sender to the output voltage of a receiver is given by:

$$G_n(s) = \frac{V_d(s)}{V_a(s)} \tag{3}$$

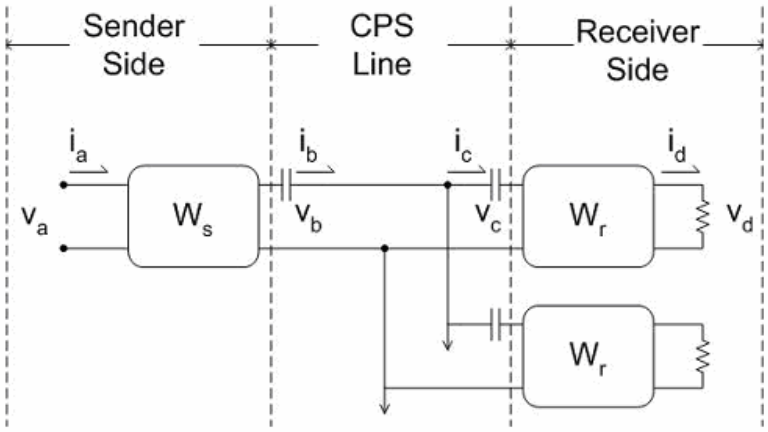

Fig. 12 Circuit divided into sections: sender side components, CPS, receiver side components

Note that $V_a(s)$ is the sinusoidal voltage input generated by the sender and $V_d(s)$ is the voltage observed at one of the receivers at steady state. $I_a(s)$ is the sender-side current associated with the voltage $V_a(s)$.

To obtain (2) and (3), it is convenient to use a 2x2 matrix formulation relating input current and voltage to output current and voltage. This allows us to evaluate the system characteristics independent of the loads and on a component-by-component basis. As shown in Fig. 12 the whole system can be divided into the sender TLT, the receiver TLT, and the line characteristics including the blocking capacitor. We use (1) to write the equations of the sender side Guanella TLT in 2x2 matrix form,

$$\begin{bmatrix} V_b \\ I_b \end{bmatrix} = \begin{bmatrix} & W_s & \end{bmatrix} \begin{bmatrix} V_a \\ I_a \end{bmatrix} \tag{4}$$

where

$$W_s = \begin{bmatrix} 1/2 & 0 \\ -\left(\dfrac{1}{4R_w} + \dfrac{1}{2L_m s}\right) & 2 \end{bmatrix} \tag{5}$$

Similarly, the impedance of the receiver-side TLT can be used to write;

$$\begin{bmatrix} V_d \\ I_d \end{bmatrix} = \begin{bmatrix} & W_r & \end{bmatrix} \begin{bmatrix} V_c \\ I_c \end{bmatrix} \tag{6}$$

where

$$W_r = \begin{bmatrix} 2 & 0 \\ \left(\frac{1}{4R_w} + \frac{1}{2L_m s}\right) & \frac{1}{2} \end{bmatrix} \tag{7}$$

Note that $I_c(s)$ is the current flowing to each receiver at steady state. In most robotic systems, the length of the CPS line is at most 10m. The phase shift due to the distributed impedance of the CPS conductor is not significant as long as the carrier frequency of signal transmission is lower than 10MHz. Assuming that all the blocking capacitors involved in both sender and receivers are the same and that the line impedance is dominated by the blocking capacitance, we can relate the receiver-side voltage and current to those of the sender-side as;

$$\begin{bmatrix} V_c \\ I_c \end{bmatrix} = \begin{bmatrix} & W_{line} & \end{bmatrix} \begin{bmatrix} V_b \\ I_b \end{bmatrix} \tag{8}$$

where

$$W_{line} = \begin{bmatrix} 1 & -\left(1 + \frac{1}{n}\right)\frac{1}{sC} \\ 0 & \frac{1}{n} \end{bmatrix} \tag{9}$$

Combining (4), (6), and (8) gives;

$$\begin{bmatrix} V_d \\ I_d \end{bmatrix} = \begin{bmatrix} W_r \end{bmatrix} \begin{bmatrix} W_{line} \end{bmatrix} \begin{bmatrix} W_s \end{bmatrix} \begin{bmatrix} V_a \\ I_a \end{bmatrix} \tag{10}$$

Solving this for the impedance V_a/I_a subject to the load resistance $V_d = R_d/I_d$ yields;

$$Z_n(s) = \frac{As^3 + Bs^2 + Cs}{Ds^3 + Es^2 + Fs + G} \tag{11}$$

where $Z_n(s)$ is the total system impedance (See Appendix 10.3 for coefficients).

As the number of nodes, n, tends to infinity, the impedance function reduces to;

$$Z_\infty(s) = \lim_{n\to\infty} Z_n(s) = \frac{b_1 s^2 + c_1 s}{d_1 s^3 + e_1 s^2 + f_1 s + g_1} \tag{12}$$

These coefficients are dependent on two effective time constants, $\tau_1 = R_w C$ and $\tau_2 = \sqrt{L_m C}$. Typically, the resistance order of magnitude is hundreds of Ohms, whereas the capacitor is in 10^{-9}Farads, and the inductance is 10^{-6}Henries. Thus, the time constant τ_1 is on the order 10^{-7}s and τ_2

is on the order $10^{-7.5}$s. We use these values to find $b_1 << c_1$ and $d_1 << e_1, f_1, g_1$. Simplifying the coefficients, $Z_\infty(s)$ can be further simplified to:

$$Z_\infty(s) \cong \frac{c_1 s}{e_1 s^2 + f_1 s + g_1} \tag{13}$$

Similarly, the gain function $G(s)$ for n receivers is given by;

$$G_n(s) = \frac{\alpha s^3}{\delta s^3 + \gamma s^2 + \varsigma s + \varepsilon} \tag{14}$$

(See Appendix 10.4 for coefficients)

As n approaches ∞, the gain function reduces to;

$$G_\infty(s) = \lim_{n\to\infty} G_n(s) = 0 \tag{15}$$

The fact that $Z_\infty(s)$ goes to a constant value and that $G_\infty(s)$ goes to zero make logical sense. As n goes to infinity (and the load resistance goes to zero), the impedance seen from the sender side will just be a function of the sender-side components. Similarly, when the load resistance goes to zero, the output voltage goes to zero, and thus, the gain goes to zero.

The plot in Fig. 13a shows the frequency dependent impedance for varying numbers of receivers, n, which has a very distinct peak. Specifically, as the number of nodes increases, the peak amplitude increases, the peak frequency decreases, and the impedance at high frequencies decreases. It should be noted that, as the number of nodes tends to infinity, the impedance peak amplitude becomes extremely high. The relevance of this fact will be addressed in the following.

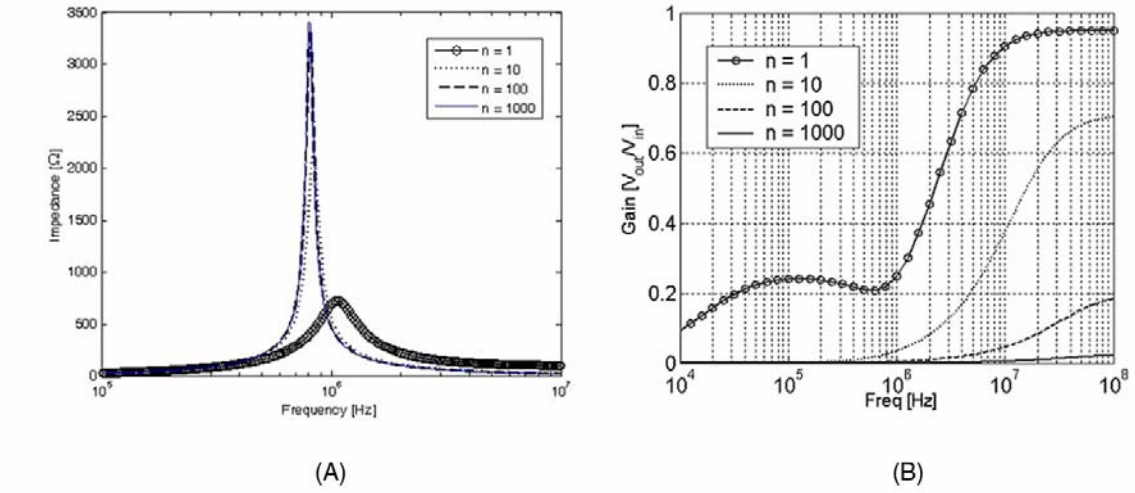

Fig. 13 Impedance and gain as a function of n

The physical sense of this peaking behavior can be explained with Fig. 14. Recall the impedance form depicted in (11). Equation (11) simplifies to (13) as *n* approaches infinity. The peak frequency for this simplified expression is given by $\omega_p = \sqrt{g_1 / e_1}$. Referring the parameters of e_1 and g_1 from the appendix reveals that the value can be approximated by a constant multiplied by $1/\sqrt{L_m C} = 1/\tau_2$. This implies the resonant behavior of a parallel *L-C* circuit.

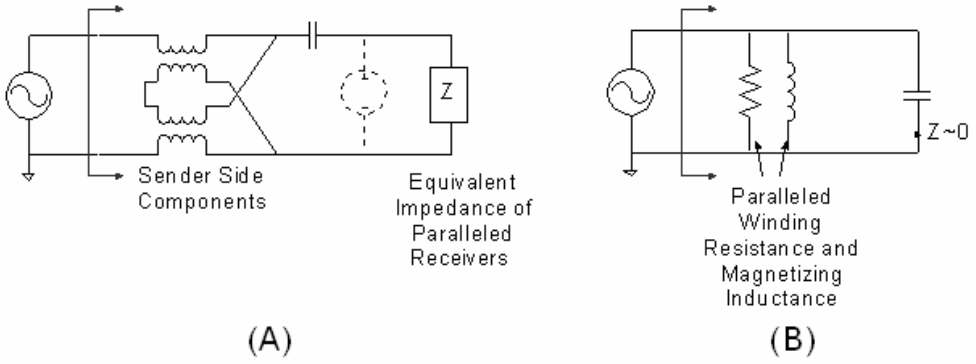

Fig. 14 Simplified circuit schematic and the resulting equivalent circuit model for large *n*

Looking again at the circuit, we see that, as more loads are placed in parallel, the equivalent load impedance of approaches zero. This effectively changes the circuit to that of Fig. 14b. The coupling capacitor is in parallel with the winding resistance and magnetizing inductance of the TLT. The impedance function of this parallel *R-L-C* circuit matches the form of the impedance function $Z_\infty(s)$. In the equivalent *R-L-C* circuit, current must always pass through the receiver impedance as well as the coupling capacitor. Once again, the use of the TLT ensures that current will always flow into the load. Note that the typical transformer orientation of Fig. 8 allows the current to flow right back to the source without passing through the load. Thanks to the TLT, we are able to manipulate the impedance values even for large gain and large numbers of actuators *n*.

3.2.5. High Fanout Design Protocol

This implies that the proposed modem design using a TLT would allow us to transmit signals to a large number of nodes simultaneously without drastically lowering the output impedance. Refer again to Fig. 13a. Even for large values of *n,* there remains a regime over which the impedance is high. Due to the TLT, this peak will always remain in the impedance curve. Typically, when fanout becomes large, the impedance goes to zero, and infinite current is

required to drive the system. However, in our apparatus, when fanout becomes large, there is always a frequency range for which only a nominal amount of current is required to drive the system. Of course, this frequency range is only useful if the gain of the transfer function, $G_n(s)$, is not too small. Therefore, we must examine the gain in the frequency range where the impedance remains high. Specifically, to use this high impedance value, we must ensure that the dip that is apparent in the gain curve of Fig. 13b is separable from the peak in the impedance curve by using the design parameters involved in the TLT modem.

Looking at the gain function, we find that the dip frequency is governed by the load resistance, R_d, and coupling capacitance, C. As mentioned, the peak is a function of the time constant, τ_1.Thus, tuning the L_m, C, and R_d parameters allows us to separate the impedance peak and gain dip. To verify this, the authors conducted a set of experiments in which the value of magnetizing inductance was changed from 0.5μH to 5μH to 50μH. In the impedance plot, the peak value changes from 2MHz to 1.5MHz to 850kHz. However, the dip in the gain curve changes from 1.5MHz to 900kHz to 800kHz.

Thus, tuning the TLT components gives us the ability to separate the impedance peak and gain dip, and as a result, allows us to use the high-fanout design protocol. This unique contribution, based on the use of the TLT, allows us to broadcast information to multiple receivers simultaneously.

3.3. Implementation and Experiments

3.3.1. Prototype

A proof-of-concept prototype system has been developed to demonstrate the proposed approach and verify the design and analysis methods. Fig. 15 depicts the modem used at each node of the system (a circuit diagram can be obtained from the authors directly). It consists of a transmission line transformer, a coupling capacitor, a microprocessor (PIC16F84), a signal modulation chipset, and a DC/DC converter. A DC servomotor equipped with a 12V PWM amplifier was connected to each node. The PIC is capable of performing computations for local feedback control as well as for communication with the central control unit through the CPS line.

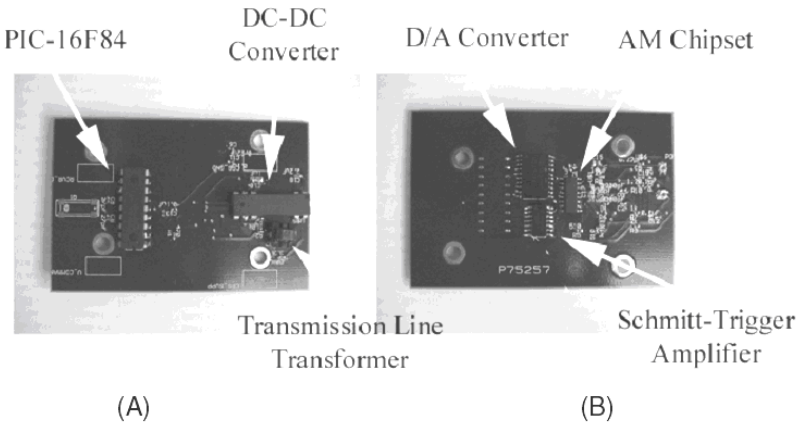

Fig. 15 Top and bottom views of prototype modem

3.3.2. Design

In this section a few design issues critical to the proposed method will be addressed, and experiments using the prototype will be conducted in the following section to verify the theoretical results and demonstrate the feasibility of the method. The relevant issues are the selection of the transmission frequency and the selection of modem components.

3.3.2.1. Selection of Coupling Circuit Component Values

We design the coupling circuitry based on the analysis described in the previous section, frequency restrictions imposed by the power supply and sensors, and filtering and impedance matching conditions. The design parameters are the transmission carrier frequency f, the coupling capacitance C, and the receiver load impedance Z_l. In addition, we have the TLT impedance $Z_t(s)$, which is a function of its magnetizing inductance Lm, and parallel resistance R_w. The design procedure is as follows.

To determine the TLT parameters L_m and R_w, we first notice that the TLT has high pass filter characteristics. The cutoff frequency is a function of these two parameters and should be tuned such that only transmission frequencies (i.e. the mega-Hertz range as mentioned in the previous section) can pass to the CPS. Thus, the frequency f is found based on the desired transmission rate. We see, from Fig. 11, that regardless of load impedance, there is a certain frequency below which no frequency signal can pass. This can be used to select R_w and L_m. Having determined L_m and R_w, the next step is to determine $Z_d(s)$ by evaluating the operating current and voltage for the signal processing components.

The first step after receiving the signal is to demodulate it. At the demodulator, the signal is divided between two ports that can sink a total of 250mA. The input voltage limit is 5V, which gives a minimum input impedance of 20Ω. This is the value used for $Z_c(s)$. Having found $Z_c(s)$, we can next find the value for C. The receiver impedance is the TLT impedance of (1) added to the impedance of the coupling capacitance, $1/sC$. For transmission line impedance matching, the impedance of the line must be matched to the impedance of the load to ensure maximum power deliver. Thus, $Z_t(s)$ is equal to the impedance of the chosen communication medium (75Ω, in our case). Setting the impedance of the coupling capacitor and receiver equal to 75Ω, the only unknown is the capacitance value C. The parameters for our system were specified using this method and are presented in Table 1;

Table I. Coupling circuit parameter values

Parameter	Value
C	3.9 nF
L_m	5.1μH
R_w	450Ω

3.3.3. Experimental Evaluation

Using the coupling circuit, experiments were conducted to demonstrate the feasibility of the method. Fig. 16a shows a source digital signal before modulation and transmission, and Fig. 16b shows the demodulated signal received by one of the nodes connected to the CPS lines. Here, the pulse interval is 10μs, and the transmission rate is 100kbps. Although the high frequency noise of the power supply is visible in the received signal, the data is correctly decoded. The signal amplitude reduced only to 50% of the source amplitude. This confirms our predicted value of gain depicted in Fig. 13b. Although 30 nodes were connected, the signal gain remained high. The SNR of the received signal was 18.1.

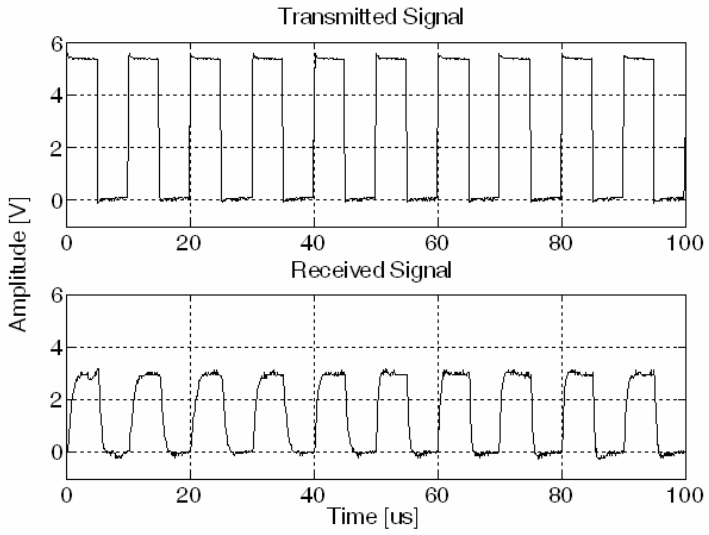

Fig. 16 Original transmitted digital signal and received signal

The key technical feature of the proposed method is to exploit the peak signal transmission impedance that is created through careful selection of coupling circuit parameters and the carrier frequency. It is important to note that this peak is obtainable even though we use a normal amplifier on the sender side. We verify this peak experimentally, and have presented the results for one and for thirty receivers in Fig. 17. We can evaluate (11) using the parameter values determined by the above design procedure. We can compare this result to the experimental data obtained using the impedance analyzer and the experimental apparatus. Shown in Fig. 17a is the comparison of the signal transmission impedance for a single node, $n = 1$. Fig. 17b is the result for the large degree-of-freedom robot with $n = 30$. The experimental values are shown with diamonds, and the model with the solid line. Excluding high frequencies, there is good agreement between the experiments and the model. The discrepancy at the high frequencies is due to the equivalent series resistance (ESR) of the coupling capacitor, and it is found experimentally that a coupling capacitance ESR value below 100Ω is adequate to elucidate the flat, high frequency behavior. The actual behavior is accurately predicted using our model and our design procedure.

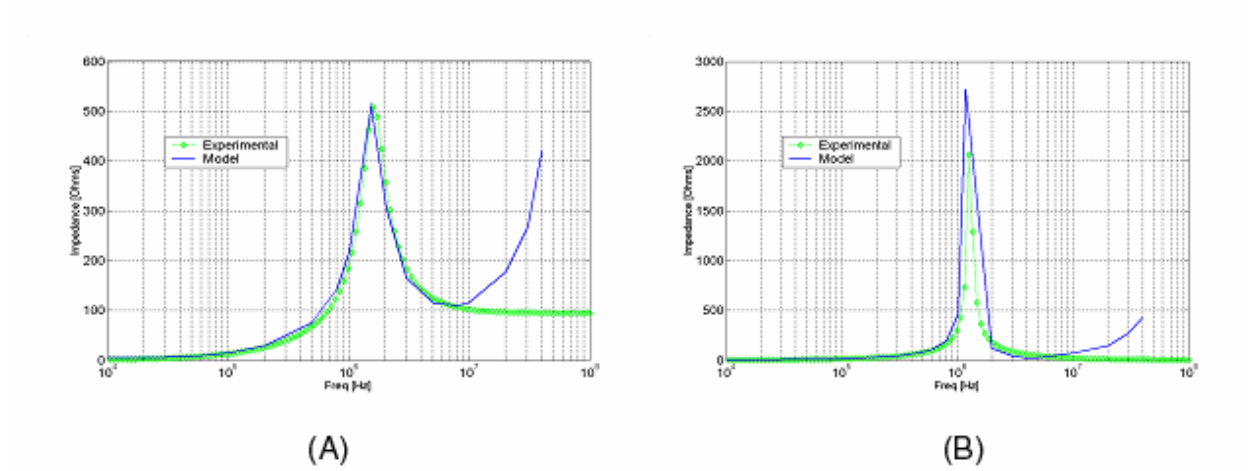

Fig. 17 Signal transmission impedance viewed from sender for n=1, a single node, and n=30, thirty nodes

The question may arise as to how well our model predicts the limiting case as *n* becomes large. To address this question, it is helpful to look at the model and experimental results as a function of *n.* Specifically, we can look at the magnitude of the impedance peak, and the frequency at which it occurs. We showed earlier that the peak magnitude and frequency reach a maximum and minimum value (respectively) well before *n* reaches infinity. We now try to calculate the error in the predicted and actual steady-state values. Fig. 18a shows how the peak magnitude varies as a function of *n* according to the model and experimental results. There is a final error of 500Ω (20%). For the frequency plot given in Fig. 18b, there is an error of 50kHz (5%). Thus, while the limiting value of impedance magnitude shows some error, the frequency at which it occurs can be predicted quite closely. In our design procedure, this frequency is critical because it is used to help determine the parameter values of Table I. However, the magnitude is not as important. Thus, the utility of the model is verified once again in terms of its ability to predict the limiting system behavior as a function of *n*.

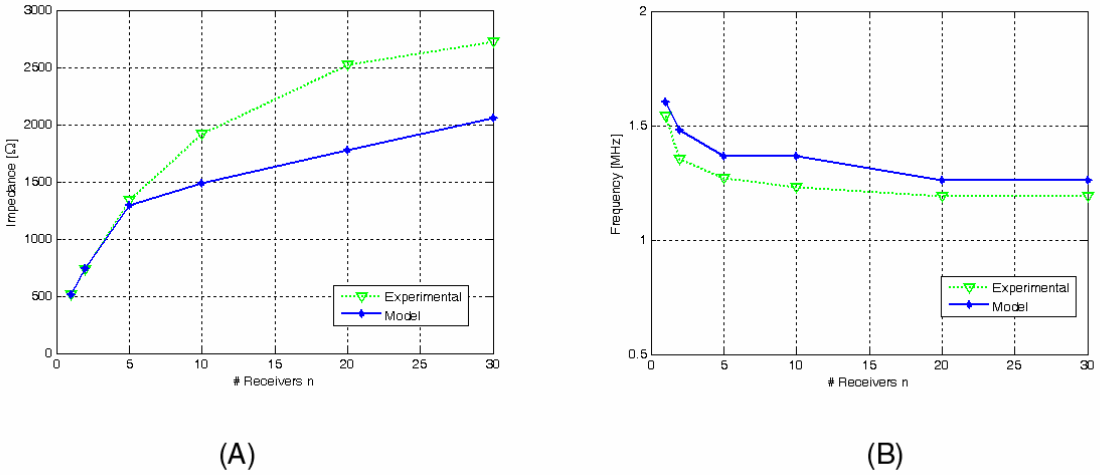

(A) (B)

Fig. 18 Peak magnitude and frequency

4.Electromagnetism in Conductive Fabrics

As mentioned, there are many advantages of using conductive fabrics in wearable monitoring devices. The most obvious is their ability to minimize the burden on the user due to the fact that they feel, behave, and act like fabrics that we are accustomed to wearing on our bodies. This advantage does unfortunately come at a cost. Unlike normal metal cables, conductive fabrics have unpredictable electrical characteristics. While conductive fabrics have been studied for certain applications [8],[13],[14], there is no comprehensive resource that details their electrical behavior. We require information that will give design guidelines for our DC PLC system. Can we utilize the same DC PLC design and treat the conductive fabric as a lumped parameter resistance? Do we have to consider transient effects? How do the probe size and garment geometry affect transmission? To understand how to answer such questions, our first task is to gain some insight into the electrical behavior of conductive fabric sheets.

4.1. Electromagnetic Waves on Conductive Fabrics

We must first evaluate the electrical the properties of the conductive fabric medium in order to understand the potential challenges of designing such a system. Electrically conductive fabrics are readily available from a number of vendors, and with a large range of properties [35],[36],[37]. Cotton, nylon, and polyester are commonly coated or woven with silver, carbon, or nickel. Such fabrics are typically used for shielding the user from electrical shock [38]. However, more recently, they have been used as conductors on printed circuit boards. Within the last decade, they have become more pervasive for use in a variety of conducting configurations, such as transmission lines, sensor arrays, and sensor suits [39],[40],[41]. To this point, various studies on conductive fabric properties have been performed. For instance, Wilson [42] and Crown et. al. [43] have looked at the effects of the conductive fabric microstructure on its properties. Copeland et. al. [44] have looked at radiation effects of garments made of conductive fabrics. Azoulay [14] has looked at the effect of isotropy in conductive fabrics and their effects on certain surface properties. However, for a number of reasons none of the analyses in these references can be generalized for the analysis of our system, dealing with issues, configurations, or test specimens that are geometrically dissimilar to our actual system. The experiments performed utilize certain configurations that are geometrically dissimilar to our actual system.

For this reason, utilize fundamental electromagnetic principles by consulting Maxwell's equations.

We note the layout of our garment consists of conductive fabric 'sheets' with sensor nodes embedded at various points (See Fig. 19).

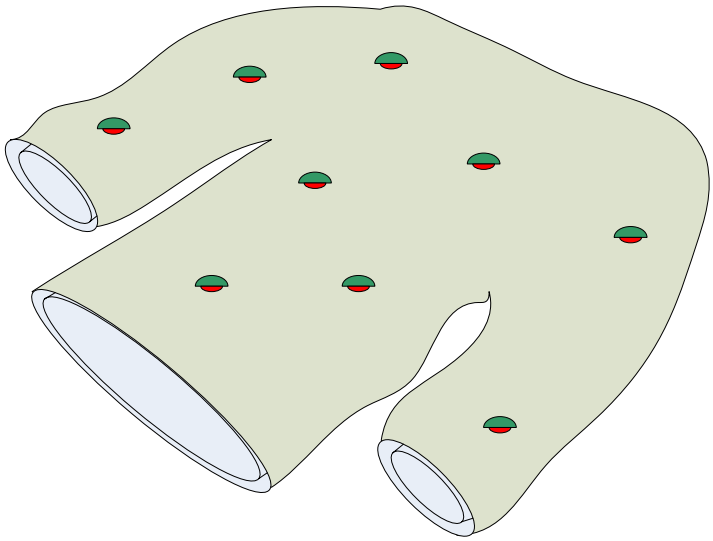

Fig. 19 Conductive fabric garment with sensor nodes embedded at various points

The garment is a distributed system; it is non-centralized, with numerous components physically placed at different locations. There are numerous transmission paths between any two points of transmission. The sensor nodes picture in Fig. 19, all shown on top of the garment are coplanar, inasmuch as the garment itself is coplanar. Finally, we note that, due to the very thin nature of the fabric garment, a significant portion of the transmission should be along the surface of the garment, and not through the cross-sectional area.

These reasons make straightforward application of Ohm's law difficult. Ohm's law, stated simply means that the voltage across a transmission medium is proportional to the current according the proportionality constant, resistance.

$$V = IR \tag{16}$$

This simplified form implies a conductor of constant cross sectional area with uniform conductivity σ in $[\Omega m]^{-1}$ (or alternatively, uniform resistivity ρ in $[\Omega m]$). For our problem, due to the 2D nature of the conductor, the distributed garment nature, and its thin geometry, it does not make sense to apply (16) directly. Further, we are unsure of the material makeup, and unsure of whether or not it has uniform conductivity.

We can evaluate how electromagnetic fields behave in our conductor by considering the electrical dipole (See Fig. 20). In an infinite conductor, the electric field (E-field) lines between a point of reception (marked with a '–', corresponding to a negative charge) and a point of transmission (marked with a '+,' corresponding to a positive charge), emanate radially to and from the points, respectively. At a given point in the garment, the electric field has *x*- and *y*-components defined as;

$$\mathbf{E}_x = -\frac{q}{4\pi\varepsilon}\left[\frac{x+a/2}{\left(\left(x+a/2\right)^2+y^2\right)^{3/2}}+\frac{x-a/2}{\left(\left(x-a/2\right)^2+y^2\right)^{3/2}}\right] \tag{17}$$

$$\mathbf{E}_y = -\frac{q}{4\pi\varepsilon}\left[\frac{y}{\left(\left(x+a/2\right)^2+y^2\right)^{3/2}}-\frac{y}{\left(\left(x-a/2\right)^2+y^2\right)^{3/2}}\right] \tag{18}$$

where q is the charge in Coulombs (C) and ε is the permittivity in [C^2/Jm]. It can be shown that these E-field lines form circular arcs, and that the orthogonal equipotential lines are also circular.

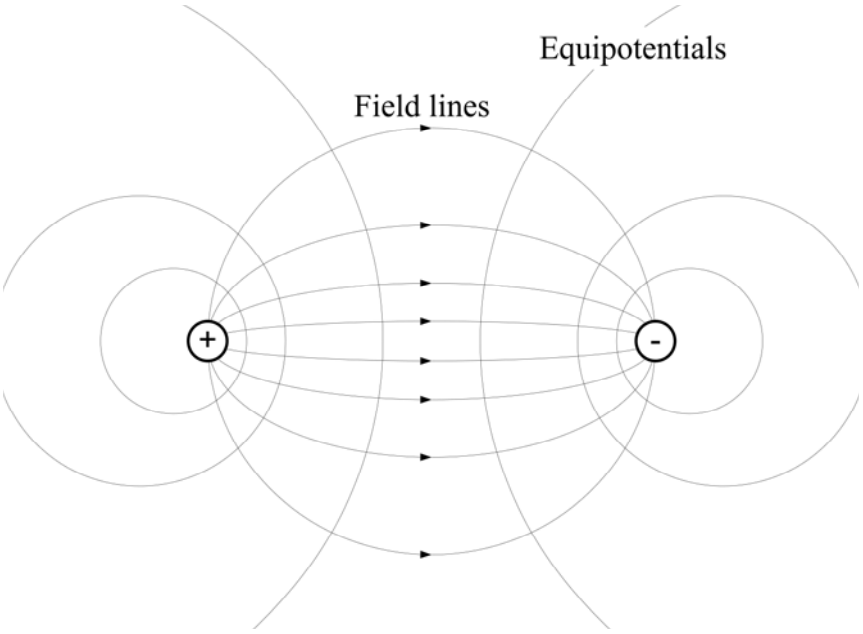

Fig. 20 Field lines and equipotentials due to an electric dipole

Thus, without boundaries, we assume that the larger an area you have, the more E-field lines, the more current paths, and the lower the resistance. In reality, of course, we must account for the boundaries of the conductive fabric pieces, or 'strips.' In a non-infinite strip, E-field lines must conform to the edges. In standard, metallic conductors, Maxwell's equations can be used to determine these boundary conditions and E-field behaviors. We must first determine to what extent such analysis techniques can be applied to our non-standard conductive fabric transmission medium.

4.2. 2D Behavior

If the conductive fabric has homogeneous electrical properties, then electric properties of the fabric media can be completely described by Maxwell's equations. However, 3D Maxwell equations applied to the 3D garment do not provide a closed-form solution. Matching boundary conditions along the 3D garment requires numerical analysis techniques. However, a simplified 2D problem is solvable using Maxwell. We can then use this 2D analysis combined with empirical results from our garment to formulate a closed-form equation for the 3D garment. We assume that certain hypotheses hold. Specifically, we hypothesize that:

- the conductive fabric, which is an aggregate of silver and nylon, behaves like a homogeneous conductor
- the 3D garment resistance behavior can be approximated to an assembly of segments having the 2D and 1D resistance characteristics. Combining these gives a closed-form solution that approximates the 3D resistance.

Performing an electrostatic analysis of the conductive fabric will allow us to verify these hypotheses. We will first analyze the behavior of an ideal, homogeneous sheet of material with uniform electric properties using Maxwell's equations. Next, we will compare the behavior of this idealized material to the resistance measurements taken from a conductive fabric sheet to check the homogeneity condition. This will also allow us to confirm that the 2D resistivity is non-linear, and smaller in magnitude than the 1D resistivity. We will compare the 2D behavior to that of a single strand of conductive fabric (to compare the 2D and 1D transmission properties). To verify the final hypothesis, we will return to the measurements taken on the actual garment.

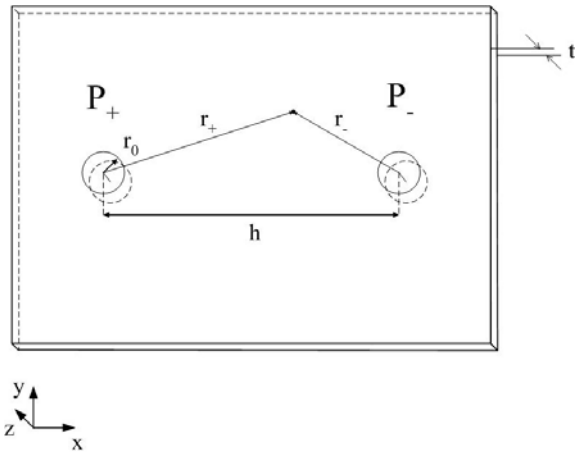

Fig. 21 Conductive Sheet used for Electrostatic Modeling

4.2.1. Electrostatic Analysis

We begin with an analysis of a 2D sheet. We assume that the sheet is infinite in the *x*- and *y*-directions to avoid edge-effect dominated behavior (see Fig. 21). We also assume that the thickness *t* in the z-direction is substantially small so that we can neglect E-field variation in the *z*-direction. Next, we assume that the electrical connection at the transmission and reception points is circular with radius r_0. The implication is that the E-field will emit radially from the transmission point, P_+, and to the reception point, P_-.

With a voltage applied to our sheet at P_+ and P_- and with r_0 small, we have two equal and opposite line potentials of radius r_0 and thickness t, separated by the distance *h*. We apply Maxwell's equations, which can be found in a standard textbook such as Herman A. Haus'[45]]. The potential Φ due to these line charges at a point within the conductor can be found by applying Laplace's equation, which follows directly from Maxwell for static analyses;

$$\Phi\left(r_+, r_-\right) = \frac{\lambda}{2\pi\varepsilon} \ln\left[\frac{r_-}{r_+}\right] \tag{19}$$

where λ is the charge per unit thickness *t*, r_+ and r_- are the distances from each line charge, and ε is the material permittivity (see Fig. 21).

To account for the fact that actual transmission probes have some finite radius r_0, a correction factor must be introduced to the relationship in (19). Furthermore, converting r_+ and r_- to Cartesian coordinates allows us to find the potential as a function of the separation distance *h* and

the disc radius r_0 (for a detailed derivation, see [45]). We can subsequently find the voltage difference between P_+ and P_- by subtracting their respective potentials, $\Phi_+(h,r_0)$ and $\Phi_-(h,r_0)$;

$$\Delta\Phi(h,r_0) = \Phi_+(h,r_0) - \Phi_-(h,r_0) = \frac{\lambda}{\pi\varepsilon}\ln\left[\frac{h}{2r_0} + \sqrt{\left(\frac{h}{2r_0}\right)^2 - 1}\right] \tag{20}$$

We can combine (20) with Ohm's Law, which states that the voltage divided by the current is equal to the resistance;

$$R(h,r_0) = \frac{\Delta\Phi}{I_p} = \frac{\lambda}{I_p\pi\varepsilon}\ln\left[\frac{h}{2r_0} + \sqrt{\left(\frac{h}{2r_0}\right)^2 - 1}\right] \tag{21}$$

where I_p is the current passing from one probe to the next. Thus, for 2D transmission, the resistance increases logarithmically with separation distance h. Also, we note the constant term on the right-hand side of (21);

$$k_{2D} = \frac{\lambda}{I_p\pi\varepsilon_r} \tag{22}$$

This term, which has units of [Ohms], accounts for the material properties of the medium, as well as the behavior of the current. Specifically, the term λ/I is inversely proportional to the drift velocity of the electrons. The drift velocity is proportional to an electron flow rate. Thus, as the electron flow rate increases, k_{2D} decreases, and the resistance decreases, as expected. The permittivity accounts for the material behavior, and as expected, is inversely proportional to the resistance.

4.2.2. Verification of Homogeneity

Now that we have formulated a model for the resistance relationship for a flat homogeneous sheet, we can compare the results to a rectangular conductive fabric section. If they match, then we can model the conductive fabric as homogeneous. A comparator-based milli-Ohm meter was again used to measure resistance at varying distances for a conductive fabric sheet with dimensions 90cm×140cm. The results are shown in Fig. 22, plotted on a log-scale along with the model of (21). Excellent agreement can be found between the model for the homogeneous media and the experimental data.

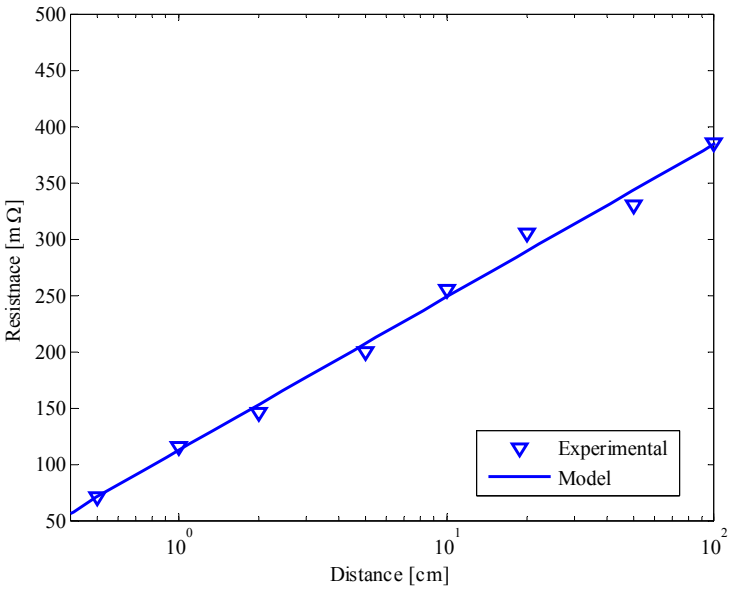

Fig. 22 Measured Resistance and Model Resistance for Sheet

This result verifies that the conductive fabric can be treated as a homogeneous material with uniform properties.

4.3. Ohmic conduction

To confine the problem, we now consider the effects of using a non-infinite sheet, or a strip of conductive fabric, pictured in Fig. 23. Having verified the electrical homogeneity of the conductive fabric, we can apply Maxwell's equations to the strip. Specifically, we consider the electro-quasistatic approximation, and assume that Ohmic conduction governs the E-field behavior.

Fig. 23 Strip of conductive fabric with a point of transmission and a point of reception

In treating this as an Ohmic conduction problem, we know that the e-field lines in the material are governed by the Laplace equation;

$$\nabla^2 \Phi = 0 \tag{23}$$

Because we consider a sheet, which is extremely thin (relative to it's length and width), we neglect e-field variations in the z-direction, and (23) reduces to;

$$\frac{d^2\Phi}{dx^2}+\frac{d^2\Phi}{dy^2}=0 \tag{24}$$

Now, we can solve (24) using the normal and tangent boundary conditions for the strip, and the potential imposed at the transmission and reception points;

$$\left\{\begin{matrix} @\,x=0,l; & \dfrac{d\Phi}{dx}=0 \\ @\,y=0,w; & \dfrac{d\Phi}{dy}=0 \end{matrix}\right\},\left\{\begin{matrix} @\,probe1; & \Phi=V_0 \\ @\,probe2; & \Phi=0 \end{matrix}\right\} \tag{25}$$

The general solutions to this equation are of the form;

$$\Phi=A\left\{\begin{matrix} \sin \\ \cos \\ e^{\pm} \\ -\sin \\ -\cos \end{matrix}\right\}kx\left\{\begin{matrix} \sinh \\ \cosh \\ e^{\pm} \\ -\sinh \\ -\cosh \end{matrix}\right\}ky \tag{26}$$

By superimposing the solutions of the strip with each probe in isolation, we find;

$$\Phi=A\sin(kx)\sinh(ky)+B\cos(kx)\cosh(ky) \tag{27}$$

We can visualize this result through the use of a finite element analysis.

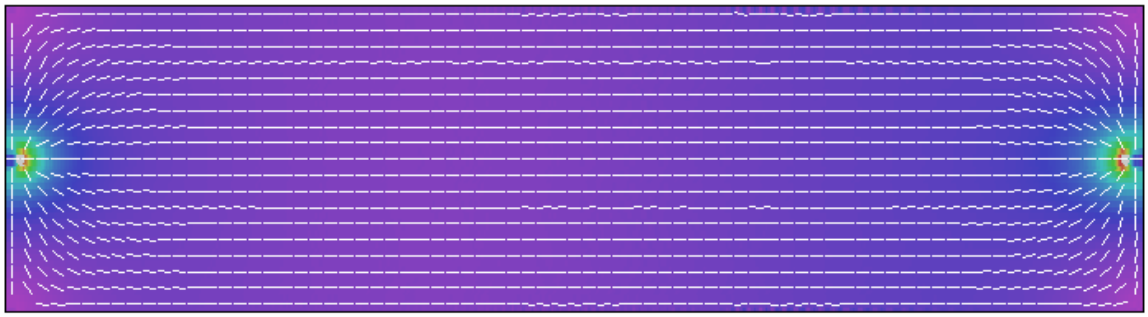

Fig. 24 Finite element representation of field lines in a conductive fabric strip

As we can see, in the vicinity of the probes, the field lines are similar to those depicted in Fig. 20. However, near the edges, we can see the effects of the boundary conditions on the field lines. And in the bulk of the material, at a distance from the probes, the field lines are parallel and linear, as would be expect if the probes were the full width of the strip. The relative size of these regions will, of course, depend on the strip geometry. For a square section, the linear region is much less pronounced, and the ideal field line behavior is more prevalent (See Fig. 25).

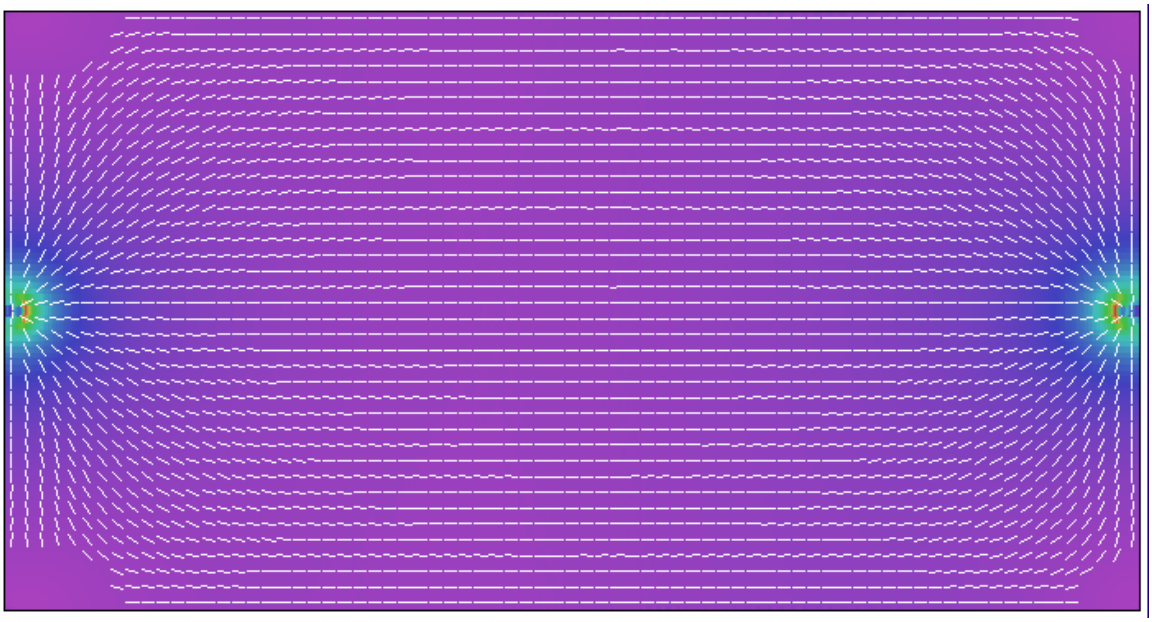

Fig. 25 Finite element representation of field lines in a square conductive fabric strip.

4.4. Experimental Design – Applying DC PLC to a wearable system

To apply the DC PLC scheme described in Section 3, we will have to make modifications to our current design procedure. Physically, the conductive fabric medium replaces the CPS line of Fig. 12 (as depicted in Fig. 26). Practically speaking, there are a number of issues that must be taken into account. Whereas the system described in Section 3 was implemented using circuit boards and bench-top power cables, we must now determine a mechanism for fastening the various components to this fabric transmission medium. However, of more importance is determining how the design procedure might change. That is, how will the electrical properties of the transmission medium affect the procedure described in Section 3.2? Will resonances be created between the medium and the transmission line transformer? Will we be able to transmit DC power over the medium? To answer these questions, some experimental tests can be useful. However, of premier importance is a fundamental understanding of how the governing physics will affect DC and AC electrical behavior in the conductive fabric garment. These issues will be addressed in the following two chapters.

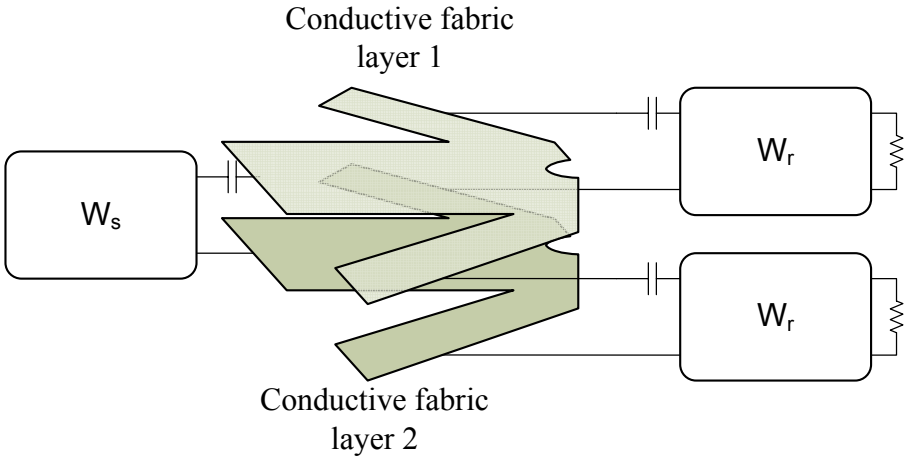

Fig. 26 The conductive fabric garment as a replacement for the CPS line of Fig. 12

5.DC Analysis of Conductive Fabrics

For the design of the DC-PLC system, and to describe the results of the initial experiments, we need to be able to predict the DC resistance between any two points in the garment. The design of the modem and the DC-PLC system depends on the resistances between the master node and any given sensor. Specifically, for successful operation of our system, we must be sure that there is no interference between our DC power transmission and the AC data transmission.

5.1. 1D and 2D Conductivity

We now compare the 1D and 2D conductivity results. Note that, for a homogeneous conductor of constant cross section A and length h, the resistance is;

$$R = \frac{\rho h}{A} \tag{28}$$

This 1D relationship is used for most resistors, and will be used here for our strand of thread. We were able to find that the resistance per length of the silver coated nylon thread was 800Ω/cm, we can plot the linear conductivity of a single thread versus the conductivity predicted by our sheet model (Fig. 27).

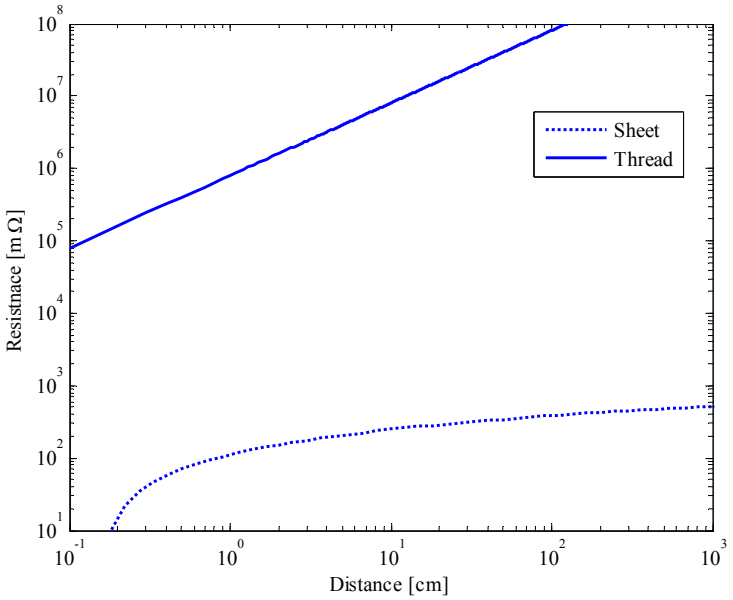

Fig. 27 Resistance of Sheet and Thread vs. Length

As expected, the savings are dramatic. In the plot, we see that even at 1m (100cm) (the length scale of the human body) the resistance in a sheet is less than 0.4Ω, whereas the thread resistance is 80kΩ. Indeed, our early resistance experiments (with results depicted in Fig. 33) affirm the fact that the garment conductivity is comparable to 2D transmission rather than 1D transmission. These results verify the utility and advantage of using conductive fabric sheets as a transmission medium.

5.2. Deriving the Closed-Form 3D Solution

We have derived a closed-form relationship for determining resistance as a function of length for a sheet. Based on this analytic result, we now obtain the resistance of a 3D garment. Unlike the more tractable 2D analysis, Maxwell's equations cannot produce a closed-form solution for the 3D garment resistance. Thus, we need another means of deriving a relationship that describes the 3D behavior. To do so, we first take note of the garment geometry. The shirt and pants that we traditionally wear can be simplified into a set of connected cylinders (See Fig. 28A). That is, the part of a shirt surrounding the trunk is primarily cylindrical in nature. The same is true for the shirt sleeves and the pant legs. Therefore, the resistance of the 3D garment may be obtained by analyzing the resistance of individual cylinders and assembling the component resistances together.

5.2.1. Cylindrical Reduction

Each cylinder differs in length L and diameter D, and the resistance characteristics vary depending on these dimensions. As the diameter gets larger, the E-field created by a pair of electrodes becomes similar to that of the 2D infinite sheet. "Un-wrapping" a cylinder with a large diameter creates the 2D sheet that was analyzed in the previous section (See Fig. 28B). Therefore, for large-diameter cylinders, the previous closed-form resistance model will give a close approximation. On the other hand, as the diameter becomes smaller and the length gets longer, the resultant resistance characteristics get closer to a single strand 1D conductor. Namely, the resistance will increase linearly with the length of the cylinder. We hypothesize that an arbitrary cylinder exhibits a mixture of the two types of resistance characteristics.

We will derive an approximate 3D closed-form solution that resembles the 2D solution of **(21)** with additional terms to account for the cylinder geometry. By empirically determining the behavior of these cylinders, we can determine what modifications must be made to (21) to

accurately predict the DC resistance. Our simplification of the garment into cylinders is the 'bridge' between the tractable 2D model and the actual 3D garment.

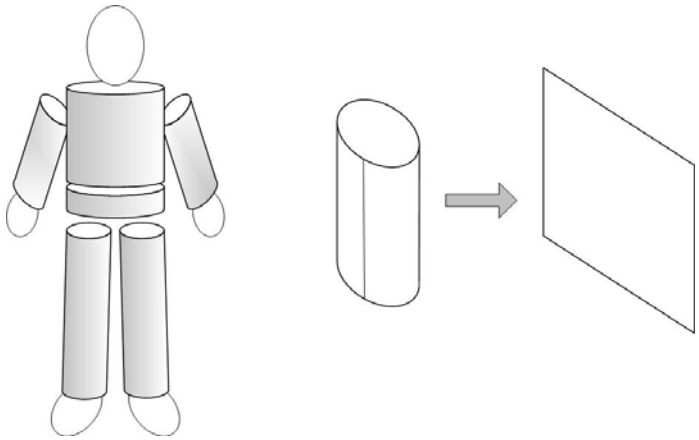

Fig. 28 Garment Simplified as Cylindrical Sections and Cylindrical Section Being 'Unwrapped'

5.2.2. Resistivity of Cylinders

To experimentally determine the resistivity of the cylinder, the resistance of cylinders of varying diameters is measured according to the method depicted in Fig. 29. With one probe placed 10cm from the edge of the cylindrical conductor, the resistance is measured at 5cm intervals along the length of the cylinder. Fig. 30 shows the measured resistance in [milli-Ω] for three different diameters. Note that the resistance curve for the smallest diameter, D = 9 cm, is almost a straight line, resembling the linear resistance curve of 1D conductor. As the diameter becomes larger (e.g. for D = 18), the resistance curve becomes closer to that of a logarithmic function, similar to that of the 2D infinite plane.

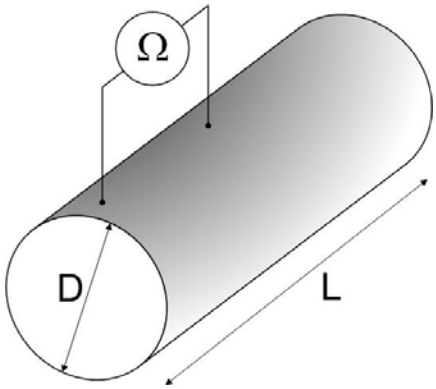

Fig. 29 Measurement Method for Cylindrical Sections

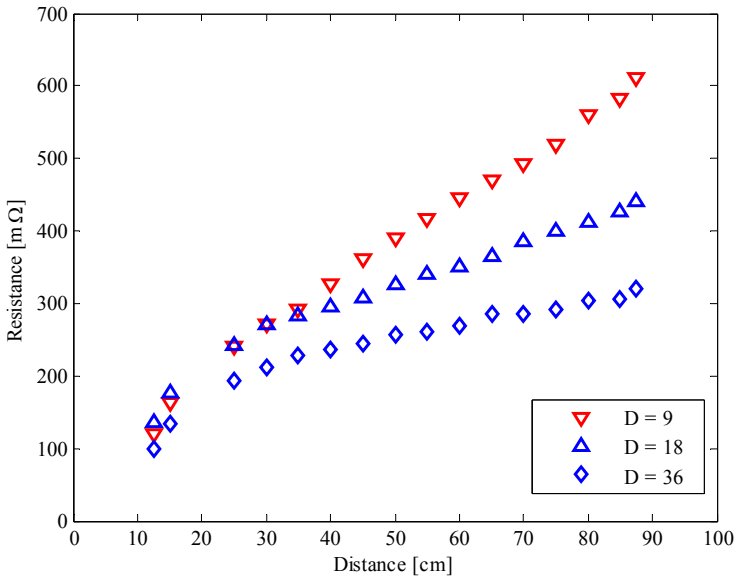

Fig. 30 Plot of Resistance vs. Distance for Cylinders of Diameter 9, 18, and 36cm

5.3. 3D Prediction Method

Based on the observations of the previous section, we consider the following function relating the cylinder dimensions to the resistance:

$$R(x) = p_1 \times \log\left(\frac{h}{r_0}\right) + p_2 + p_3 \times (h) \tag{29}$$

where p_1, p_2, and p_3 are parameters to be determined, and r_0 is the probe diameter. This expression incorporates both the 1D and 2D behavior; thus, we call it the 1D-2D model. The first two terms represent the 2D resistance characteristics, which are dominant when D is large (See (21)). The third term represents the 1D resistance characteristic, which is dominant as the diameter gets smaller.

The p_i coefficients are found to be functions of the cylinder geometry. By taking data from a variety of cylinders, we find that p_1, p_2 and p_3 relate to the D/L ratio according to (30):

$$p_1 = k_{2D}\left(-265.36\left(\frac{D}{L}\right)^2 + 206.27\left(\frac{D}{L}\right) + 6.76\right)$$
$$p_2 = k_{2D}\left(-914.42\left(\frac{D}{L}\right)^2 + 325.07\left(\frac{D}{L}\right) + 69.79\right) \quad (30)$$
$$p_3 = \frac{\rho_{sq} L}{\pi D}\left(0.0091\left(\frac{L}{D}\right)^2 + 0.75\left(\frac{L}{D}\right) - 0.39\right)$$

Note that the p_3 term has a different leading constant. This constant is a function of the sheet resistance, ρ_{sq}, which has units of [Ω/square] (see description of the sheet resistance term in Appendix 10.1). Note that this is a unique parameter, used commonly in printed circuit board design. When flat conductors, such as traces on a printed circuit board, are used, often the resistance for a unit square of material is calculated. To calculate the resistance of a trace, the number of squares in sequence is added together, and the total resistance is just the number of squares multiplied by the sheet resistance. Unlike normal 1D transmission, such as through a wire, the current primarily passes along the surface of the conductor. Thus, we cannot use the typical resistance relationship of (28) and must account for this by using the augmented leading term on p_3. We then cross-validated the 2D-1D model using cylinders of varying diameters. The close agreement between our model and the experimental results indicated in Fig. 31 supports the validity of the 2D-1D model of (29) and (30).

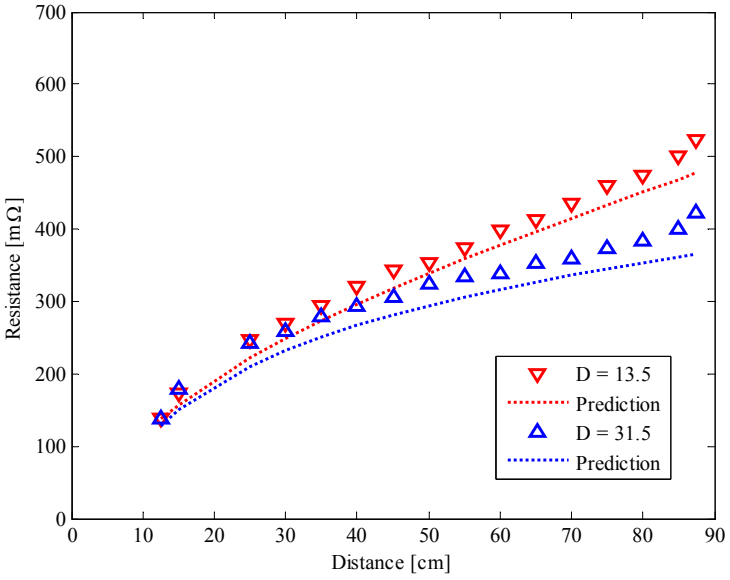

Fig. 31 Plot of Resistance vs. Distance for a Cylinders of Diameter 9, 18, and 36cm

So far, we have not yet considered the edge-effect. That is, when a probe is close to an edge, we must account for the fact that there is a current build-up, and less paths of electrical conduction between the two points. As a result, electric-field lines, along which current flows, will be 'cutoff' at the edges, effectively reducing the number of current paths between two points and increasing the resistance This is the reason for the deviation between the experimental results and the logarithmic fit evident in Fig. 31 above x = 80cm, where the distance to the edge on the far-end is less than 10cm. If we assume that we are not operating close to an edge, this can be neglected.

Note also that the experimental resistance values are higher than the values of our prediction method. This is due to the fact that our prediction method is based on an infinite sheet model. In the real world, due to the edge effect, there are less paths of conduction between the probes. Thus, there are effectively less paths in parallel, and the effective resistance is higher. In our DC-PLC system, it is vital to be able to limit the resistance between the master node and the sensor nodes. While finite element analysis can be used to get specific resistances, we have formulated an accurate, generalized analytical solution that allows us to design these garments for bodies of various sizes, shapes, and dimensions and gain physical intuition into the electrostatic behavior of such garments. The value of this method is demonstrated in the following section, where we predict the DC resistance values depicted on the garment. Our analysis method is as follows; first we represent the trunk and arms as simplified cylindrical sections. Next, we use the distance h between the two measurement points to predict the resistance. Since the geometry varies between remote points (e.g. a point on the wrist and a point on the trunk), we can find a resistance value for each section, and add them in series (see Fig. 32).

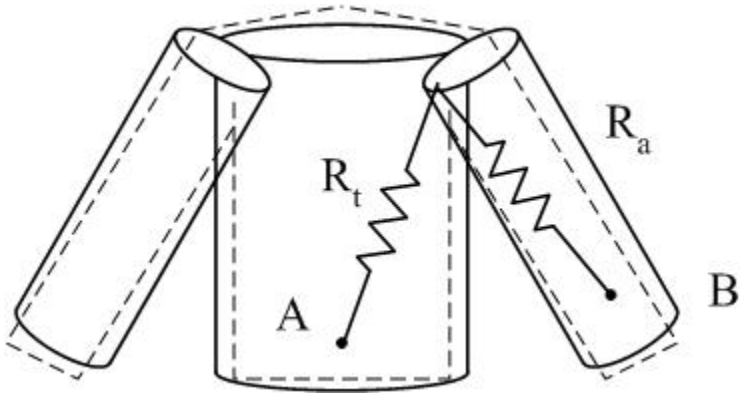

Fig. 32 Equivalent Resistance Diagram for Garment

Using (30), we calculate a few selected resistance values and compare with those that were determined empirically. For the arm section, the *D/L* ratio is 0.17. For the trunk, the *D/L* ratio is 0.5. The trunk resistance is denoted R_t and the arm resistance denoted Ra. Thus, the total resistance between points *A* and *B* is $R_t + R_a$. The distance between the master node and the shoulder, h_t, is 80cm. The distance between the shoulder and the wrist, h_a, is 60cm. These values are used to create the results shown in Fig. 33, with empirical results in bold and predicted values in parenthesis.

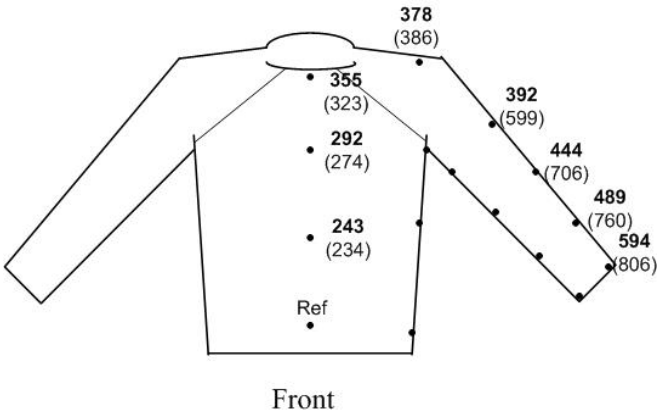

Fig. 33 Comparison of empirical and predicted resistance values in [mΩ]

Our method provides an accurate estimate for predicting the resistance between points on the trunk, with a maximum error of 9.01%. However, predictions for the arm are much higher than the measured values. In our analysis, we do not account for the connection at the shoulder. In calculating the resistance values for points on the arm, h_t and h_a are too large and cause our predicted values to be consistently larger than the experimental values.

Our cylindrical section approximation breaks down at the shoulder. We turn to finite-element analysis methods to account for and predict this behavior. The software allows us to 'break' the garment into distinct sections, as shown in Fig. 34.

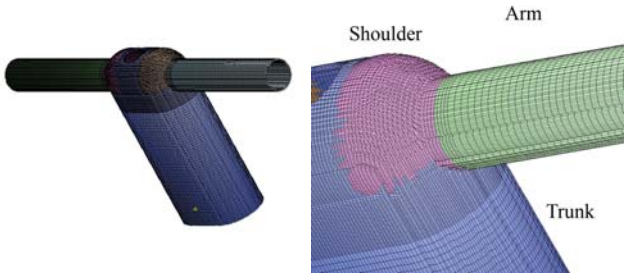

Fig. 34 Finite element construction of the garment and close-up view of the shoulder section

We investigated anthropometric data to find the 'typical' body dimensions of a user [46]. We constructed a number of garments with dimensions fitting 98% of the population. Evaluating the power dissipated in the shoulder when a voltage is placed across the garment allows us to calculate the resistive contribution of the shoulder. For our 25 trials, the predicted resistance was 77mΩ with a deviation of 12mΩ. Thus, for varying geometries, the resistive contribution of the shoulder does not vary significantly.

By using this fixed value shoulder resistance, R_s, we now augment our prediction method as depicted in Fig. 35. Whereas the length between the trunk and arm point was previously found by measuring the distance to a single point on the shoulder, we now measure from the trunk point to the shoulder section's edge and from the shoulder section's opposite edge to the arm point.

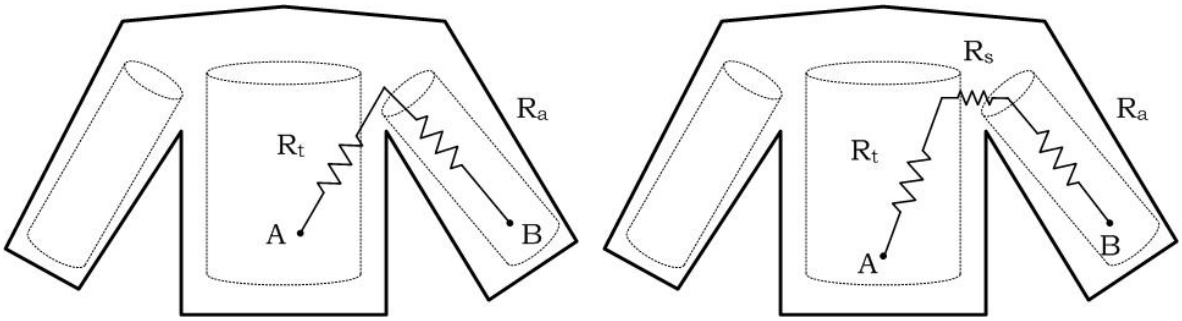

Fig. 35 Old and new prediction methods for resistance values along the arms

To calculate the resistance, we now write;

$$R(x) = R_t(h_t) + R_s + R_a(h_a) \tag{31}$$

with results shown in Fig. 36.

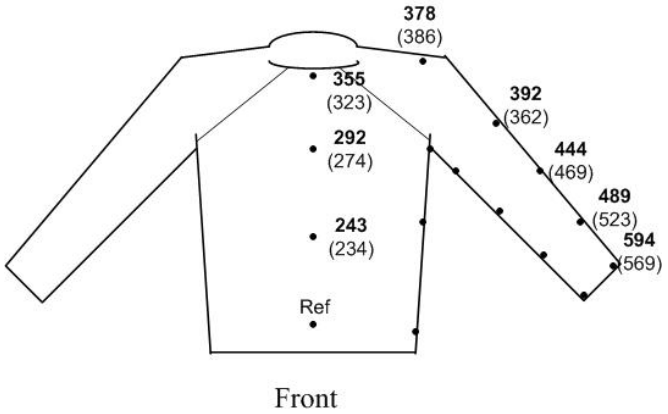

Fig. 36 Results of revised prediction method

We expect a one-to-one relationship between the experimental results and the results of our prediction method. Fig. 37 demonstrates how well the revised prediction method works.

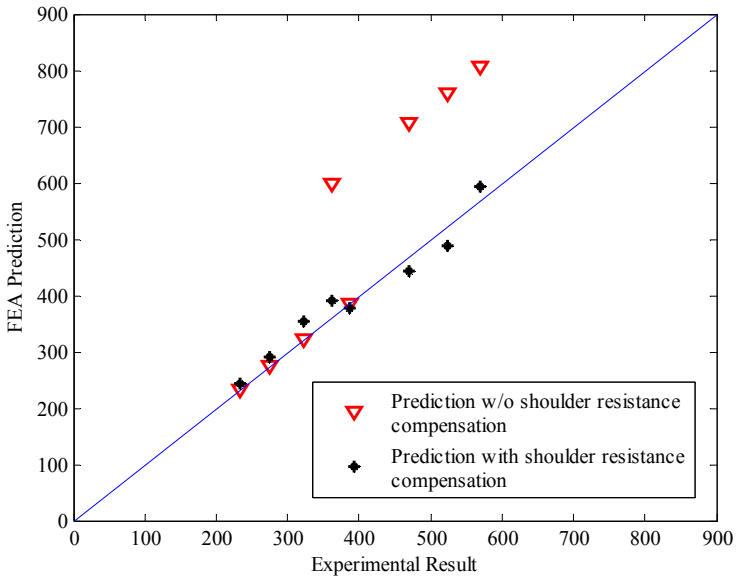

Fig. 37 Comparison of the original prediction method and the revised prediction method which accounts for shoulder geometry

With minimal use of time-consuming numerical analysis techniques, we have found a method of estimating DC resistance for a garment, given only its geometry. This gives useful insights and design guidelines.

6.AC Analysis of Conductive Fabric

Our goal is to develop a garment for remote wearable health monitoring that utilizes conductive fabric sheets for data transmission. In order for multiple nodes to simultaneously and reliably transmit data, we must understand the garment's channel properties. Specifically, the bandwidth and gain, time delay, and noise must all meet certain requirements. These are all dependent on the garment material, the garment geometry, and the load impedances. Here, we discuss the relevant design challenges that motivate our AC analysis, and our resulting approach to developing a wearable network for data transmission.

As we did with the DC analysis, we will start by analyzing geometrically simple sections of conductive fabric to ensure the accuracy of models and testing procedures. We will then characterize the conductive fabric garment impedance and bandwidth. Finally, we will construct a transmission line model of the conductive fabric in order to explain its frequency dependent characteristics.

6.1. Design Challenges

The preceding phenomena are determined by the garment shape, garment size, and conductive fabric material, and may pose challenges to successful data transmission on the garment. These challenges are described in the following.

6.1.1. Bandwidth and Gain

We must consider the garment bandwidth and gain, which determine 'how much' signal can be transmitted and at what frequencies. Our goal is to maximize the number of successful simultaneous transmissions from the sensor nodes in the system. The bandwidth places a limit on these transmissions, since it is a specification of the usable frequency band. Physically, the bandwidth is governed by the construction of the system, including transmission line material properties, physical shape, and the loads connected across the power / data bus.

If the signal amplitude is not sufficiently large within this frequency range, it can become impossible to observe the modulated sensor node output. We will thus characterize bandwidth as the frequency ranges over which the gain is equal to or greater than a specified value.

6.1.2. Transient Behavior

Because our conductive fabric garment is a distributed, 2D transmission medium, we must consider transient effects. Transient effects such as time delays can result in bit errors for the transmitted data. Bit transitions (from high-to-low or low-to-high) can be prone to error because the threshold set for measuring bits may not be reached in the expected amount of time. Depending on the medium size, transients can also result in standing waves, which create anti-nodes at which the signal amplitude will be zero. The transient effects depend on the garment's distributed nature, the distance between a sender and a receiver, and the loads connected to the garment.

The most significant cause of delays is the distributed capacitive nature of the garment (See Fig. 38). As a signal propagates along a medium with distributed capacitance, each subsequent capacitor must be charged with voltage. The time associated with this charging is the delay. The delay will also be determined by line length and the velocity of signal propagation, which is a function of the dielectric constant ε of the insulator. We must place a limit on the maximum expected delay in the system.

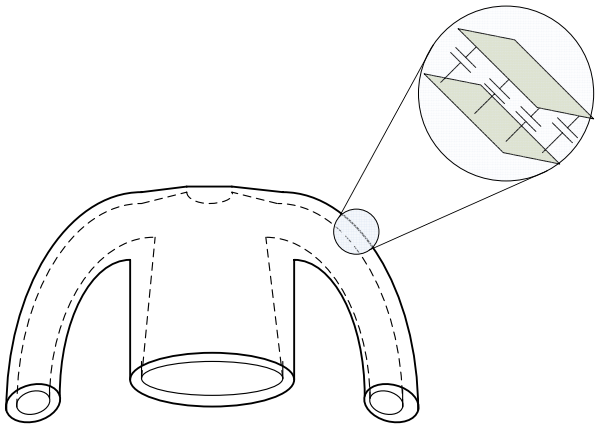

Fig. 38 Distributed capacitance of parallel conductors

6.1.3. Noise and interference

We will also consider noise sources in the system in order to ensure that we can successfully decode transmitted data. Once we determine noise sources, we must minimize their effects on signals transmitted in the system. The noise can be caused by both external and internal sources. Externally, there are numerous sources of radiated electromagnetic noise such as the 60Hz 'hum' caused by electronic appliances. We must ensure that the garment does not behave as an antenna

by picking up this undesirable noise. Additive noise can also be generated by 'internal' components such as solid state devices and power converters. Furthermore, interference from other sensors in the system can manifest itself as signal noise. When using frequency modulation techniques, we assign a certain frequency band to each sensor node. There is a minimum required value for the separation between subsequent frequency bands in order to avoid interference noise.

The metric for evaluating these adverse effects is the Signal-to-Noise Ratio (SNR), which is simply the ratio of signal amplitude to noise amplitude. Of course, depending on the sensitivity of the data to errors, and the importance of the data, the SNR requirement can be tightened or loosened. Upon determining an allowable SNR, if we find that the system's SNR is restrictively high, proper shielding of the transmission medium and designing of the filters within the modems can help us to reduce adverse effects of noise.

6.2. Initial tests and experimentation

Even though our system is a localized, isolated network, there are still environmental phenomena which can make data transmission difficult. To determine which of these effects are relevant, we can attempt to transmit data and observe what, if any, problems occur.

6.2.1. Bandwidth

To measure the garment bandwidth, we transmitted a signal at the lower trunk, where the central control unit will be placed, and looked at the received signal at other points on the garment (See Fig. 39).

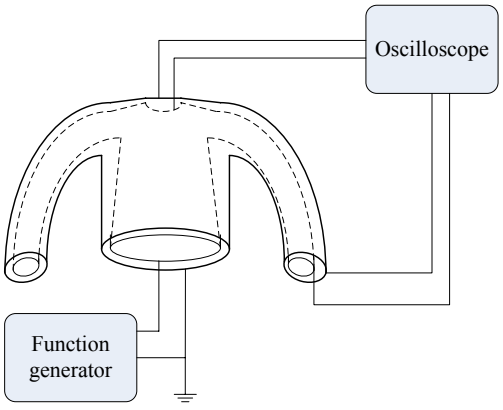

Fig. 39 Garment transmission and measurement points

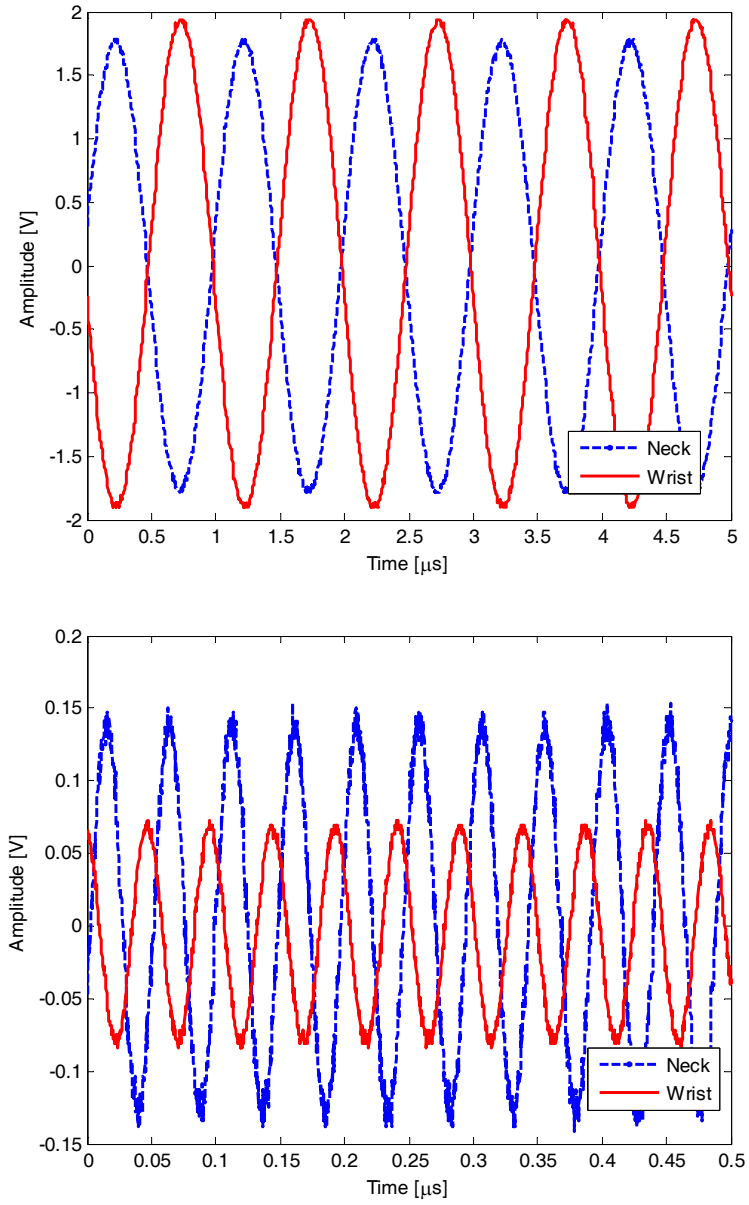

Fig. 40 Signal amplitudes at 1MHz and 20.6MHz taken at the neck and wrist

By varying the signal frequency, we found the frequency band over which transmission is possible. For the purposes of brevity, we present data from two specific transmission frequencies. There is a noticeable difference in signal gain that is both frequency and location-dependent. When transmitting a 1MHz signal, the received signal amplitudes at the neck and wrist are the same (see Fig. 40a). However, a 20.6MHz signal produced a significantly different result, with the amplitude at the neck twice that measured at the wrist (Fig. 40 b). This result indicates that amplification will have to be used and that certain frequency bands will have to be avoided for sensors depending on their locations in the garment.

6.2.2. Impedance matching

Finally, we must understand the impedance characteristic of our transmission medium and sensor nodes to make sure that impedance is matched between senders and receivers. To do so, we use an impedance analyzer in the configuration of Fig. 41. Here, we want to find the garment characteristic impedance. While characteristic impedance cannot be measured directly, the short circuit and open circuit impedances can be measured. To do so, we connect the impedance analyzer probes to one arm (the left or right), with each probe connected to the inner or outer layer. Subsequently, we place an open or short across the opposite wrist. Then, using the relationship;

$$Z_0(\omega) = \sqrt{Z_{sc}(\omega) Z_{oc}(\omega)} \tag{32}$$

we can find the characteristic impedance, $Z_0(\omega)$, as a function of the short circuit and open circuit impedances $Z_{sc}(\omega)$ and $Z_{oc}(\omega)$. The gain and phase of the complex impedance, $Z_0(\omega)$, are shown in Fig. 42.

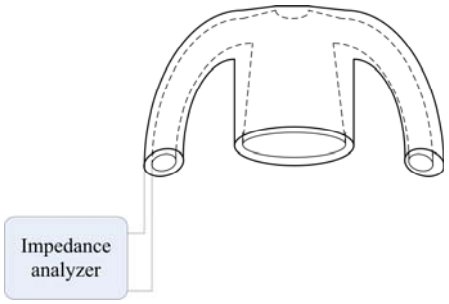

Fig. 41 Impedance analyzer setup for measuring garment impedance

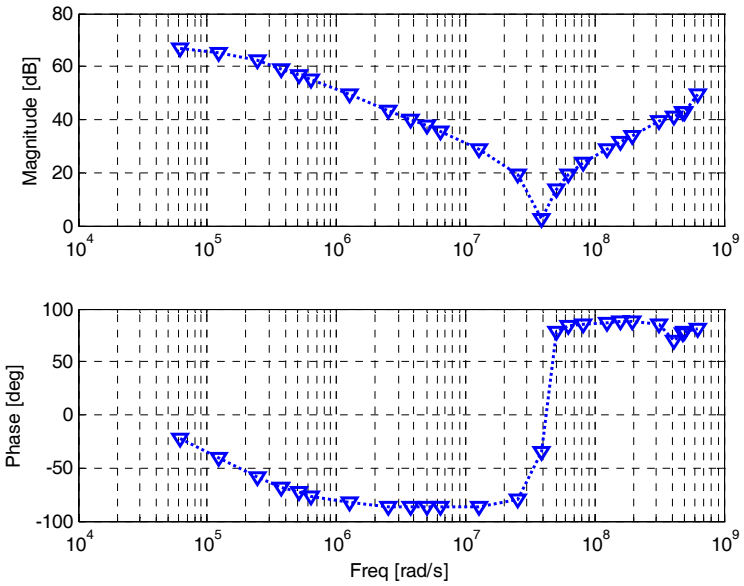

Fig. 42 Gain and phase plots for complex impedance $Z_0(\omega)$ for entire garment

This result is indicative of both capacitive and inductive behavior. That is, for low frequencies, when capacitive impedance dominates, we see decreasing magnitude and a phase of -90^o. However, at 670kHz (4.21Mrad/s), there is a sink in the impedance characteristic, due to internal resonance. The phase jumps to +90^o and the impedance begins to increase. This *L*-*C* behavior could be indicative of transmission line effects. Based on these observed phenomena, we proceed to discuss the types of challenges for the design of this garment.

6.3. Transmission Line Theory

The physical construction of our conductive fabric garment immediately brings to mind the structure of a transmission line. A transmission line is any conductor used for transmitting electrical or optical signals or power. In its more common use, the term transmission line refers to a number (usually 2) of parallel conductors used for the propagation of electrical waves.

There are a number of text books that detail the derivation of transmission-line theory; particularly comprehensive handling of the subject can be found in Kong and Staelin [47], [48]. Here, we introduce the transmission line equations to gain insight into the design of the conductive fabric garment, using the method presented in Kong [47].

We start by considering Maxwell's equations, which describe relationships between the electrical and magnetic fields.

$$\nabla \times \mathbf{H} = \frac{\partial \mathbf{D}}{\partial t} + \mathbf{J} \tag{33}$$

$$\nabla \times \mathbf{E} = -\frac{\partial \mathbf{B}}{\partial t} \tag{34}$$

$$\nabla \cdot \mathbf{D} = \rho \tag{35}$$

$$\nabla \cdot \mathbf{B} = 0 \tag{36}$$

where ***E*** is the electrical field strength [V/m], ***B*** is the magnetic flux density [webers/m^2], ***H*** is the magnetic field strength [A/m], ***D*** is the electric displacement [C/m^2], ***J*** is the electric current density [A/m^2], and ρ is the electric charge density [C/m^3]. Assigning material and geometric constraints allows us to derive closed-form solutions to Maxwell's equations. We take, for example, the case of the parallel plate transmission line, pictured in Fig. 43.

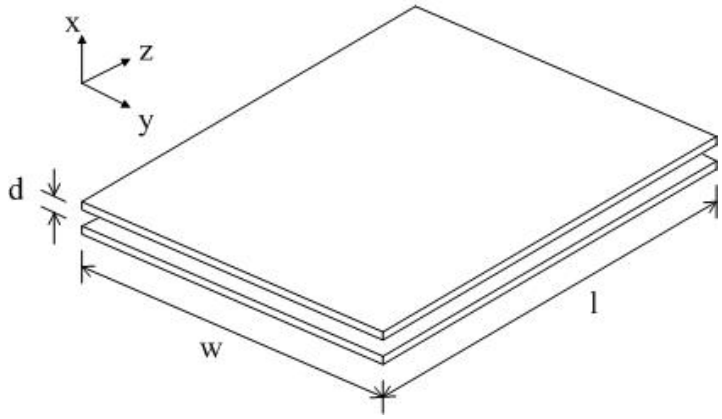

Fig. 43 Parallel-plate transmission line model

Here, we assume that we have two parallel conductors separated by a gap of height *d*, which is filled with a dielectric material of permittivity ε. If we assume that the gap *d* is very small, we can assume that 'all electromagnetic fields are in between the plates and there are no fringing fields outside of the plate regions' [47]. This means that wave is such a transmission line will propagate along the *z*-direction, with the ***E*** and ***H*** fields perpendicular to the direction of travel. This is commonly known as transverse electromagnetic (TEM) wave mode. By confining ***E*** to the *x*-direction, and ***H*** to the *y*-direction, and assuming that continuity holds, Maxwell's equations simplify to expressions in space and time;

$$\begin{aligned} \frac{\partial}{\partial z} E_x(l,t) &= -\mu \frac{\partial}{\partial t} H_y(l,t) \\ \frac{\partial}{\partial z} H_y(l,t) &= -\varepsilon \frac{\partial}{\partial t} E_x(l,t) \end{aligned} \tag{37}$$

(see [35] for derivation). Capacitance and inductance per unit length can be written in terms of the geometry as;

$$L_{ul} = \frac{\mu d}{w}$$
$$C_{ul} = \frac{\varepsilon w}{d} \tag{38}$$

Now, combining (37) and (38) we can write the transmission line equations as;

$$\frac{\partial}{\partial z} V(l,t) = -L_{ul} \frac{\partial}{\partial t} I(l,t)$$
$$\frac{\partial}{\partial z} I(l,t) = -C_{ul} \frac{\partial}{\partial t} V(l,t) \tag{39}$$

The capacitance and inductance per unit length are critical for evaluating transmission line behavior. Unlike typical linear circuit analysis, transmission line theory accounts for time-dependent transients on the line. That is, we must consider the time it takes for a wave to propagate along the line. To do so, we consider the transmission line characteristic impedance, Z_0. Instead of the relationship of (32), we use the more general definition;

$$Z_0 = \sqrt{\frac{L_{ul}}{C_{ul}}} \tag{40}$$

The characteristic impedance is used to determine the behavior of reflections on the transmission line (see Fig. 44).

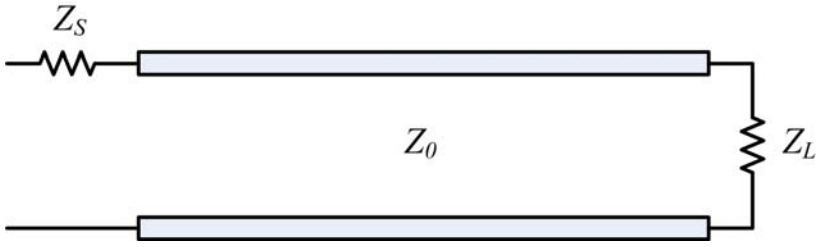

Fig. 44 Transmission line impedances and resistances

According to the figure, we also consider the source impedance, Z_s, and the load resistance, R_L. We can then define the source and load reflection coefficients as;

$$\Gamma_L = \frac{Z_L - Z_0}{Z_L + Z_0}$$
$$\Gamma_S = \frac{Z_S - Z_0}{Z_S + Z_0} \tag{41}$$

Finally, to evaluate the voltage and current at a point z on the transmission line, in lieu of Kirchoff voltage and current laws, we use the transmission line equations to write $V(z)$ and $I(z)$ as;

$$V(l) = V_0\left(e^{-jkl} + \Gamma_L e^{jkl}\right) \tag{42}$$

$$I(l) = \frac{V_0}{Z_0}\left(e^{-jkl} - \Gamma_L e^{jkl}\right) \tag{43}$$

where k is the spatial frequency. The generalized impedance, $V(z)/I(z)$ looking into a transmission line, is then equal to;

$$Z(l) = \frac{V(l)}{I(l)} = Z_0 \frac{e^{-jkl} + \Gamma_L e^{jkl}}{e^{-jkl} - \Gamma_L e^{jkl}} \tag{44}$$

(Note that, by setting Z_L equal to zero and infinity in (41), and evaluating (44), we can obtain Z_{sc} and Z_{oc}, respectively. The impedance, written in such form, can then be used to derive (32)).

6.4. Deriving the TL Model for our Garment

To model our garment, we wish to predict the AC characteristics manifest when data is transmitted on the conductive fabric. As with the DC analysis, this is done by assuming that we can determine the performance of each of the sections in isolation (that is, the trunk and arms) and later introduce components to account for the transition regions between the sections (e.g. at the shoulder). We will first discuss the behavior of individual cylindrical sections, and then determine the aggregate garment behavior.

The model used for the entire garment is depicted in Fig. 45. As with the DC analysis, we separate the arms and trunk into three individual sections. As such, we assume that there is one transmission line for the trunk and one for each arm (See Fig. 45).

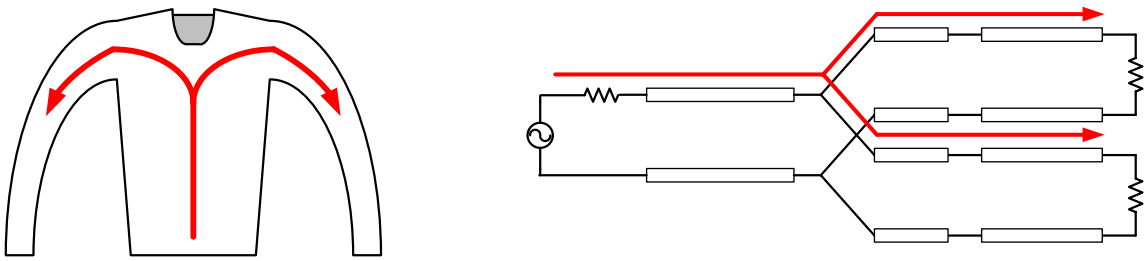

Fig. 45 Transmission line approximation of the conductive fabric garment

As depicted in this figure, a signal is being transmitted from the centralized components. This signal will travel the length of the trunk to the arms, as illustrated by the red arrows in Fig. 45. At the top of the garment, where the arms meet the trunk section, the signal splits (assuming equal impedance for the arms). For this reason, we have the arm transmission lines in parallel. In this case we have added series resistances at the 'arms' and load resistances as well. In fact, when verifying this model with experimental results, we expect to see geometry-dependant effects at the intersection of the arms and trunk. The series impedance can be used to account for such effects. The terminal resistances at the arms are essentially design parameters. We can tune the model (and the actual garment) AC characteristics with a specific terminal impedance or stub if necessary.

We can validate this model by comparing experimental results with our derived analytical model. In this case, we can evaluate the input impedance and gain. Both are easily measured, and insightful for understanding garment bandwidth.

Our procedure is to derive the analytical impedance, experimentally determine the relevant parameters, and finally to compare the analytical and experimental results. To derive the impedance model, we must specify the source voltage, V_s and source resistance R_s, and the load impedances $Z_{L,ai}$ (all of which we can choose in the actual system). The length and characteristic impedance of the trunk transmission line are denoted L_t and $Z_{0,t}$. Similarly, the arms have lengths and characteristic impedances L_a and $Z_{0,a1}$ and $Z_{0,a2}$, respectively. They are terminated by load impedances $Z_{L,a1}$ and $Z_{L,a2}$.

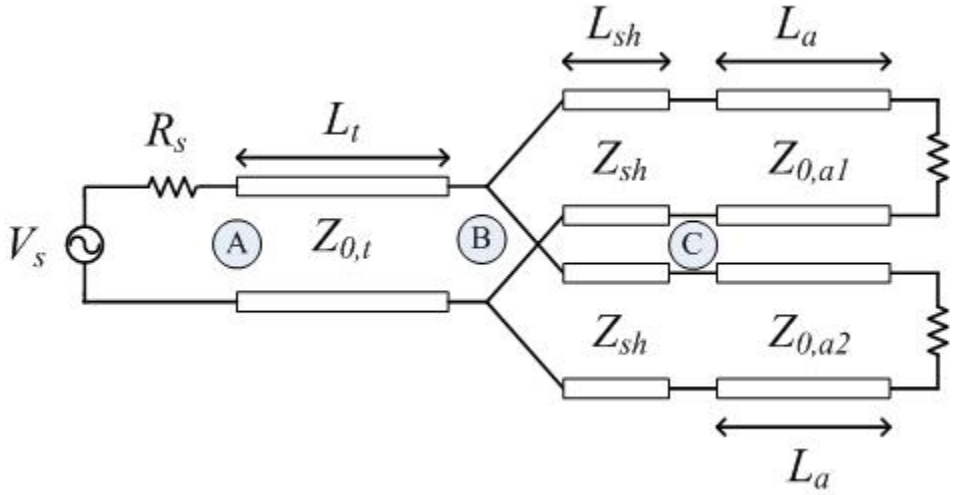

Fig. 46 Parameters for describing transmission line approximation of the garment

Using the standard transmission line equation, (44), we can find the input impedance seen at the source. For simplicity of notation, we start with the arms. Given the parameters of Fig. 46, we find that the input impedance of the arms, just to the right of *Point C* is given as;

$$Z_{in,a1} = Z_{0,a1}\frac{\frac{Z_{L,a1}}{Z_{0,a1}} - j\tan k_a L_a}{1 - j\frac{Z_{L,a1}}{Z_{0,a1}}\tan k_a L_a}$$
$$Z_{in,a2} = Z_{0,a2}\frac{\frac{Z_{L,a2}}{Z_{0,a2}} - j\tan k_a L_a}{1 - j\frac{Z_{L,a2}}{Z_{0,a2}}\tan k_a L_a} \tag{45}$$

These impedances are simply the load impedance on the shoulders. So, looking into each shoulder, just past *Point B,* we can write;

$$Z_{in,sh1} = Z_{sh}\frac{\frac{Z_{in,a1}}{Z_{sh}} - j\tan k_{sh} L_{sh}}{1 - j\frac{Z_{in,a1}}{Z_{sh}}\tan k_{sh} L_{sh}}$$
$$Z_{in,sh2} = Z_{sh}\frac{\frac{Z_{in,a2}}{Z_{sh}} - j\tan k_{sh} L_{sh}}{1 - j\frac{Z_{in,a2}}{Z_{sh}}\tan k_{sh} L_{sh}} \tag{46}$$

Thus, the input impedance at *Point B* is these two impedances in parallel, which is;

$$Z_B = \frac{Z_{sh}{}^2\left(\frac{Z_{in,a1}Z_{in,a2}}{Z_{sh}{}^2} - \tan^2 k_{sh}L_{sh} - j\left(\frac{Z_{in,a1}+Z_{in,a2}}{Z_{sh}}\right)\tan k_{sh}L_{sh}\right)}{c_1 + c_2} \tag{47}$$

where the *c* terms are given as;

$$c_1 = Z_{sh}\left(\frac{Z_{in,a1}}{Z_{sh}} - \frac{Z_{in,a2}}{Z_{sh}}\tan^2 k_{sh}L_{sh} - j\left(\frac{Z_{in,a1}+Z_{in,a2}}{Z_{sh}}\right)\tan k_{sh}L_{sh}\right)$$
$$c_2 = Z_{sh}\left(\frac{Z_{in,a2}}{Z_{sh}} - \frac{Z_{in,a1}}{Z_{sh}}\tan^2 k_{sh}L_{sh} - j\left(\frac{Z_{in,a1}+Z_{in,a2}}{Z_{sh}}\right)\tan k_{sh}L_{sh}\right) \tag{48}$$

Finally, we can write the input impedance at *Point A* as;

$$Z_A = Z_{0,t}\frac{\frac{Z_B}{Z_{0,t}} - j\tan k_t L_t}{1 - j\frac{Z_B}{Z_{0,t}}\tan k_t L_t} \tag{49}$$

In the case where the arms are open-circuited, (47) will simplify to;

$$Z_B = \frac{\begin{array}{r} Z_{0,a1}Z_{0,a2}\tan^2 k_a L_a + Z_{sh}{}^2\tan^2 k_{sh}L_{sh} + \\ j\left[Z_{sh}\tan k_{sh}L_{sh}\left(Z_{0,a1}\tan k_a L_a + Z_{0,a2}\tan k_a L_a\right)\right] \end{array}}{\begin{array}{r} 2\tan k_{sh}L_{sh}\left(Z_{0,a1}\tan k_a L_a + Z_{0,a2}\tan k_a L_a\right) + \\ j\left[\left(Z_{0,a1}+Z_{0,a2}\right)\left(\tan k_a L_a\right)\left(1-\tan 2k_p L_p\right)\right] \end{array}} \tag{50}$$

Due to symmetric geometry, we can further assume that the arm impedances are identical. That is;

$$Z_{0,a1} = Z_{0,a2} \equiv Z_a \tag{51}$$

Thus, we can write;

$$Z_B = \frac{Z_a{}^2\tan^2 k_a L_a + Z_{sh}{}^2\tan^2 k_{sh}L_{sh} + j\left[2Z_{sh}Z_a\tan k_{sh}L_{sh}\tan k_a L_a\right]}{2\tan k_{sh}L_{sh}\left(2Z_a\tan k_a L_a\right) + j\left[2Z_a\left(\tan k_a L_a\right)\left(1-\tan 2k_p L_p\right)\right]} \tag{52}$$

We plug this expression into (49) to solve for the input impedance of the garment. Thus, to evaluate the open circuit impedance, we must know the characteristic impedances of the trunk, shoulders, and arms, and the lengths of the trunk, shoulders and arms (note that all impedances, Z_i, are complex). We also need the spatial frequencies (wave numbers) k which are functions of ε and determine the speed of electromagnetic wave propagation in our garment. These can all be determined experimentally.

6.5. Deriving Transmission Line Parameters

We now seek to verify the transmission line analysis technique using conductive fabric. To do so, we must experimentally determine certain relevant parameters, which can be used to numerically solve the relationship of (49). Specifically, we must know the characteristic impedances wave numbers k, the characteristic impedances $Z_{0,i}$, and the lengths l.

6.5.1. Wave number

The wave number, k, in units of m^{-1}, governs the speed of wave propagation in the transmission line. For the parallel plate transmission line, we can write;

$$k = \frac{2\pi}{\lambda} = \frac{2\pi f}{c}\sqrt{\varepsilon_{rel}} = \frac{\omega}{c}\sqrt{\varepsilon_{rel}} \tag{53}$$

Thus, given the transmission frequency, the unknown is the relative permittivity, ε_{rel}, of the insulator. Further, we must account for the lossy nature or our transmission line. Specifically, the conductive fabric has a finite conductivity σ that modifies the effective permittivity according to;

$$\varepsilon_{eff} = \varepsilon - j\frac{\sigma}{\omega} \tag{54}$$

Thus, the permittivity, and thus the wave number, depends on frequency and conductivity. To find the actual conductivity of our cotton insulator, we use the conductive fabric as a dielectric in a capacitor. We set up two metal plates in a capacitive formation according to Fig. 47. We then use an impedance analyzer to experimentally determine the capacitance. Finally, we use the relationship;

$$C = \frac{\varepsilon A}{d} \tag{55}$$

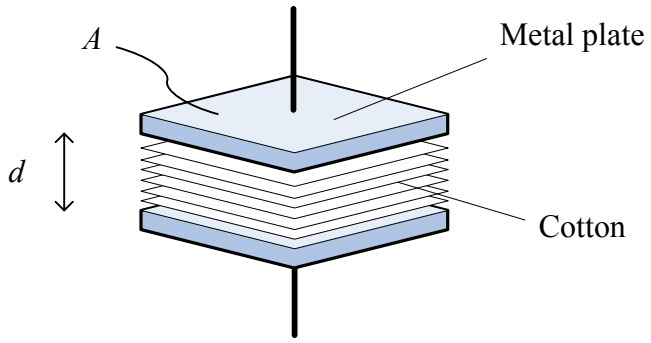

Fig. 47 Measuring conductive fabric permittivity

6.5.2. Characteristic Impedance

Now, refer again to (49); this equation is dependent on three characteristic impedances; that of the arm ($Z_{0,arm}$), the shoulder (Z_{sh})and that of the trunk ($Z_{0,trunk}$). As part of our model, we assume that the arm and trunk are distinct transmission line sections connected by a shoulder section. As such, they have distinct characteristic impedances that will be a function of their material and geometric properties. Thus, if we know the bulk inductance and capacitance for our trunk and arm section, we can solve for the characteristic impedance. On first thought, we might expect to apply the closed form solutions for L_{ul} and C_{ul} directly. For a coaxial cable (that is, two concentric cylindrical conductors), we can write these as;

$$C_{ul} = \varepsilon \frac{2\pi}{\ln(R/r)}$$
$$L_{ul} = \mu \frac{\ln(R/r)}{2\pi} \tag{56}$$

However, these equations cannot be applied directly. One reason for this is the material properties of the conductors. Because we use non-ideal conductors, the real capacitance is likely to be lower than what this model predicts, and the inductance is likely to be higher. Further, the actual transmission characteristic is not that which is implied for (56). As with the discussion of DC transmission, we transmit from a point to a point, while these equations imply that the entire conductor cross-section is used (See Fig. 48).

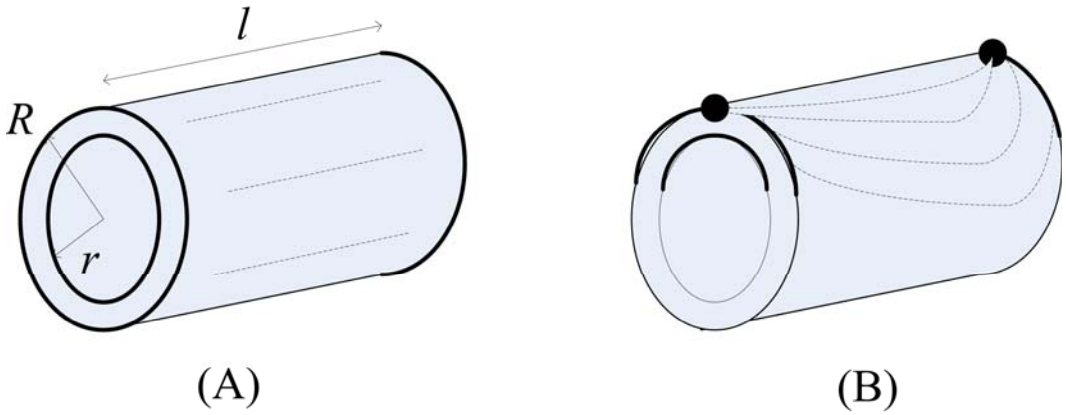

Fig. 48 Cylindrical section with ideal transmission characteristic and actual transmission characteristic

Thus, we expect the inductance and capacitance to be of the form of (56), but expect deviation in the actual values.

To verify our hypothesis, we perform the following experiments. The characteristic impedance of a cylindrical section cannot be measured directly; the bulk impedance and capacitance can. To do so, we create cylindrical sections of varying lengths (but of the same diameter) and use cotton as an insulator between the two layers. The conductive fabric is then sewn onto a solder-board; subsequently, an SMA connector is soldered to the board for a robust connection, with predictable impedance characteristics (See Fig. 49).

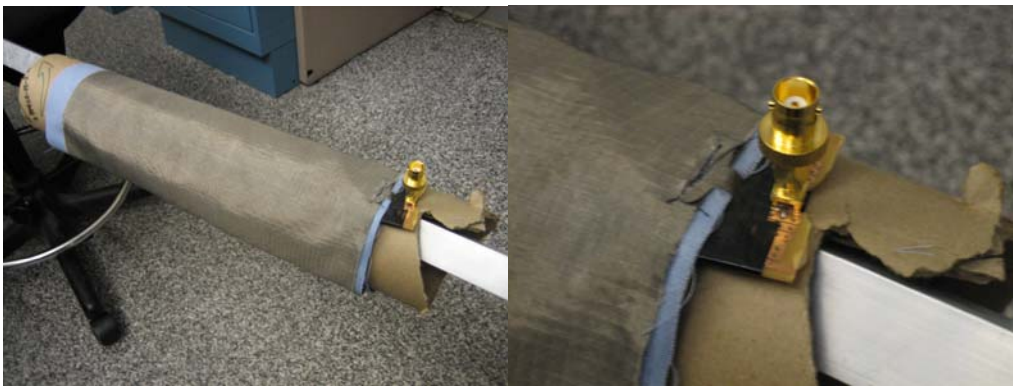

Fig. 49 Cylindrical section with SMA-to-solder-board connection

To obtain our results, we used an HP impedance analyzer. Results were confirmed using a vector network analyzer. First, we note that both (38) and (56) imply that, if we change only the length of the transmission line, the capacitance and inductance per unit length will not change. Experimentally, we find that this is not the case for our geometry. The capacitance and inductance per unit length are plotted versus length in Fig. 50.

Here, C_{ul} and L_{ul} vary inversely with the length. When considering our results for the DC analysis, this makes sense. Our DC analysis showed that, because we are not using the entire conductor cross section, but rather a single point, the resistive (or impedance) characteristics do not vary linearly with length. Since these values were found from sections of the same diameter, we also seek to find the effect of changing the diameter on C_{ul} and L_{ul}.

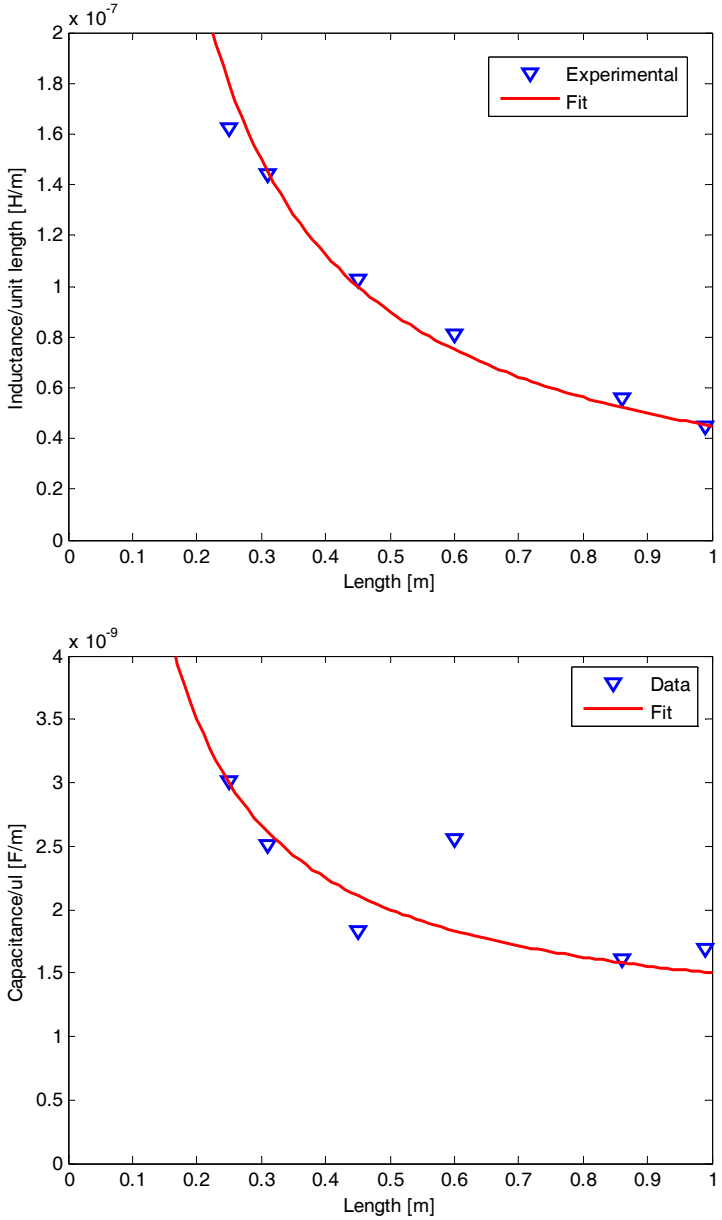

Fig. 50 Capacitance and inductance versus length for cylindrical conductive fabric sections

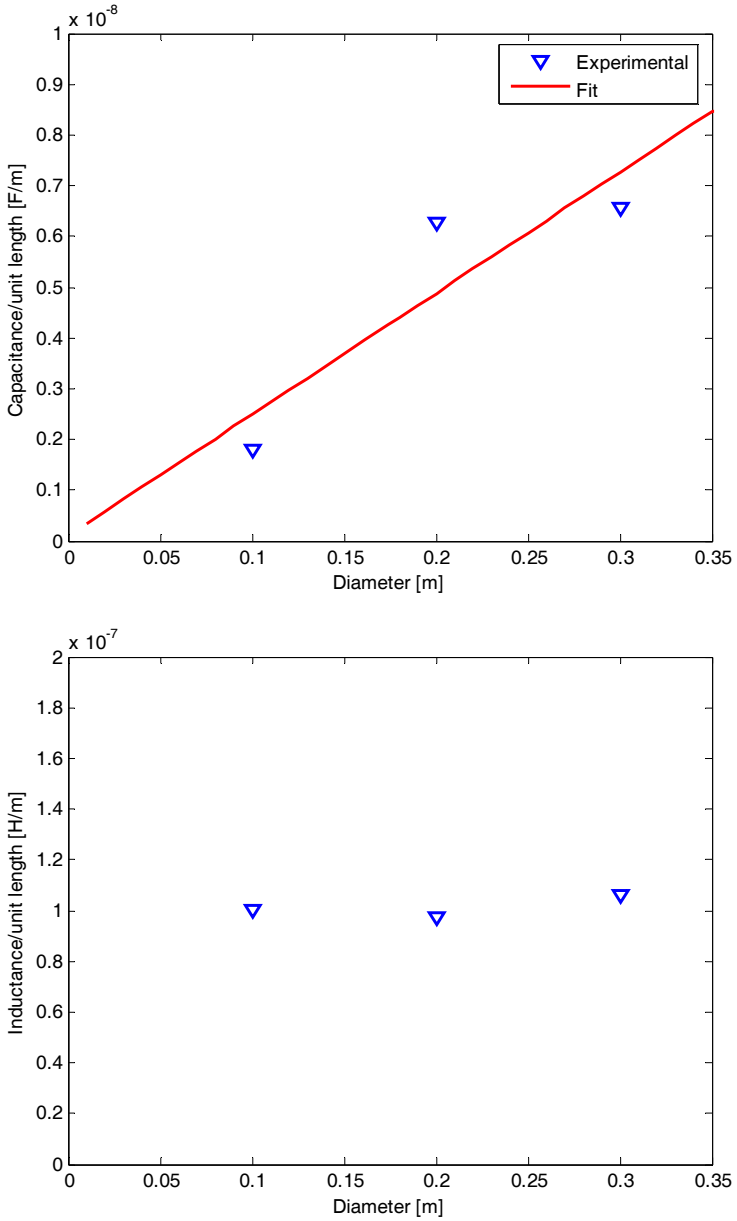

Fig. 51 Capacitance and inductance per unit length versus diameter

In these experiments, using a fixed length of 0.46m, we varied the diameter from 0.1, 0.2, and 0.3m. Thus, we see that C_{ul} can be approximated with a linear fit, while L_{ul} does not vary significantly with diameter. Thus, neither (38) nor (56) can be applied directly to predict the C_{ul} and L_{ul} characteristics. This is expected, as capacitance is proportional to area. However, the inductance per unit length does not appear to vary with diameter. This is expected, as inductance is proportional to length, which was held constant to produce the results of Fig. 51b.

As a result, our technique is as follows. For a given section, we first determine the length, L. Next, we use the fit of Fig. 50a to find the value of the curve that corresponds to this length. Then, using the section diameter D, we scale using the linear curve of Fig. 51a to find the C_{ul} value. Due to the lack of dependence on D, the technique for finding L_{ul} is similar, but omits the second step; we need only consult Fig. 50b. Following this procedure for the trunk section, we find that $Z_0 = 3.55\Omega$, whereas experimentally, we find $Z_0 = 3.71\Omega$.

Following this method, we know that the arm dimensions are $D = 9.8$cm, and $L = 33.5$cm. The trunk has $D = 33.5$cm, and $L = 70$cm, so the characteristic impedance for the arm and trunk are 23.09Ω and 17.89Ω, respectively.

6.5.3. Equivalent Length

Also critical to the calculation of the impedance is the length z at which the impedance is being measured. In fact there will be an 'effective' length for calculations. That is, our transmission line model is based on an ideal parallel plate capacitor. However, the non-ideal geometry of the garment means that there may be deviation from the expected TEM wave mode. Because of this, the actual distance between a transmission and reception point may not accurately reflect the measured impedance. Based on the discussion of the field line behavior in strips from Section 4, we can make certain hypotheses. Here, we use our FEA program to look at the E-field lines on cylindrical sections. To represent the results visually, we 'unwrap' a cylinder according to the schematic in Fig. 52.

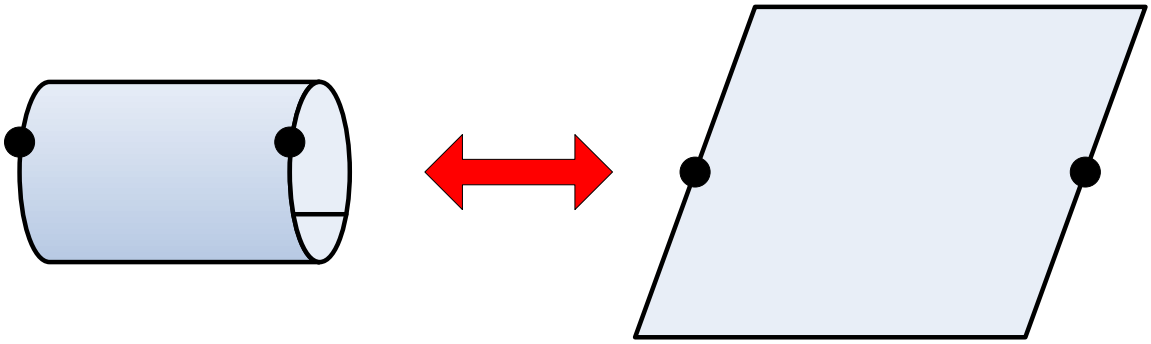

Fig. 52 Unwrapping a cylinder for visual representation

By 'wrapping' the strip axially, we have created our cylinder, and thus we expect to see similar electrical behavior to that described in Section 4. To understand visually how the equivalent length manifests itself, we look again at the field lines in a strip.

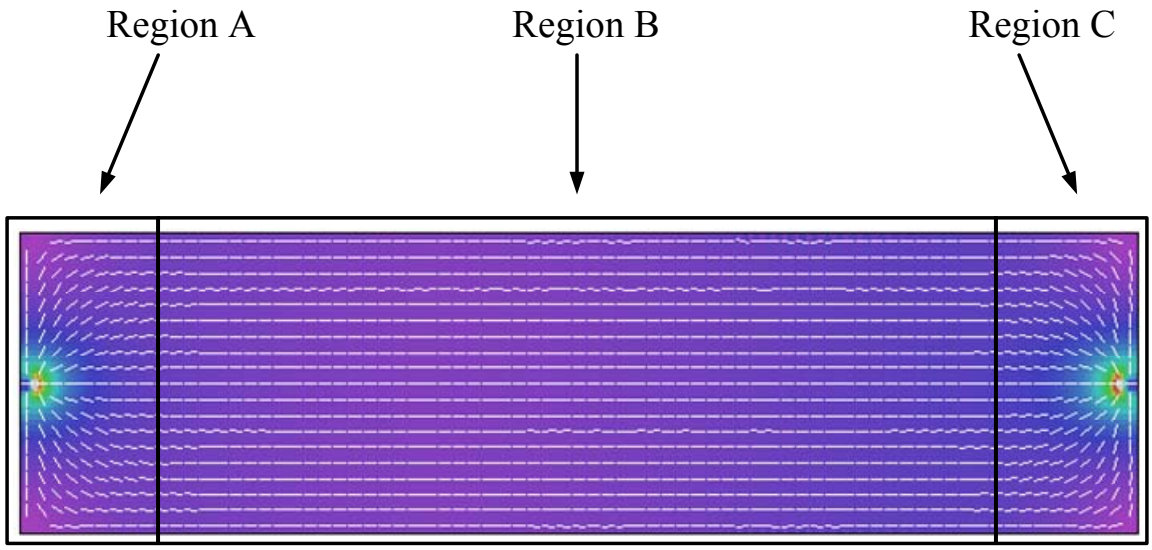

Fig. 53 Field lines in a conductive fabric strip, with linear region highlighted

In Fig. 53, the field lines are curved in regions A and C. However in region B, the field lines are primarily linear. Thus, region B would look very similar if the probe points in regions A and C were the full width of the strip. Therefore, the difference between a strip with full-width probes and point probes is primarily in the ends, or regions A and C of the figure. In these regions, the full area of the strip is not used for conduction. As a result, the effective impedance of regions A and C is larger than what one would be expected based on their lengths. As a result, we can draw the schematic of Fig. 54.

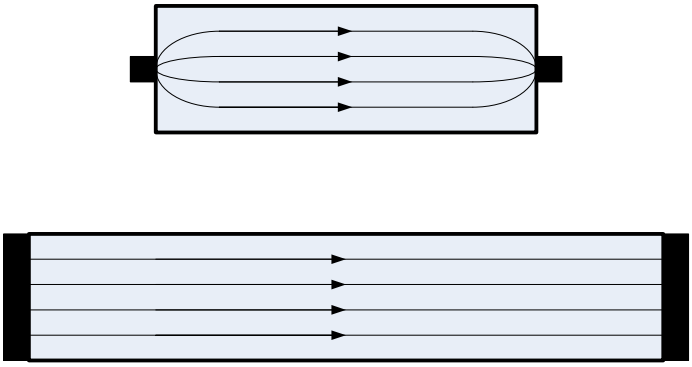

Fig. 54 Two strips of equivalent impedance; one with point probes, and one with full-width probes

There are two strips in the figure; in each case, the impedance between the probes is the same. However, due to the geometry of the probes, the total length of each strip is different. We can redraw these strips in Fig. 55

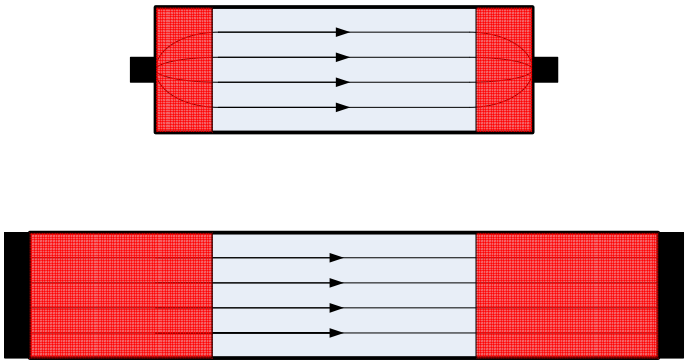

Fig. 55 Two strips of equivalent impedance, with like regions shaded

Now, the shaded areas have the same contribution in both cases. The un-shaded areas contribute the same amount of impedance in both cases, but due to the field line geometry, they have different lengths.

Thus, what we expect that, when calculating impedance in the cylindrical sections, our empirical measurements will be of a higher magnitude than the model prediction. We must then use the governing physics and geometry to be able to predict and *equivalent length* to be used in impedance calculations, and plugged into (49).

Using the conductive fabric cylinders described in 6.5.2, we measured the input impedance using an impedance analyzer. This input impedance is described in (45). In the previous sections, we describe how the other parameters are obtained. Thus, given a measurement of Z_{in}, we need to tune only the length to ensure that the model result matches the experimental result. In this

way, we can solve for the equivalent length as a function of the actual length. An example of experimental data compared to the model is shown in Fig. 56.

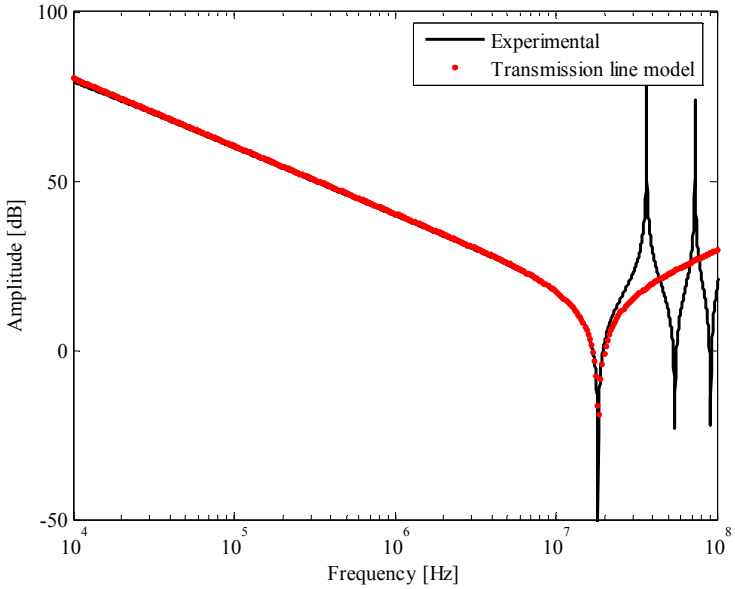

Fig. 56 Model and experimental results for a cylinder with D/L of 0.167

As a result, we can plot the value of $L_{equivalent}$ as a function of the actual length in Fig. 57. As with the Z_0 calculation, we use both plots in order to determine the equivalent length for a given section. The fit from Fig. 57a is described by;

$$L_e = 1.66L_a + 1.87 \tag{57}$$

The fit from Fig. 57b is described by;

$$L_e = 12.25D + 1.62 \tag{58}$$

Thus, to calculate L_e using the diameter and length, we use start with (57) to find the initial guess for L_e, L_e'. Subsequently, we need to scale this L_e guess by the slope of Fig. 57B to adjust for the actual diameter.

Using the trunk section for verification, which has D = 0.70m and L = 0.33m, we calculate L_{eq} = 6.1m.

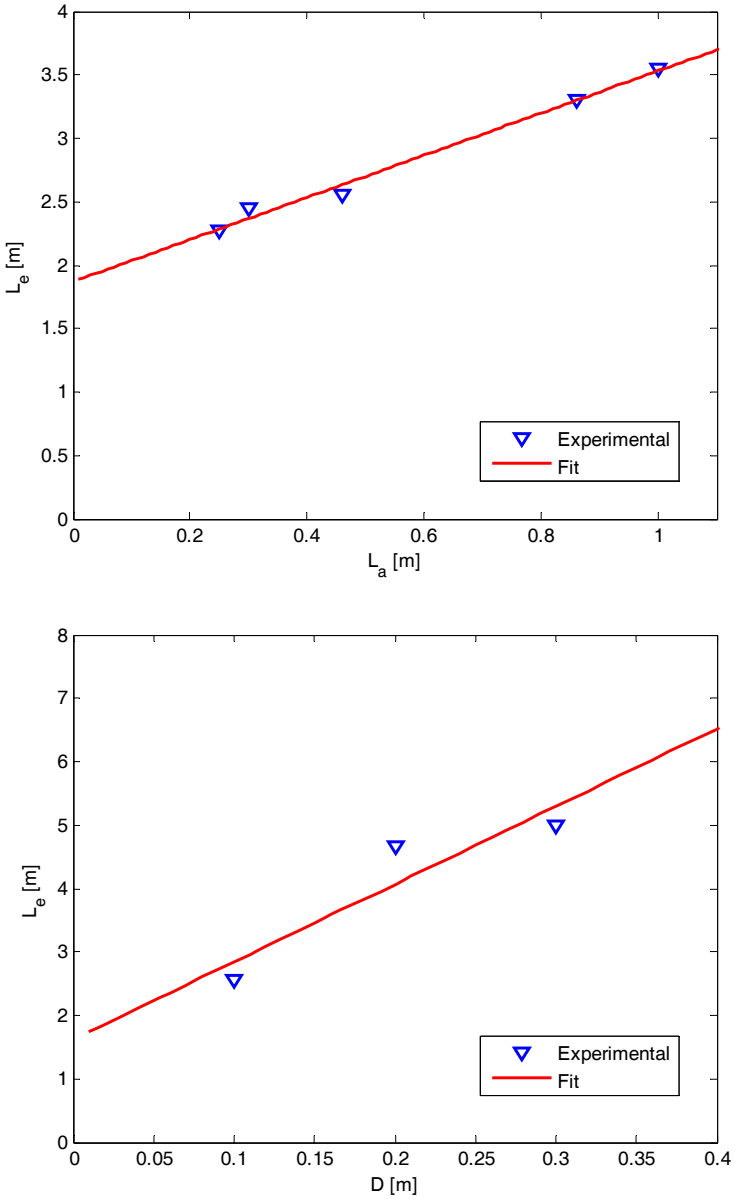

Fig. 57 Equivalent length versus actual length and diameter for cylindrical sections

6.6. Shoulder section

As we did in our DC analysis, we must determine how the shoulder affects our AC analysis. Once again, we will assume that the shoulder has much less of a contribution to the overall characteristic than the arms and trunk; using finite element analysis, we will find 'typical' impedance characteristics, and use these to validate our experimental results.

We treat the shoulder as a short transmission line, as depicted in Fig. 45. As such, it has its own characteristic impedance. Again, using human factors data, we fit shoulders for the 98th percentile of the population. Because we are interested in the transmission line properties, we must model both layers of conductive fabric, as depicted in Fig. 58.

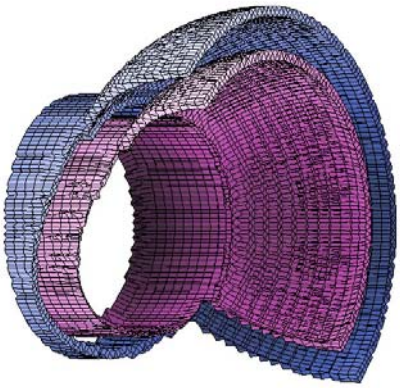

Fig. 58 Finite element model of shoulder used for capacitance tests

Here, the cotton insulation between the outer and inner conductive fabric layers has been omitted for clarity. Using the FEA program, we can extrapolate the capacitance and inductance of the geometry. This is done using perfect conductors. Subsequently, the conductivity of the fabric is taken into account when considering the dielectric constant, according to (54).

The results for capacitance, for 25 samples, were 0.65nF ± 0.07nF, and the inductance 0.026nH ± 0.0045nH, resulting in $Z_0 = 2.0\Omega$ and $t_d = 0.13$ns. Thus, we can plug these values into our model when considering the overall garment transfer function. This result cannot be independently verified; rather, the assumptions will be validated when evaluating the entire garment's behavior.

6.7. Verification

Thus, to validate our work, we demonstrate our ability to predict individual cylindrical section behavior, and subsequently, the overall garment. First, we present the open-circuit impedance characteristic of the trunk and arm sections using (45), compared to the experimental results. These results are shown in Fig. 59.

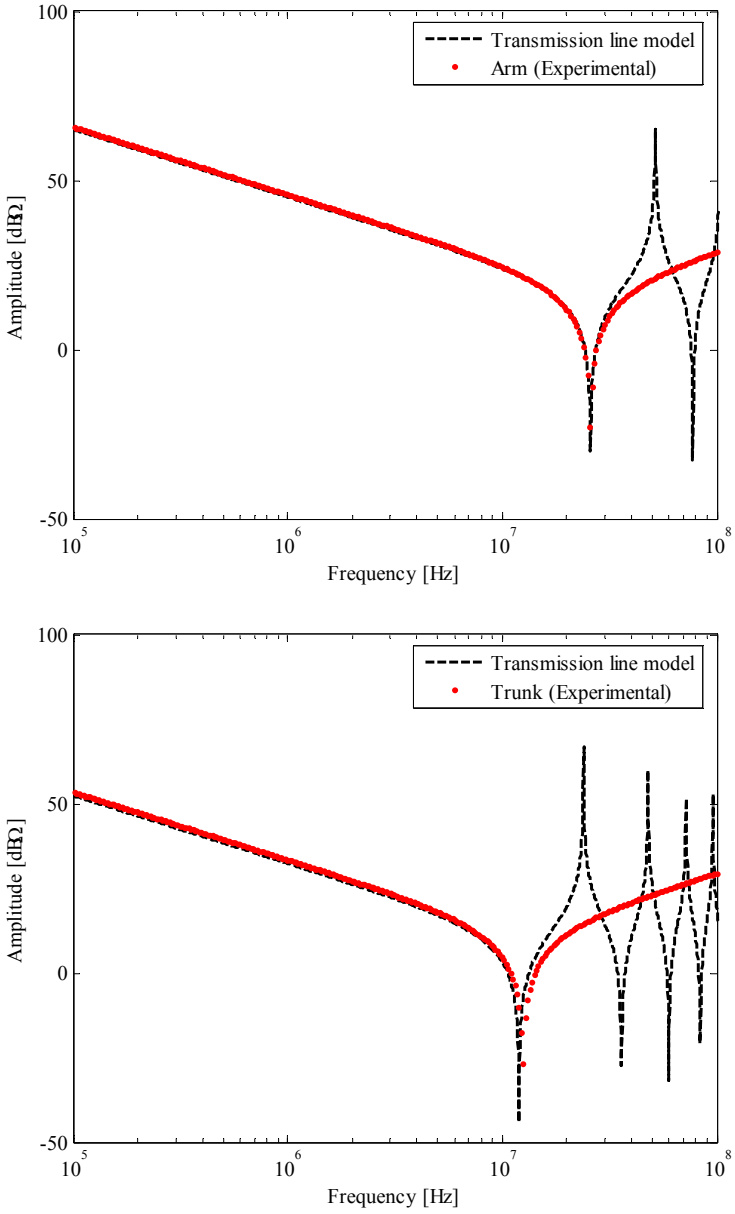

Fig. 59 Impedance characteristic for arm and trunk sections

Note that there are poles and zeros evident in the higher frequency range. This is due to the model capturing the high order poles and zeros that result from the distributed nature of the

garment. The experimental result captures only the bulk L_{ul} and C_{ul}, which manifests itself as the simple *LC* impedance response. Now, using the model of (49), we have a method for calculating the impedance of the entire garment. We can simultaneously plot the model and experimental results, which are shown in Fig. 60.

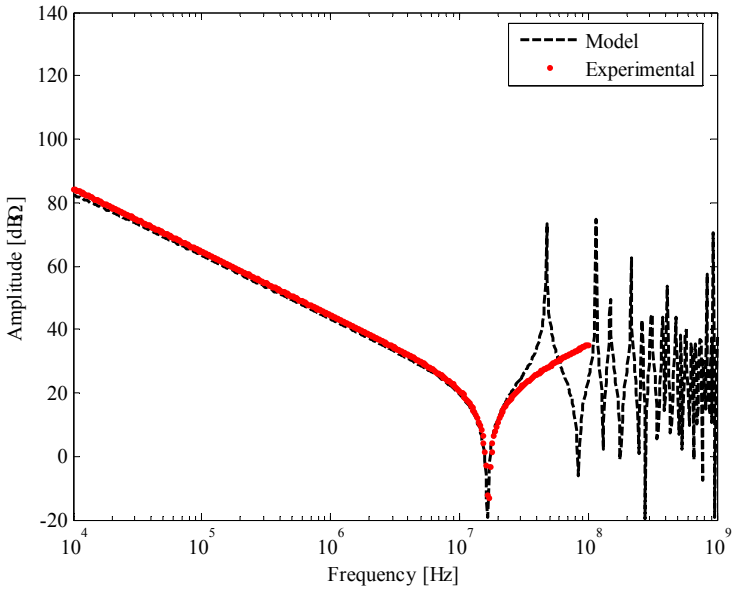

Fig. 60 Impedance for open-circuited garment

Here, the experimental values end at 10^8 Hz due to limitations of our measurement equipment. In both cases, the model and experimental results show close agreement. This confirms our model structure, and verifies that our approximations for equivalent length are appropriate.

7.Garment Fabrication and Performance Tests

We now perform tests and experiments to obtain practical design considerations for conductive fabric garments. We first discuss the relevant details of the garment fabrication, then go on to discuss relevant characteristics and specifications.

7.1. Garment fabrication

Here, we describe the physical construction of our wearable DC-PLC system. We will begin by describing the sensor nodes and the centralized components. Next, we discuss the design of the CF medium used to connect the electronic components to the body. This will all be discussed within the framework of determining which physiological signals must be measured.

We devise three specific design requirements for the physical construction of the garment. In order to be useful for our target population, we want to be able to take sensor measurements at any point on the body. Our garment should be truly ubiquitous on the body and cover the trunk, arms, and legs.

In addition, we want to ensure that the garment facilitates DC-PLC on the body. The CF garment transmission medium must be able to maintain adequate line impedance such that simultaneous power and data delivery are possible.

Finally, and most importantly, we wish to minimize the burden on the user. Specifically, wearability metrics must be taken into account such that the user feels no undue difficulty while using the system. Thus, the garment must not be restrictively constraining. The weight of components must be distributed on the body so as not to have a large concentration at any one point on the body. Similarly, the bulk of components should be distributed. Also, the size of all components must be minimized. Further, there are certain vague intangibles that affect the user's perceived burden which must be taken into account. For instance, technical complexity might pose unnecessary stressors on an elderly user.

We achieve these goals by combining DC-PLC with conductive fabrics. The DC-PLC technique ensures that we need only two conductors for the body area network. Thus, the

garment is constructed using two layers of CF and 1-to-3 layers of insulation sandwiched together (See. Fig. 61).

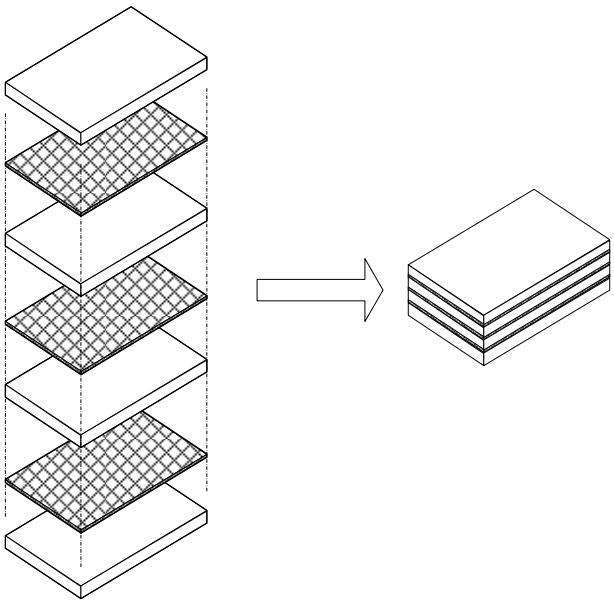

Fig. 61 Layering of conductive fabric and insulation

By using conductive fabric in this method, we ensure that the garment looks and feels like a normal garment to the user. Further, the CF covers the entire body such that sensors can be place anywhere. In general, a sensor node is connected to the garment using the fixturing method depicted in Fig. 62.

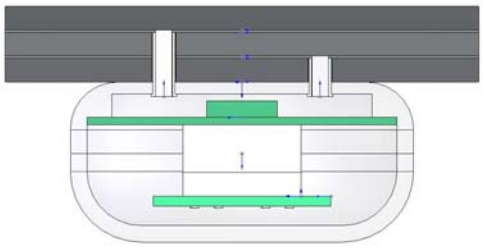

Fig. 62 Method for connecting sensor nodes to the conductive fabric garment

It has two connectors, where one must be shielded to prevent contact with the other conductive layer. The actual sequence for physically connecting the sensor nodes to the garment is depicted in Fig. 63.

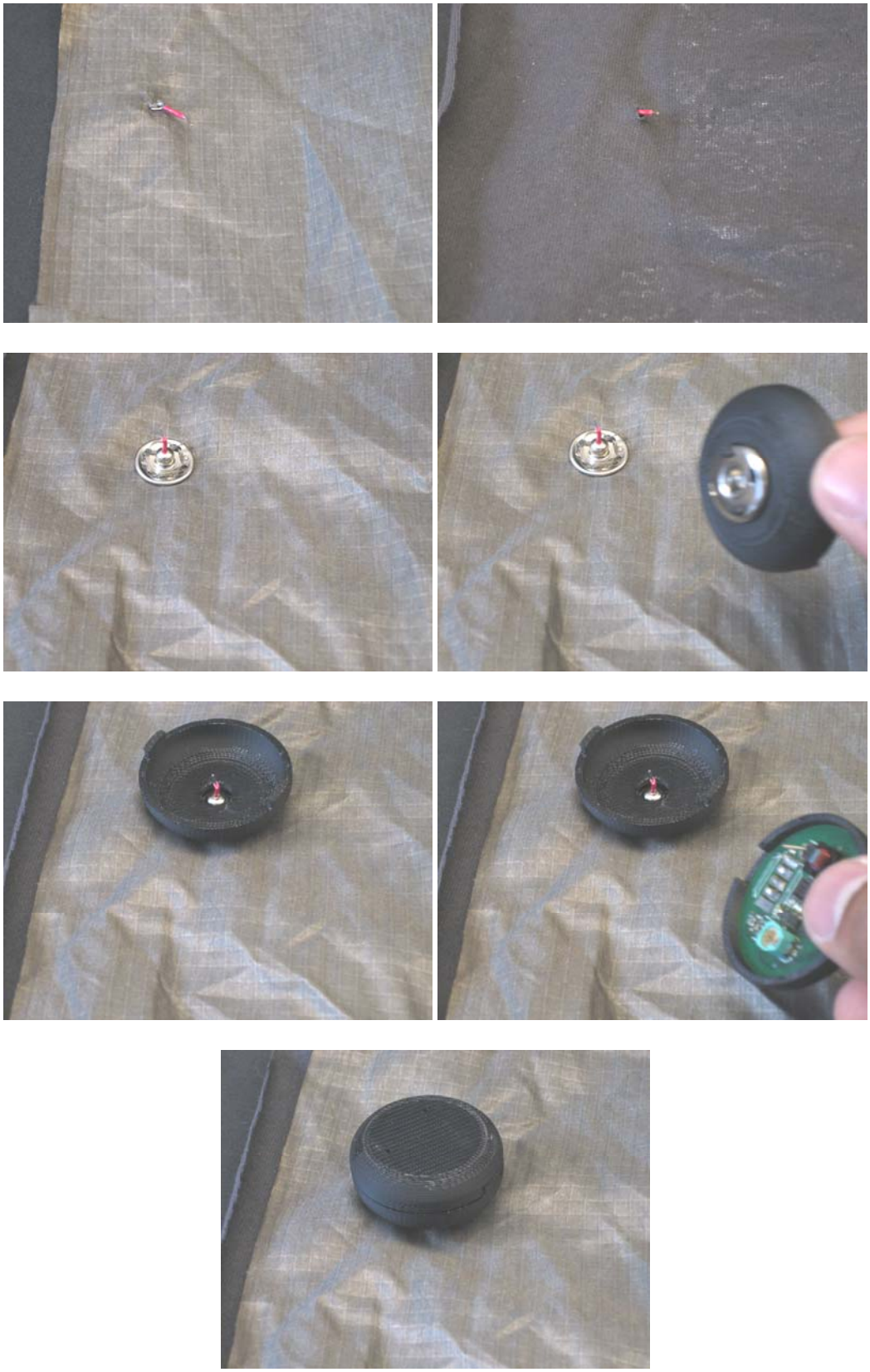

Fig. 63 Sequence for placing sensors on garment

First, a shielded contact is sewn to the inner layer of fabric. Next, this shielded connecter is routed through the insulation and through the metallic snap button on the outer layer. Thus, the metallic button acts as the electrical connector for the outer layer, while the insulated wire acts as the connector for the inner layer. The actual sensor node contains the mating button snap, which also has a hole in the center, through which the insulated connector passes. Finally, the sensor board maintains a mechanical contact with the inner layer through the insulated connector, and with the outer layer through the metallic snap button. Variations on this node design will be made depending on the type of sensor. We will now discuss in detail the design of these components and how they meet our design requirements.

To avoid hazard due to short circuit, a fuse is placed in the sensor nodes and at the central components. Thus, while the system will shut down upon noticing a short circuit, there is no danger to the user, as the battery connection is broken.

We also note that, for additional comfort, changes can be made. For instance, different materials of varying breathability and flexibility can be used depending on climate; for instance, lighter, more breathable materials are optimal for higher temperature environments. In addition, certain sections of the garment can be removed. For instance, the underarms are not a likely location for a sensor. As a result, the underarm section can be removed, which does not drastically affect impedance or resistance characteristics, but adds an additional conduit through which air can pass.

7.1.1. Electronic Circuit

The electronic components in the circuit modem are designed to interface with the DC-PLC CPS bus and a variety of sensor types. For any given sensor, we must determine the operating power requirements and the data type. For power, this pertains to maximum operating voltage and current. For data types, we must ensure that the modem can process analog and digital, single- and multi-channel signals. In terms of the protocol of the DC-PLC system, we require modulated digital signals to be sent on the CPS. Thus, we must include this capability in our modem

To describe the circuitry, we will present the example of a sensor node built around an off-the-shelf MEMS accelerometer. MEMS accelerometers work on the premise of measuring deflections in a micro-scale cantilever beam in order to measure acceleration. This acceleration is converted to an electrical voltage output. Typical MEMS accelerometer voltage outputs are

analog signals, or pulse-wave modulated (PWM) signals. In case we use an accelerometer with analog output, our modem must (1) digitize the data signal, (2) modulate the signal, (3) and superimpose the data signal on the CPS. These steps are done using and analog-to-digital (ADC) converter, a phase-locked loop (PLL), and the DC-PLC circuitry and TLT combination described in Section 3. The actual circuit can be seen in Fig. 64.

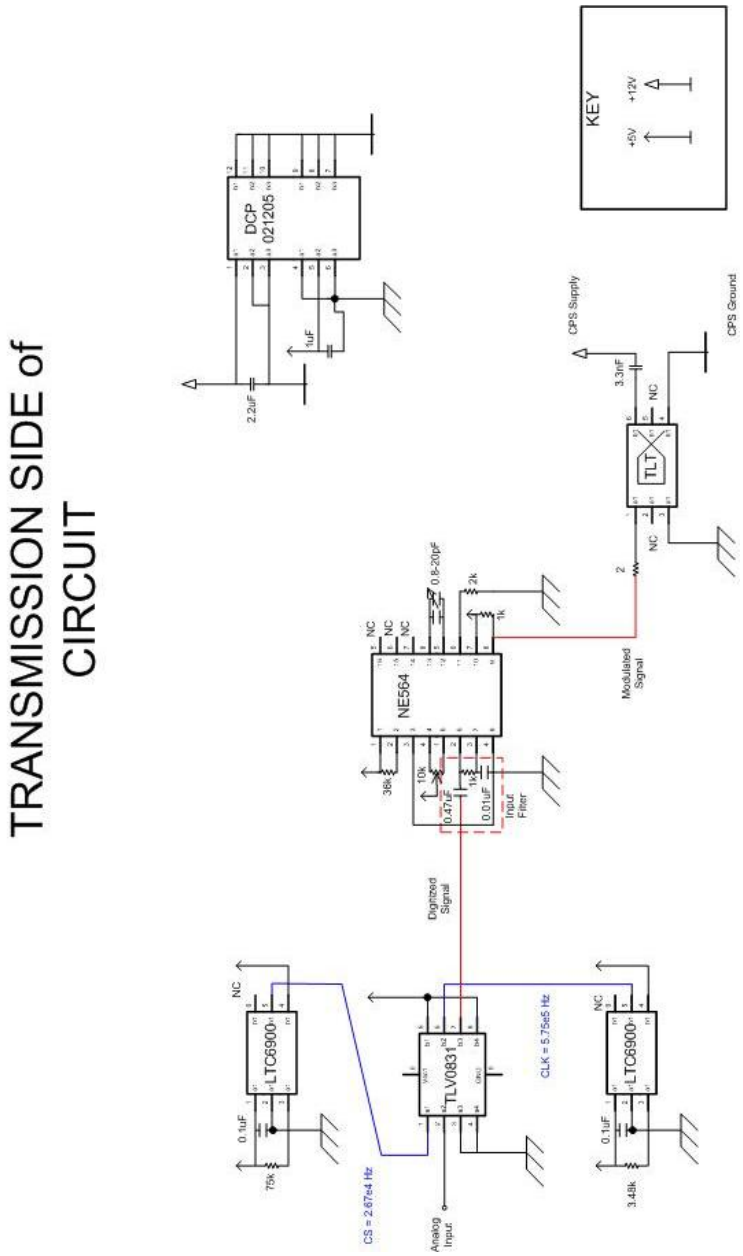

Fig. 64 Transmission side of DC-PLC circuit components

The actual chip sets used can be seen in Fig. 64. The LTC6900 chips are variable oscillators that have resistor-dependent frequencies. When used in conjunction with the TLV0831 ADC, we

can determine the sampling frequency and interval sizes for the incoming analog signal. The digital output is then modulated in frequency using the NE564 phase-locked loop, and finally superimposed on the CPS using the TLT-capacitor combination described in Section 3. We are simultaneously providing power using the DCP021205 DC-to-DC converter, which converts the 12VDC provided on the CPS to the supply voltage of the sensor. This supply voltage is also dependent on the chip's output resistors and capacitors.

This is the basic circuitry used in the modem design. We also allow for Schmitt-trigger inverters and voltage followers at various points to improve signal integrity. Such components are best used at the PLL output on the digital signal.

In this way, the signal processing circuitry can be made to fit a variety of sensors. Adjusting the resistors used with the oscillators changes the digital sampling rate; similarly, changing the resistors of the DCP021205 changes the DC conversion from the DC on the CPS to the sensor supply voltage. Using these components gives us frequency sampling rate between 1kHz and 20MHz. If necessary, both the analog sampling frequency and the DC voltage supply range can be changed using different chipsets in our modem.

7.2. Performance tests

7.2.1. Garment shape

In the previous chapter, we described the garment impedance. Here, we look to determine how crumpling might affect this behavior. To do so, we measure the open-circuit impedance when the garment is mounted on the test model and crumpled and resting on bench-top, as pictured in Fig. 65. Here, we show two degrees of 'crumpling' denoted *Resting* and *Crumpled*.

Fig. 65 Garment on model, resting, and crumpled on bench-top

The resulting impedance curves are shown in Fig. 66.

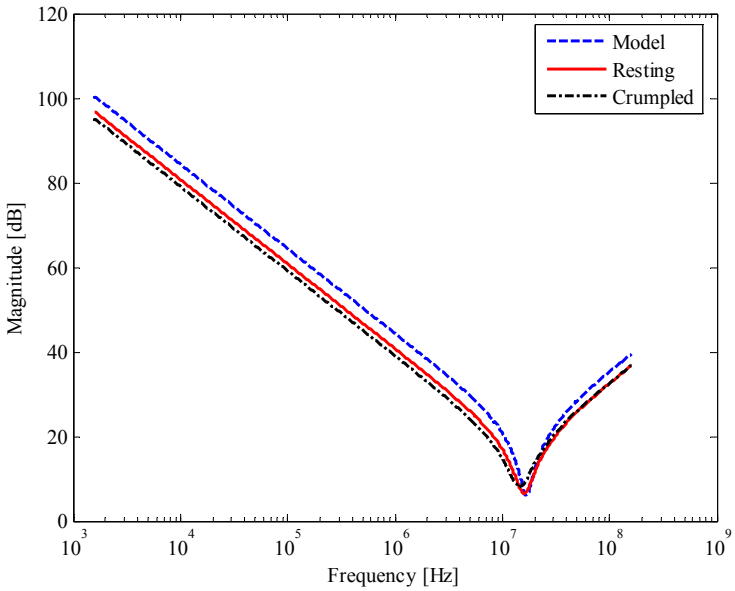

Fig. 66 Impedance curves for garment on the model, resting, and crumpled

Between the model and crumpled results, we see variations in inductance and capacitance of 30nH and 796pF, respectively. Thus, we can expect a range of characteristic impedance of 3.6Ω depending on the user's position.

7.2.2. Effect of garment on transmission properties

To evaluate the effect of the garment on transmission properties, we place the garment on a test subject, and measure the sensor output directly from the accelerometer while also monitoring the demodulated signal. Thus, we know the 'true' signal, and can also look at the signal modified by the channel properties. Typical PWM sensor output data is shown in Fig. 67

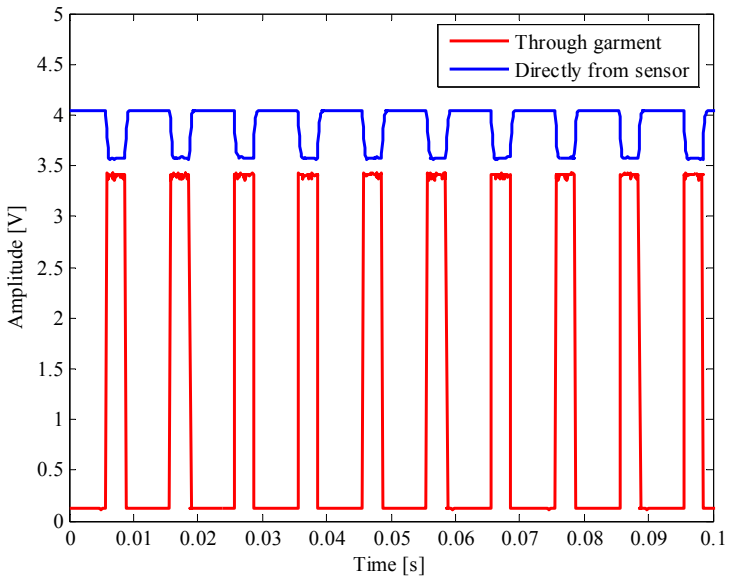

Fig. 67 PWM sensor output during motion

We can also look at the demodulated output in Fig. 68. Note that there are spikes, specifically at 11s and 16s. These are the result of errors in the bit sequence. Because the position data is reconstructed from digital pulse widths, a bit error can result in a pulse going low prematurely, which corresponds to a lower pulse width, and smaller resultant value for position. The modulation performed by the FSK chipset may sometimes be imperfect, causing such errors.

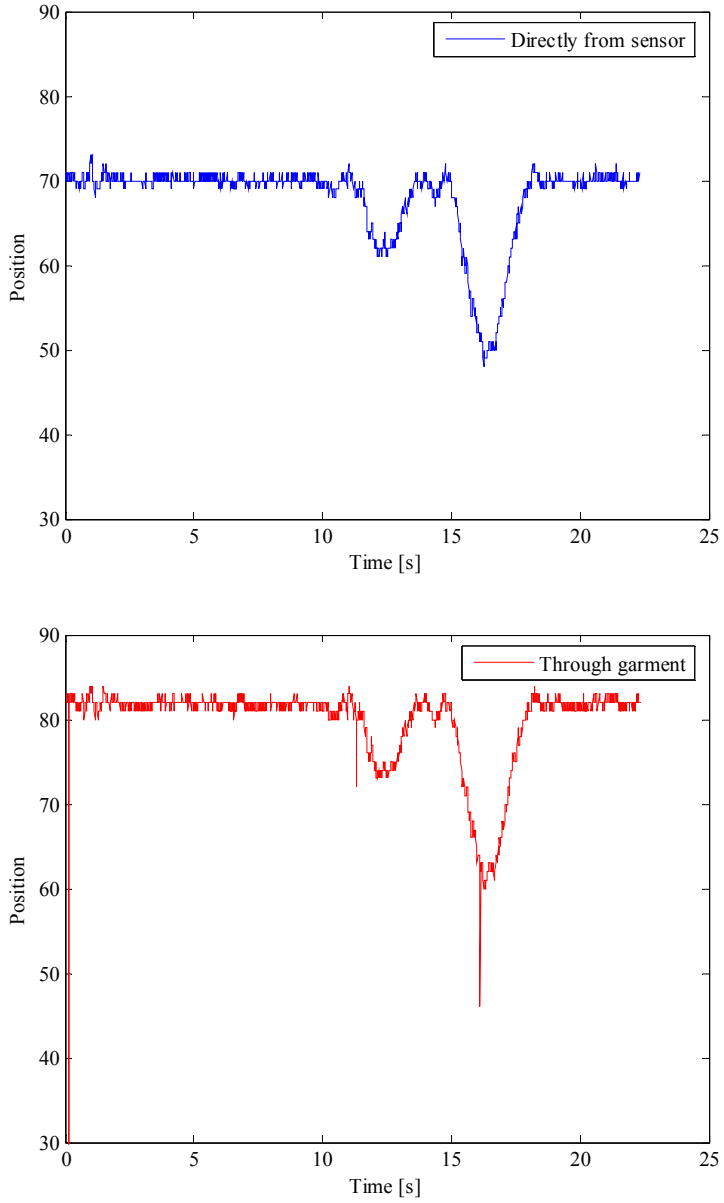

Fig. 68 Demodulated motion measured directly from the sensor and through the garment

7.2.3. Motion artifact

We can also evaluate the motion artifact. For this experiment, a test subject wore the garment, and the sensor node, in this case a MEMS accelerometer attached to the user's wrist, was secured using a bench-top vise (this was done to prevent sensor motion, and ensure that any noise was due to the movement of the transmission medium). Noise was induced my shaking the garment along the sleeve, and along the body as well. This was done to evaluate the location-dependence of noise sources. First, we show the sensor PWM signal output and the demodulated PWM output in Fig. 69. In Fig. 70, we show the actual position information.

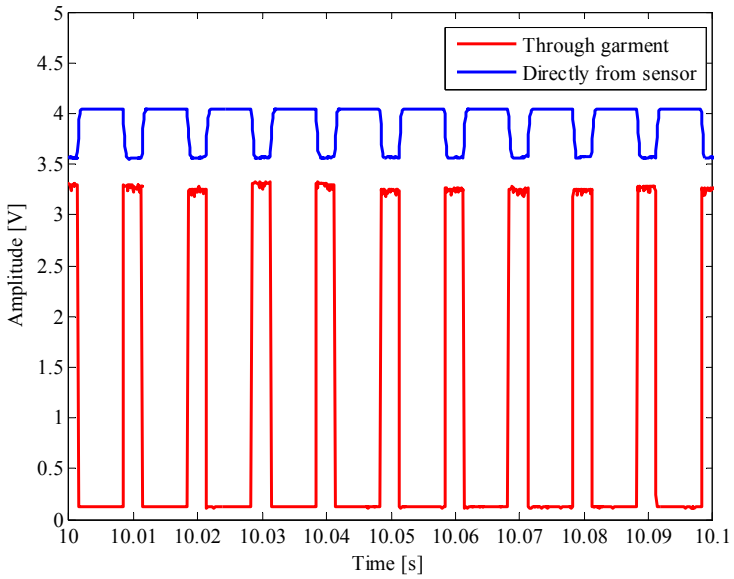

Fig. 69 Accelerometer PWM signal directly from sensor, and measured through the garment

Here, the noise that occurs at 9s is of higher amplitude that that at 12s. This indicates the path -dependence of noise, and verifies what we might expect; if the noise source is located along the primary, most direct path between the sensor and the receiver, it will have a more noticeable effect than if it is at a more peripheral location. The induced noise manifests itself as spikes that must be filtered out to avoid errors.

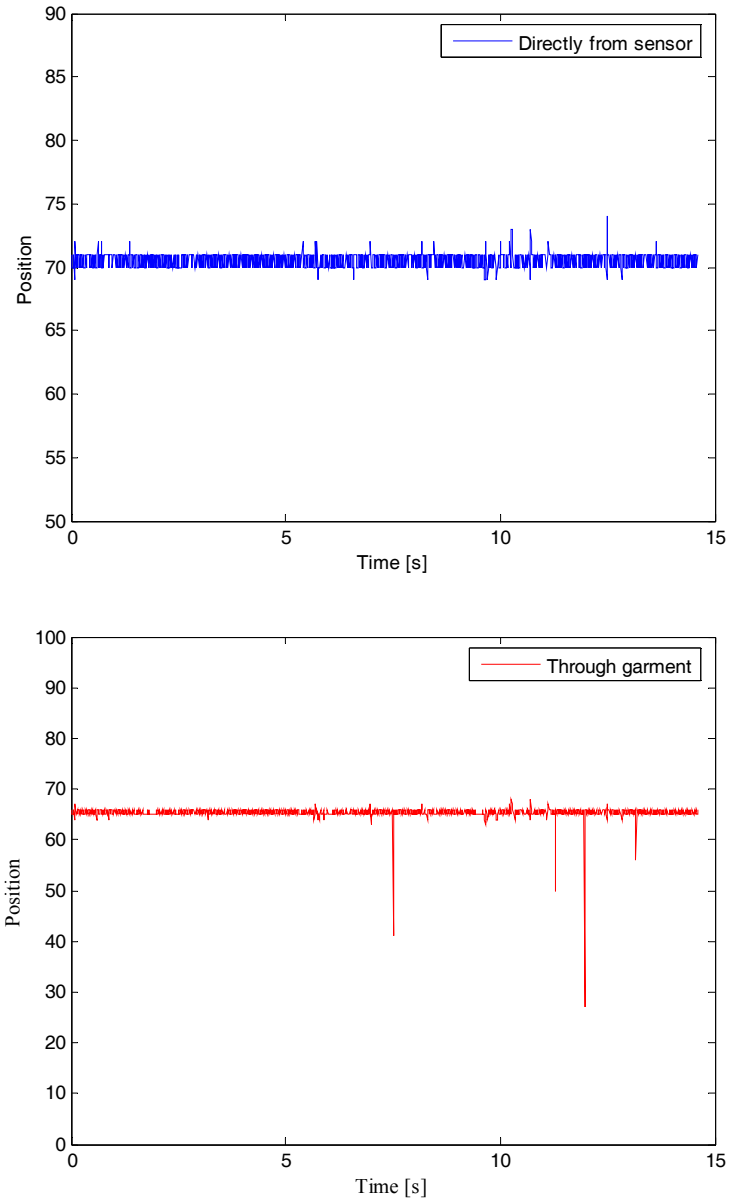

Fig. 70 Position information gained directly from sensor, and measured through the garment

8.Applications

The focus of the garment is on measuring physiological signals from the user. However, we do not restrict the type of sensor that must be used. Rather, we build sensor nodes that can interact with any number of off-the-shelf sensor types. In considering the physical construction, we must minimize sensor node size, bulk, and weight. The sensor node must also be rounded and smooth to match the form factor of the human body.

8.1.1. Physical Construction

To describe the physical design, we must determine what measurements are interesting and useful for determining the user's physical condition. In fact, there are a number of useful sensing techniques that are sufficiently mature for this work. We describe typical sensors and their relevant physical characteristics.

8.1.1.1. Plethysmography

Plethysmography is the technique of assessing changes in body volume and organs by measuring changes in blood volume. Typical useful parameters are oxygen saturation in the blood, pulse, and heart rate variability. There are a number of methods for implementing plethysmography. For instance, photo plethysmography involves shining a light into the skin, and observing the reflected light signal. For such applications, the sensor must be in direct contact with the skin.

8.1.1.2. Temperature Sensing

Skin temperature indicative of body core temperature, which is in turn an indicator of the physical health condition. Such sensors are typically small, but must obviously be in contact with the skin

8.1.1.3. Motion Sensing

Motion can be measured using sensor such as rate gyros or accelerometers. Accelerometer can be used in conjunction with inverse kinematics to reconstruct the biomechanical model. MEMS accelerometers have ideal size and shape for such applications. The accelerometer should be physically shielded from the environment to prevent noise from the environment, but must also be secured such that it does not move relative to the limb on which it is mounted.

8.1.1.4. Electrocardiogram

The electrocardiogram (ECG) is a test that detects heart abnormalities by measuring electrical potentials on the body surface. It requires leads to be placed directly on the skin. This sensor must also be placed in direct contact with the skin, and involves 3 or 12 leads simultaneously connected to the body

8.1.2. Sensor Shell and Physical Construction

The actual physical construction depends on the sensor type. Each sensor node must (1) be secured to the garment, (2) be in contact with the physiological source, and (3) contain both the sensor and the modem. To minimize the size of the modem circuitry, we fabricated on a printed circuit board (PCB), as depicted in Fig. 71.

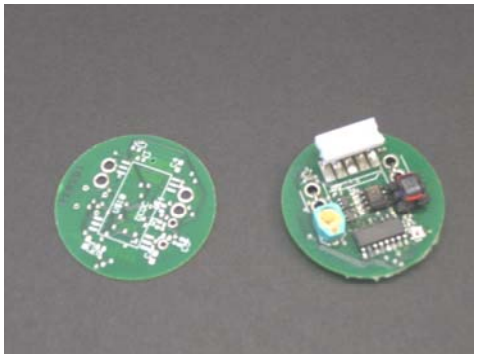

Fig. 71 Sensor PCB and PCB with components soldered in place

Here, the PCB is shown to the left, and the PCB with all modem components attached is shown to the right. The diameter of the board is 33.27mm, and the height with components installed is 9.42mm. The design of the sensor shell depends on the sensor type.

8.1.2.1. Open Sensors

Open sensors, such as EKG, which require direct skin contact, need to have the sensor exposed. We use the shell depicted in Fig. 72. This shell ensures that none of the circuitry is exposed to the environment, but that the sensor itself is in fact exposed to contact the user. Note the rounded form factor and smooth profile of the shell.

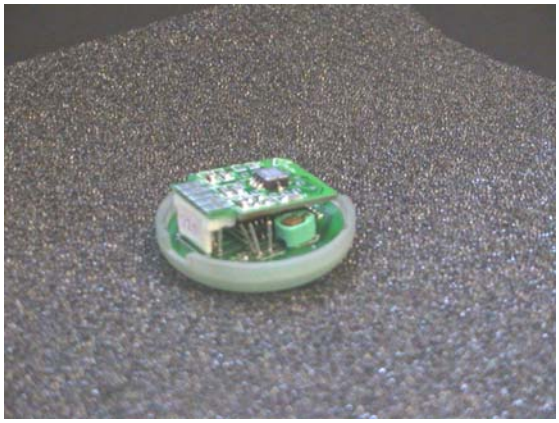

Fig. 72 Sensor shell for open sensors

8.1.2.2. Closed Sensors

Closed sensors such as the accelerometer require the sensor to be covered. For this reason, we use the shell depicted in Fig. 73**.** Once again, note the rounded form factor. In this case, we ensure that the sensor is inside the case, shielded from the environmental exposure. A picture of a completed, closed sensor node is shown in Fig. 73.

Fig. 73 Sensor shell for closed sensors

8.2. Central-Side Components

Conceptually, the design of the central-side components is similar to that of the sensor nodes. However, it differs quite a bit in its functionality. Whereas the nodes act somewhat passively, collecting data and transmitting when necessary, the central side components must coordinate node data transmission, provide power, and transmit information wirelessly to a local capture and storage mechanism.

8.2.1. Electronic Circuit

The electronic circuit of the central components is similar to that of the sensor nodes, but much more complicated. For transmitting and receiving data, the central components have a mirror-image circuit for DC-PLC superposition. It also has a PLL that modulates its outgoing data and demodulates incoming data. Unlike the sensor nodes, a higher level of intelligence is required for the central components. We use a PIC16 programmable controller in this capacity. The PIC16 allows us to determine an order and priority for the various sensor nodes in the system. Now, depending on the specific use for the CF garment, the PIC16 is connected either to a local data storage device or a wireless transmission device. In the case where the user is not critical, the system will act as a data storage device. In this case, the PIC16 instructs local data storage circuitry to keep data for later evaluation by a health professional. Alternatively, for real-time monitoring, the PIC16 passes the data to a wireless transmitter. An off-the-shelf component such as the Bluetooth-based Parani-SD can be used relatively effortlessly, as it replaces typical serial cables and has a range up to a kilometer. With a complementary socket on a local PC, the data can be transmitted over the internet and / or stored on the PC hard drive.

The centralized components also provide system power. Thus, we use a DC battery pack composed of four rechargeable NiMH. The battery pack is rated at 4.8VDC and 7200mAh, and weighs 125g.

For the central components, we use a solder-board for circuit mounting. The circuit board, along with the battery pack, is placed in a plastic shell. The shell has a rounded form factor, but a large flat surface, as it will be placed at the lower back of the garment. The fixturing method is the same as that of the sensor nodes. The central components have two leads, with one in contact with ground, and the other in contact with the CPS.

8.3. Conductive Fabric Garment

The design of the conductive fabric garment is motivated by the desire to have a wearable, comfortable monitoring system. As such, the style is based on normal outerwear. Sheets of CF are cut and sewn together according to normal sewing techniques. Elastic is sewn into the garment at the sleeves and waist to prevent unnecessary motion of sensors relative to the body.

To totally insulate the layers of conductive fabric, three layers of cotton are used. One layer is placed between the two conductive fabric layers, one is placed between the CF and the user,

and one is placed between the CF and the environment. At the edges of the garment, the three layers of cotton are sewn together, as depicted in Fig. 74. This forms a complete non-conductive shell around the CF. Now, to add sensors to the garment, a location is chosen, and the required electrical connections are made.

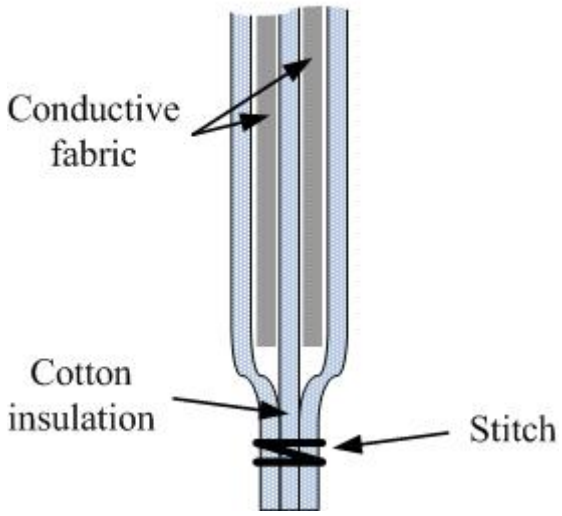

Fig. 74 Isolating the CF layers from one another and the environment

8.4. Sensor Removal

To remove sensors for washing or other situations, we have included an easy-removal mechanism for the sensor nodes and centralized components. The sensor shell separates into two parts. One part holds the electronic components. The other simply has the leads that connect to the garment. This second part remains intact with the garment while the electronic components are now separated. The garment and the remaining part of the sensor shell can then be washed without damaging any of the system. This process is depicted in Fig. 75.

Fig. 75 Separating the sensor shell from the garment

In situations in which the sensor must remain stationary, elastic or Velcro strips can be sewn into the garment in order to minimize motion relative to the user's skin. This is done, for instance, to minimize motion at the wrist, as depicted in Fig. 76. These strips may not be adequate for the fast motion associated with intense activities such as vigorous exercise or sports, but are adequate for normal daily activities.

Fig. 76 Elastic strips to minimize motion at the wrist

8.5. Biomechanical Model Reconstruction

So, to perform the experiments, I placed a MEMS accelerometer at my wrist, and one near the shoulder at 'heart level.' I placed my arm such that there was some variety of relative height between the two positions. For the following, refer to Fig. 77.

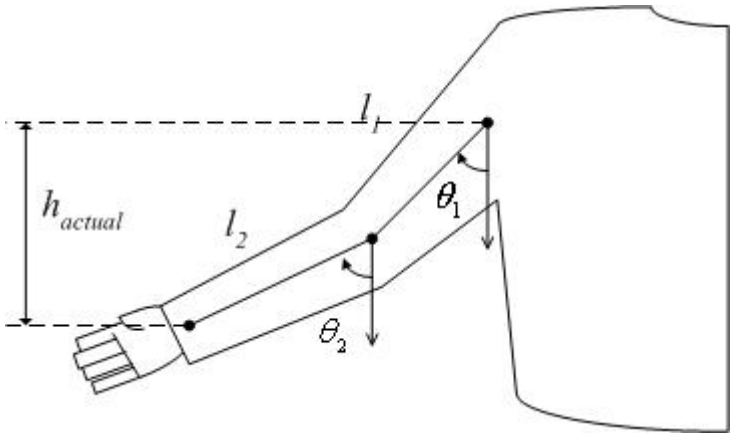

Fig. 77 Parameters for arm height measurements

The relative heights I used for h_{actual} were 37.5cm (arm completely vertical), 33cm, 32cm, 19.5cm, 13.5cm, and 4cm (arm almost horizontal). The reason for the 33cm and 32cm measurements is, even though the relative height was similar, in one case, I bent at the elbow, and in another, I didn't. For the 33cm case, θ_1 was equal to θ_2, and for 32cm, they were slightly

different. For the experiment, I measured out the various desired h_{actual} values. Then, using the accelerometer measurements, I calculated the expected height, h_{est}, using the relationship;

$$h_{est} = l_1 \cos\theta_1 + l_2 \cos\theta_2 \tag{59}$$

The results are shown in Fig. 78.

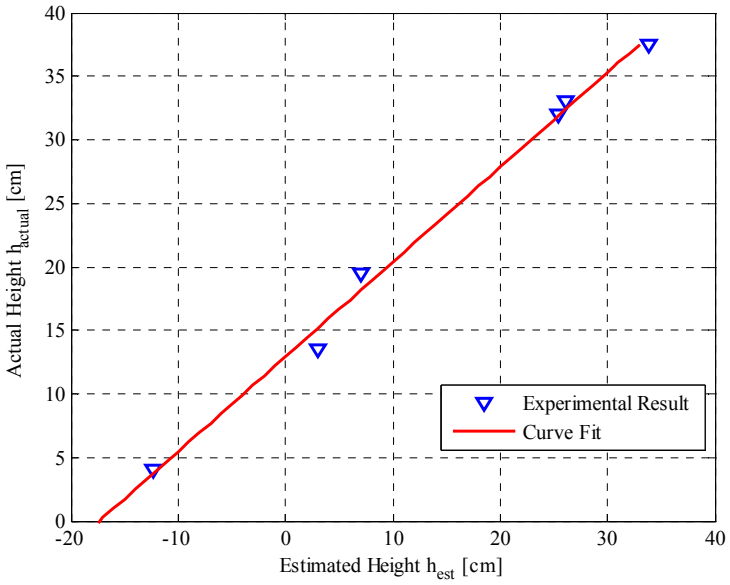

Fig. 78 Initial calibration results for accelerometer experiments

The equation for the fit is;

$$h_{actual} = 0.746 \times h_{est} + 12.925 \tag{60}$$

Of course, we would like to achieve a relationship where;

$$h_{actual} = 1 \times h_{est} \tag{61}$$

So there is an error in the slope, and an offset, that may be associated with some error in the measurement due to the accelerometer calibration. Nonetheless, the method definitely shows promise. I can do more experiments to try to eliminate some of the error associated with experimental process.

While doing the experiment, I made some observations. First, it is critical that the accelerometer remain in the vertical plane in order to assure accurate results. Note that the accelerometer must remain in the *x-y* plane (See Fig. 79).

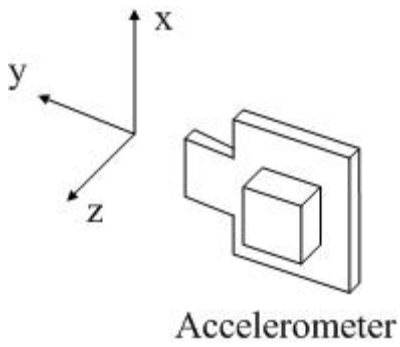

Fig. 79 Accelerometer axes

Rotation about the *z*-axis is what we are interested in for measuring the θ values. However, rotation about the *y*-axis will cause errors. For instance, if the accelerometer in the figure is rotated 90^{o} about *y*, then the reading will be orthogonal to gravity, and thus give an incorrect result. Nonetheless, this example indicates a specific application of our system, and a mechanism which would be significantly more costly in weight and bulk, if implemented using standard components.

8.6. Human Robot Interaction

Our architecture functions as a method of augmenting and integrating gesture recognition algorithms and techniques. Because we can facilitate total generality of sensor locations, additional information concerning movement, speed, directions, and gestures can be conveyed directly to a robot, or possibly by way of a local PC capable of processing the information. Thus, both line-of-sight and wireless communication can be facilitated. Here, we present a novel method for the analysis and design of CF sensor networks. We will start by formulating a model for conductive sheet sections, and verifying the model using experimental resistance measurements. Next, we will present an implementation of the proposed human-robot interaction. Finally, this will allow us to present design guidelines for CF suits.

The state of the art in gesture recognition has been documented extensively in a number of sources. The focus of this work is to create an architecture that more easily facilitates the use of current gesture recognition techniques. Such techniques fall into a few areas including user observation and tracking, physical gesture recognition, and verbal signals issued by the user. We have the ability to do this in a multitude of ways. The simplest method of interaction is pictured in Fig. 80, where a robot gains information from visual clues from a user.

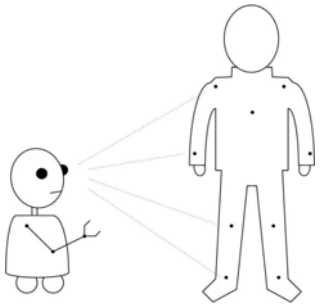

Fig. 80 Robot gaining visual information from sensors embedded in garment

9.Conclusion

We have made a number of key accomplishments to establish a workable model for the design of CF suits for health monitoring. We started by proposing a wearable network using conductive sheets. Next, we derived and verified an analytical model to describe 2D conduction in a CF sheets.

We then presented a DC power line communication system that allows us to exploit the CF properties. The technical issues specific to the use of a DC source were discussed and used to form functional requirements for a high-fanout system. An experimental apparatus confirmed our derived system model, and provided information on the system performance as the number of nodes in the system goes to infinity. By incorporating a TLT into the modem, we are able to exploit the resonance of the parasitics to ensure that power is delivered to the receivers, even for very high-fanout. An example of how we can take advantage of this feature to broadcast to large numbers of receivers is presented as well. It has been demonstrated that this protocol will work for communication with multiple nodes connected to the line.

Having verified the functionality of our DC-PLC system, we empirically quantified the resistance of a conductive fabric shirt, and used it to make hypotheses and initial observations about the DC resistance characteristic of CF garments. This DC analysis is necessary to determine power delivery characteristics of the garment. We derived and verified an analytical model to describe 2D conduction in a conductive fabric sheets. By simplifying the garment into cylindrical sections, we can use the 2D analytical result to describe the 3D garment behavior. In fact, such cylindrical sections exhibit behavior similar to 1D and 2D resistance expressions, and we subsequently derived the dependence of the resistance for the sections based on their geometry. By combining the aggregate resistances of individual cylinders used to model the garment, we derived an expression for the resistance characteristic of the 3D garment.

We also performed an AC analysis, relevant to the data transmission. Again, simplifying the garment into cylindrical sections, we applied transmission line theory to the garment. We were able to show the distributed nature of the garment, and the fact that, despite the small length scale, transmission line effects can be observed. We derived and verified a model to describe the impedance characteristic as a function of node placement in the garment.

The work culminated in the creation of a CF garment with sensor nodes embedded at various locations. We can make certain conclusions about are garment functionality by comparing to similar garments, such as the VivoMetrics LifeShirt [49]. The LifeShirt is rated at 8 hours of continuous use, with 1200mA battery capacity. Our system uses rechargeable 4-pack of NiMH batteries, which provide 7200mAH, or 900mA for 8 hours. With this capacity, we could continuously supply the Bluetooth module used for transmission [50] which draws 50mA, the central components which draw 80mA, and the 15 sensors at 50mA each. Introducing energy saving methods such as those proposed in [51] and [52], we can easily double the total use to 16 hours, and create a garment that can be worn from morning to night, and charged overnight.

Many important research topics of interest remain for this work. We focused primarily on the physical construction and architecture. Nonetheless, much work can be done on the signal processing, specifically the coding and transmission protocol. We use frequency shift keying for a number of reasons. The first is the simplicity of implementation – there are a number of standard chip sets that can be flexibly used for FSK schemes. FSK is a popular and commonly used scheme for modulating in the radio-frequency spectrum [53]. However, there are numerous channel access methods that are used for channel sharing, and extensive work has been done to characterize such methods based on desired bandwidth, bit error rate, quality of service, interference, and a number of other criteria. Such methods have been treated in text books [54],[55] as well as numerous papers [56],[57]. Applying a numerical modeling and analysis technique to this wearable network can allow for additional information to be gained. Further, in recent years, standard power line communication chip sets have been made available by vendors such as Maxim [58] and Yitran [59]. Such sets can be adapted to be used with a garment such as ours. The underlying modeling on the garment impedance and resistance would be required for determining the operating parameters of these components.

There are numerous channel sharing, modem equalization, and other communication techniques that are beyond the scope of this work. Nonetheless, many of these techniques can be applied to our system in order to augment and improve bandwidth, bit error rate, and signal quality. The exploration of such techniques and their application to this essentially new network that we have constructed is a rich area, and can serve to greatly improve the overall system functionality.

Work can also be done on the physical side of the garment construction. Investigation of more breathable materials (for insulation as well as transmission) can result in an even more lightweight garment, and by capturing less heat, the garment would improve comfortability. Initial experiments performed by the authors showed that significant portions of conductive fabric in non-critical locations, such as underarms or elbows, do not significantly alter the electrical transmission properties, but can reduce the peak core temperature of the user.

10. Appendices

10.1. Derivations of p_3 leading term

When evaluating the resistance, we utilize the equation;

$$R(x) = p_1 \times \log\left(\frac{h}{r}\right) + p_2 + p_3 \times (h) \tag{62}$$

Where the coefficients are given by;

$$\begin{aligned} p_1 &= k_{2D}\left(-265.36\left(\frac{D}{L}\right)^2 + 206.27\left(\frac{D}{L}\right) + 6.76\right) \\ p_2 &= k_{2D}\left(-914.42\left(\frac{D}{L}\right)^2 + 325.07\left(\frac{D}{L}\right) + 69.79\right) \\ p_3 &= \frac{\rho_{sq} L}{\pi D}\left(0.0091\left(\frac{L}{D}\right)^2 + 0.75\left(\frac{L}{D}\right) - 0.39\right) \end{aligned} \tag{63}$$

The k_{2D} term has already been explained. This is a constant that accounts for material properties for 2D transmission. Since p_1 and p_2 form 2D component of $R(x)$, we expect them to depend on k_{2D}. The p_3 term accounts for the linear 1D component of $R(x)$. The first term on the right side of p_3 has units of resistance, where ρ_{sq} is the sheet resistance, with units of Ω/square. This terminology, commonly used for flat conductors such as traces on printed circuit boards, gives the resistance of a given square of a conductor (see Fig. 81).

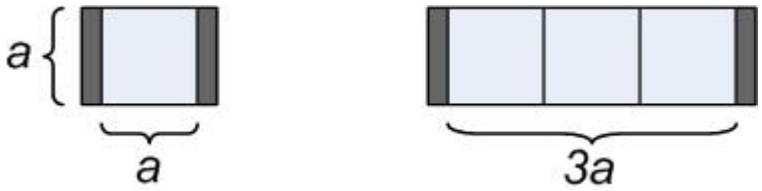

Fig. 81 Sheet resistance

For instance, assume there is a square of dimension $a \times a$, and a voltage is applied across the square with electrodes of length a resulting in a resistance of R_{square} (Fig. 81). Then, the material has a sheet resistance ρ_{sq} of R_{square}/square. Thus, for a square with any value of a, as long as electrodes of length a are used, the resistance will be equal to R_{square}. Further, if n squares are placed in series with one another, as in Fig. 81, the total resistance will be equal to nR_{square} Ω, where we have utilized the relationship;

$$R_{total}\left[\Omega\right] = n\left[\#squares\right] \times \rho_{sq}\left[\frac{\Omega}{square}\right] \tag{64}$$

For Fig. 81, the total resistance is $3\rho_{sq}$. When 'unwrapping' a thin cylinder, it becomes a sheet with dimensions $L \times \pi D$ (see Fig. 82).

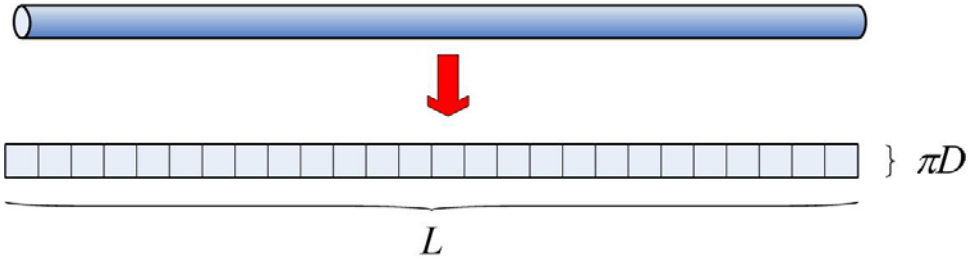

Fig. 82 Thin cylinder being unwrapped to form a series of squares

If we then break the sheet up into squares of dimension $\pi D \times \pi D$, then there will be $L/\pi D$ squares. Thus, the total resistance, given a sheet resistance, will be;

$$R_{total}\left[\Omega\right] = \frac{L}{\pi D} squares \times \rho_{sq}\frac{\Omega}{square} \tag{65}$$

For a thin cylinder, as πD gets small, we can approximate the electrode as covering the entire width πD. Thus, (65) gives us the leading term for p_3.

At first look, this term seems similar to the linear resistance relationship for a conductor given in (28); however, it should be noted that despite the similarities, (28) and the leading term on p_3 are derived using different procedures.

10.2. Derivation of $Z_t(s)$

For this derivation, we following the procedure illustrated in [34], pp. 443 – 444, we can write;

$$V_1(s) = sL_w I_1(s) \tag{66}$$

$$V_2(s) = sL_w I_2(s) \tag{67}$$

$$V_{g,out}(s) = V_1(s) + V_2(s) \tag{68}$$

$$I_{g,in}(s) = I_1(s) + \frac{V_1(s)}{R_w} - I_s(s) \tag{69}$$

$$I_{g,in}(s) = I_2(s) + \frac{V_2(s)}{R_w} - I_s(s) \tag{70}$$

$$V_{g,in}(s) = V_1(s) + V_{g,out}(s) + V_2(s) \tag{71}$$

Combining these equations, we can write;

$$\begin{aligned} V_{g,in}(s) &= V_1(s) + V_1(s) + V_2(s) + V_2(s) \\ &= 2\left(V_1(s)+V_2(s)\right) \end{aligned} \tag{72}$$

$$I_{g,in}(s) = \frac{1}{2}\left(\frac{V_1(s)+V_2(s)}{2sL_w}+\frac{V_1(s)+V_2(s)}{2R_w}+I_{g,out}(s)\right) \tag{73}$$

Next, we can write;

$$\frac{V_g(s)}{I_g(s)} = \left(\frac{8R_wZ_{g,out}}{Z_{g,out}+2R_w}\right)\frac{s}{s+\frac{1}{L_w}\left(\frac{R_wZ_{g,out}}{Z_{g,out}+2R_w}\right)} \tag{74}$$

Finally, we note that the magnetizing inductance, L_m, is equal to $2L_w$. So, we can finally write the impedance as;

$$Z_t(s) = \frac{V_{g,in}(s)}{I_{g,in}(s)} = \left(\frac{8R_wZ_l}{Z_l+2R_w}\right)\frac{s}{s+\left[\frac{2}{L_m}\left(\frac{R_wZ_l}{Z_l+2R_w}\right)\right]} \tag{75}$$

10.3. Impedance Coefficients

$$\alpha = \left(\frac{R}{R+8R_w}\right), \tau_1 = R_wC, \tau_2 = \sqrt{L_mC} \tag{76}$$

$$A = 16\alpha\tau_1\tau_2^2 \tag{77}$$

$$B = 8(n+1)(R_0)\left(\tau_2^2\right) \equiv b_1n + b \tag{78}$$

$$C = 16\alpha(n+1)(R_0)(\tau_1) \equiv c_1n + c_2 \tag{79}$$

$$D = 2(n+\alpha)(\tau_1)\left(\tau_2^2\right) \equiv d_1n + d_2 \tag{80}$$

$$E = (n+1)\left(4\alpha\tau_1^2 + \tau_2^2\right) \equiv \varepsilon_1n + \varepsilon_2 \tag{81}$$

$$F = 2(\alpha+1)(n+1)(\tau_1) \equiv f_1n + f_2 \tag{82}$$

$$G = 2\alpha(n+1)\left(\frac{\tau_1}{\tau_2}\right)^2 \equiv g_1n + g_2 \tag{83}$$

10.4. Gain Coefficients

$$\alpha = 32R_o^3L^2C \tag{84}$$

$$\delta = 4R_o^2 L^2 C\left[9nR_s + R_s + 8R_o\right] \tag{85}$$

$$\varepsilon = 2R_o L\left(n+1\right)\left[4R_o^2 R_s C + 9R_s L + 72R_o L\right] \tag{86}$$

$$\xi = 40\left(n+1\right)\left(R_o^2 R_s L\right) \tag{87}$$

11. References

[1] Glaros, C.; Fotiadis, D.I.; Likas, A.; Stafylopatis, A.; *A Wearable Intelligent System for Monitoring Health Condition and Rehabilitation of Running Athletes*, Proc IEEE EMBS 4th Int. Conference on Information Technology Applications in Biomedicine (ITAB 2003); Birmingham, U.K., April 24-26, 2003, pp. 276-279.

[2] Tsung-Che Chou; Nan-Fu Chiu; Fang-Ren Liao; Shey-Shi Lu; Feng Ping; Chang-Rung Yang; Chii-Wann Lin; *A Multi Parameters Wearable Telemetric System for Cardio-Pulmonary Fitness of e-Health*, Engineering in Medicine and Biology Society, 2005. IEEE-EMBS 2005. 27th Annual International Conference of the, 01-04 Sept. 2005 Page(s):3498 – 3501.

[3] Winterhalter, C.A.; Teverovsky, J.; Wilson, P.; Slade, J.; Horowitz, W.; Tierney, E.; Sharma, V.; *Development of electronic textiles to support networks, communications, and medical applications in future U.S. Military protective clothing systems,* Information Technology in Biomedicine, IEEE Transactions on, Volume 9, Issue 3, Sept. 2005 Page(s):402 – 406.

[4] Zieniewicz, M.J.; Johnson, D.C.; Wong, C.; Flatt, J.D.; *The evolution of Army wearable computers*, Pervasive Computing, IEEE, Volume 1, Issue 4, Oct.-Dec. 2002 Page(s):30 – 40.

[5] Martin, T.; Jovanov, E.; Raskovic, D.;*Issues in Wearable Computing for Medical Monitoring Applications: A Case Study of a Wearable ECG Monitoring Device*, Wearable Computers, 2000. The Fourth International Symposium on, 16-17 Oct. 2000 Pages:43 – 49.

[6] Stanford, V.; *Using pervasive computing to deliver elder care*, Pervasive Computing, IEEE, Volume 1, Issue 1, Jan.-March 2002 Page(s):10 – 13.

[7] Sherrill, D.M.; Bonato, P.; Moy, M.L.; Reilly, J.J.; *Accelerometer-based measurement of exercise and mobility for pulmonary rehabilitation*, Bioengineering Conference, 2004. Proceedings of the IEEE 30th Annual Northeast, 17-18 April 2004 Page(s):237 – 238.

[8] Marculescu, D.; Marculescu, R.; Zamora; Stanley-Marbell; Khosla Park; Jayaraman Jung; Weber, L.; Cottet, K.; Grzyb; Troster; Jones; Martin; Nakad; *Electronic textiles: A platform for pervasive computing*, Proceedings of the IEEE, Volume 91, Issue 12, Dec 2003 Page(s):1995 – 2018.

[9] Gemperle, F.; Kasabach, C.; Stivoric, J.; Bauer, M.; Martin, R.; *Design for wearability*, Wearable Computers, 1998. Digest of Papers. Second International Symposium on, 19-20 Oct. 1998 Page(s):116 – 122.

[10] Wade, E.; Asada, H.H. *Broadcasting Modem Hardware Design Using DC Power-Line Communication*, Mechatronics, IEEE/ASME Transactions on, Volume 11, Issue 5, Oct. 2006 Page(s):533 – 540.

[11] Wade, E.; Asada, H.H. *Wearable DC powerline communication network using conductive fabrics" Robotics and Automation*, 2004. Proceedings. ICRA '04. 2004 IEEE International Conference on , Volume: 4 , April 26-May 1, 2004 Pages:4085 – 4090.

[12] K. Van Laerhoven, N. Villar & H.-W. Gellersen. *A Layered Approach to Wearable Textile Networks*. In Proceedings of the IEE Eurowearable 2003; ISBN: 0-85296-282-7; IEE Press. Birmingham, UK, pp. 61-67.

[13] Post, E.R.; Orth, M.; *Smart fabric, or wearable clothing*; Wearable Computers, 1997. Digest of Papers., First International Symposium on, 13-14 Oct. 1997 Page(s):167 – 168.

[14] Azoulay, J. *Anisotropy in electric properties of fabrics containing new conductive fibers*, Electrical Insulation, IEEE Transactions on [see also Dielectrics and Electrical Insulation, IEEE Transactions on] , Volume: 23 , Issue: 3 , June 1988 Pages:383 – 386.

[15] United Nations. *Report of the second world assembly on ageing*. New York: United Nations; 2002.

[16] CDC, US Census Bureau, International Database, Table 094, available: http://www.census.gov/population/www/projections/natdet-D1A.html

[17] Department of Defense Caregiver Guide, *Taking Care of Elderly Family Members*, available: http://dde.carlisle.army.mil/tcefm/tcefm_main.htm

[18] Lebby; M. S., Jachimowicz; K. E.; *Textile fabric with integrated electrically conductive fibers and clothing fabricated thereof*, U.S. Patent, Patent Number: 5906004, May 1999.

[19] Lebby; M. S., Jachimowicz; K. E., Ramdani; Jamal.; *Textile fabric with integrated sensing device and clothing fabricated thereof*, U.S. Patent, Patent Number: 6080690, June 2000.

[20] Groff; C. P., Mulvaney; P. L.; *Wearable vital sign monitoring system*, U.S. Patent, Patent Number: 6102856, Aug. 2000.

[21] Rode, W.; Klintworth, R., Ludwig; K., Oberle, M. *System for long-term remote medical monitoring*, U.S. Patent, Patent Number: 6315719, Nov. 2001.

[22] Bardy, G.; *System and method for providing feedback to an individual patient for automated remote patient care*, U.S. Patent, Patent Number: 6860897, Mar. 2005.

[23] E. Munguia-Tapia, S. S. Intille, and K. Larson, *Activity Recognition in the Home Setting Using Simple and Ubiquitous Sensors*, in Proceedings of PERVASIVE 2004, LNCS 300, B. Heidelberg, Ed.: Springer-Verlag, 2004, pp. 158-175.

[24] Jayaramen, S., Park, S., Rajamanickam, R., Gopalsamy, C.; *Fabric or garment with integrated flexible information infrastructure for monitoring vital signs of infants*, U.S. Patent, Patent Number: 6687523, Feb. 2004.

[25] Lifton, J.; Broxton, M.; Paradiso, J.A.; *Experiences and directions in Pushpin computing*, Information Processing in Sensor Networks, 2005. IPSN 2005. Fourth International Symposium on, 15 April 2005 Page(s):416 – 421.

[26] Hines, David. *Unlocking the Potential of Power Distribution Networks*, Powerline Communications, April 2000.

[27] Strassberg, Dan. *Powerline Communication: Wireless Technology*, EDN Magazine, June 1996.

[28] Downey, W. and Sutterlin, P. *Power Line Communication Technology Update*, Echelon Corporation Presentation, available: http://www.lonworld.net/archive/2001/Presentations/Echelon_PLComUpdate.pdf

[29] Newbury, John E.; *Communications Services using the Low Voltage Power Distribution Network*, Transmission and Distribution Conference and Exposition, 2001 IEEE/PES, Vol. 2. Nov. 2001, P. 638-640.

[30] Chen, Yi-Fu, and Chieuh, Tzi-Dar; *A 100-Kbps Power-Line Modem for Household Application*s, International Symposium on VLSI Technology, Systems, and Applications. June 1999.

[31] FCC Bandwidth Allocation Chart, available: http://www.ntia.doc.gov/osmhome/allochrt.pdf

[32] Sutterlin, Philip H.; *Powerline Coupling Network*, U.S. Patent, Patent Number: 5485040, Jan 1996.

[33] Jerry Sevick; Transmission Line Transformers, Fourth Edition. Atlanta, GA: Noble, 1996, pp. 1-1 – 3-15.

[34] Ching Chuan Kuo, Ming Ying Kuo, and Mei Shong Kuo, *Modeling and Analysis of Wideband Power Transmission Line Transformers*, Applied Power Electronics Conference and Exposition, 1996. APEC '96. Conference Proceedings 1996., Eleventh Annual, volume: 1, 3-7 March 1996. pp. 441 – 446.

[35] MARKTEK Company website, available: http://www.marktek-inc.com/

[36] LessEmf Company website, available: www.lessemf.com/fabric.html

[37] Laird Technologies Company website, available: http://www.lairdtech.com/pages/products/EMI-FlectronConductiveFabric.asp]

[38] Blanchard, J.P.; Tesche , F.M.; Sands, S.H.; Vandre, R.H.; *Electromagnetic shielding by metallized fabric enclosure: theory and experiment,* Electromagnetic Compatibility, IEEE Transactions on, Volume 30, Issue 3, Part 2, Aug. 1988 Page(s):282 – 288.

[39] D. Cottet, J. Grzyb, T. Kirstein and G. Tröster, *Electrical Characterization of Textile Transmission Lines*, IEEE Transactions on Advanced Packaging, Vol. 26, No. 2, May 2003, pp. 182-190.

[40] Lorussi, F., Rocchia, W., Scilingo, E.P., Tognetti, A.; De Rossi, D.; *Wearable, redundant fabric-based sensor arrays for reconstruction of body segment posture*, Sensors Journal, IEEE, Volume 4, Issue 6, Dec. 2004 Page(s):807 – 818.

[41] Inaba, M.; Hoshino, Y.; Nagasaka, K.; Ninomiya, T.; Kagami, S.; Inoue, H.; *A full-body tactile sensor suit using electrically conductive fabric and strings*, Intelligent Robots and Systems '96, IROS 96, Proceedings of the 1996 IEEE/RSJ International Conference on, Volume 2, 4-8 Nov. 1996 Page(s):450 – 457.

[42] Wilson, N.; *The electrostatic behaviour of clothing fabrics containing electrically conducting threads, Electrostatic Problems During Material Handling*, IEE Colloquium on, 15 Feb 1994 Page(s):6/1 - 6/5.

[43] Gonzalez, J.A.; Rizvi, S.A.; Crown, E.M.; *Mathematical Modeling Of Electrostatic Propensity Of Protective Clothing Systems*, Electrical Overstress/Electrostatic Discharge Symposium Proceedings 1997, September 23-25,1997 Page(s):153 – 162.

[44] Joyner, K.H.; Copeland, P.R.; MacFarlane, I.P.; *An evaluation of a radiofrequency protective suit and electrically conductive fabrics*, Electromagnetic Compatibility, IEEE Transactions on, Volume 31, Issue 2, May 1989 Page(s):129 – 137.

[45] H. A. Haus, Case Studies in Electromagnetism, New York: John Wiley & Sons, 1960.

[46] A. R. Tilley, The Measure of Man and Woman, Human Factors in Design, New York, Henry Dreyfuss Associates, 1993.

[47] J. A. Kong, Electromagnetic Wave Theory, Cambridge, MA. EMW Publishing, 2000.

[48] D. H. Staelin, A. W. Morgenthaler, J. A.; Kong Electromagnetic Waves, Englewood Cliffs, NJ. Prentice Hall, 1994.

[49] VivoMetrics LifeShirt Technical Specifications, available:
http://www.vivometrics.com/site/system_techspecs.html

[50] Free2Move F2M03C1 BlueToooth Module datasheet, available:
http://www.free2move.se/pdf/Datasheet_F2M03C1.pdf

[51] Chiasserini, C.F.; Rao, R.R.; *Improving energy saving in wireless systems by using dynamic power management,* Wireless Communications, IEEE Transactions on, Volume 2, Issue 5, Sept. 2003 Page(s):1090 – 1100.

[52] Ying Li; Loke, S.W.; Ramakrishna, M.V.; *Energy-Saving Data Approximation for Data and Queries in Sensor Networks,* ITS Telecommunications Proceedings, 2006 6th International Conference on, June 2006 Page(s):782 – 785.

[53] Watson, B. *FSK: Signals and Demodulation*, WJ Communications Tech-Note, The Communications Edge, Watkins-Johnson Company, Vol. 7 No. 5, September 1980.

[54] Proakis, J. G.; Digital Communications, New York, McGraw-Hill Book Co., 1995.

[55] Betsekas. D., Gallagher, R.; Data Networks, Saddle River, NJ. Prentice Hall, 1992.

[56] Chit-Sang Tsang; Nguyen, T.M.; *Survey of signal processing techniques for interference suppression in communication*, Aerospace Conference, 2004. Proceedings. 2004 IEEE, Volume 2, 6-13 March 2004 Page(s):1347 – 1354.

[57] Yu Wang; Garcia-Luna-Aceves, J.J.; *Channel sharing of competing flows in ad hoc networks*, Computers and Communication, 2003. (ISCC 2003). Proceedings. Eighth IEEE International Symposium on 2003 Page(s):189 – 196.

[58] MAXIM MAX2986 datasheet, available: http://www.maxim-ic.com/powerline.cfm

[59] Yitran IT800 datasheet, available: http://www.yitran.com